Vibrational Quantisation of Skyrmions

William Grummitt

A thesis presented for the degree of

Doctor of Philosophy

School of Mathematics, Statistics and Actuarial Science

University of Kent

September 20, 2019

Vibrational Quantisation of Skyrmions

William Grummitt

Abstract

The Skyrme model can be used to describe atomic nuclei as topological solitons known as Skyrmions. Since atomic nuclei are intrinsically quantum objects, we must give a quantisation scheme for our Skyrmions in order to fully realise this description. Until very recently, almost all such calculations used an approach known as rigid body quantisation, which produces some plausible results for small nuclei but has many problems. In this thesis we consider a more involved quantisation scheme where we include some vibrational modes which allow the Skyrmions to deform. We demonstrate that this idea resolves some of the problems of the rigid body method.

The method of vibrational quantisation in the form that we will use is first seen in a 2015 paper by Chris Halcrow, where he applies the method to the Lithium-7 nucleus with promising results. Here we use a similar approach to describe the deuteron. We present some results from numerical calculations, and compare our results with previous work on the deuteron. In particular, we compare our results with those of a paper that includes some vibrational modes to quantise the deuteron, but does so in the instanton approximation. We also consider the case of having a non-zero pion mass in the model, which

is something that has not previously been analysed in detail.

We go on to consider the case of Oxygen-16. This nucleus has been approached using a vibrational method in a 2016 paper by Chris Halcrow, Chris King and Nick Manton. In this thesis we seek to generalise their method by using a full two-dimensional numerical scheme by way of a finite element method. This allows more general choices for the potential, specifically ones motivated by the Skyrme model. We will discuss how this alpha particle dynamics approach can be applied for other nuclei which have baryon number equal to a multiple of 4. An example is Carbon-12, where we conjecture that a suitable choice of manifold would be the three-punctured sphere.

Lastly, we also give a discussion of quantisation of Skyrmions using a quantum graph description. This is a way of considerably simplifying the numerical work by considering only certain key lines on the manifold of configurations. This reduces the problem to solving an ODE with simple endpoint boundary conditions, and we show that for Oxygen-16 this method gives a reasonable approximation of the low energy states.

Declaration

I declare that this thesis is entirely my own work. The research on which it is based is also my own, although some parts did involve some collaboration. In particular, the numerical work that underpins Chapter 3 was done in collaboration with Mareike Haberichter and Chris Halcrow, and the numerical work done in Chapter 4 was inspired by fruitful discussions with Chris Halcrow and Tom Winyard. Furthermore, any figures which have a citation in the caption are taken from other papers, with the appropriate permissions from the publishers.

This thesis is also not substantially the same as any work that I have previously submitted or am concurrently submitting for any other qualification, either at the University of Kent or any other institution.

William Grummitt

Acknowledgements

I would like to thank my PhD supervisor Steffen Krusch for the support he has given me throughout my time in Kent. He encouraged me to pursue my own ideas but was always there to offer support whenever I ran into difficulties. It is certainly the case that several parts of this thesis would not have been realised without his assistance. I also want to acknowledge my secondary supervisors Pavlos Xenitidis and Ian Wood for their support and contributions. Ian in particular was able to provide some valuable insight into the theoretical background behind quantum graphs which proved to be very useful. My studies have been well supported by Kent's School of Mathematics, Statistics and Actuarial Science, and I must especially thank Claire Carter who provides excellent support for all of the school's PhD students, and helps keep all of our spirits up. It would also be remiss of me not to acknowledge the EPSRC who provided funding for my PhD, without which I would not have been able to complete this work.

I am grateful to Mareike Haberichter, Chris Halcrow and Tom Winyard for their collaboration at various stages of my PhD. I should also thank all of my fellow PhD students in SMSAS, who have always helped to ensure a productive and friendly working environment, as well as my other friends, both in Canterbury and elsewhere, who have offered their support.

Most importantly I must thank my family. Having strong encouragement from home was vital during the inevitable periods where my work was not progressing as well as I would have liked.

Contents

1 Introduction **1**

1.1 The Skyrme model 6

1.2 Classical Skyrmions 13

1.2.1 Low charge Skyrmions and visualisation 13

1.2.2 Higher charge Skyrmions 15

1.3 Modifications to the Skyrme model 17

1.4 Thesis outline 19

2 Quantisation of Skyrmions **21**

2.1 Zero modes 24

2.1.1 Rigid body quantisation 25

2.1.2 Finkelstein-Rubinstein constraints 29

2.2 Vibrational modes 33

2.3 Summary 39

3 Vibrational quantisation of the B=2 Skyrmion **40**

3.1 The B=2 Skyrmion 40

3.2 Vibrational quantisation for $B = 2$ 43
3.3 Previous work on $B = 2$ 49
3.4 Results 51
3.4.1 The numerically generated functions 51
3.4.2 Wavefunctions 54
3.4.3 Comparison with experiment 54
3.5 Remarks on the relative contributions of the vibrational mode and the pion mass term 57
3.6 Discussion and outlook 60

4 Vibrational quantisation of the Oxygen-16 nucleus 64
4.1 The rigid body case for Oxygen-16 67
4.2 Important properties of the region F 70
4.3 The different representations 77
4.4 Boundary conditions on the vibrational wavefunctions 79
4.5 The potential 87
4.6 Constructing solutions 89
4.7 Mapping to the full solutions 103
4.7.1 Comments on the parameters 112
4.8 Allowed spins in the different representations 113
4.9 Energies 118
4.9.1 Vibrational energies 118
4.9.2 The rotational energy E_J 119

4.9.3 Remarks on calibration . . . 120
4.10 Alternative potentials . . . 121
4.10.1 Results for the first sextic potential . . . 127
4.10.2 Results for the second sextic potential . . . 130
4.11 A new approach: two-dimensional numerics . . . 133
4.11.1 A proof of concept . . . 134
4.11.2 Calibration . . . 137
4.11.3 Spectrum . . . 139
4.12 Constructing a new potential . . . 142
4.12.1 Results . . . 147
4.12.2 Spectrum . . . 151
4.13 Discussion and outlook . . . 151

5 A quantum graph approach for Oxygen-16 156

5.1 Introducing the idea . . . 156
5.2 A proof of concept . . . 166
5.2.1 Results . . . 166
5.2.2 Discussion . . . 169
5.3 Other potentials . . . 170

6 Carbon-12 and the three-punctured sphere 172

6.1 The three-punctured sphere as a vibrational manifold . . . 175
6.2 The shape space of triangles . . . 176
6.3 Symmetries and boundary conditions . . . 178

6.4 Allowed spin states for Carbon-12 179
6.5 Outlook 181

7 Conclusion **183**

7.1 Summary and discussion 183
7.2 Outlook 187

List of Figures

1.1 Plots for the first four minimal energy Skyrmions (from left to right: $B = 1$ to $B = 4$) [35]. 14

1.2 A plot of the $B = 8$ Skyrmion (left) and the triangle and chain configurations for $B = 12$ (centre and right respectively) [19],[58]. The triangle and chain configurations have similar energies. 16

1.3 Plots for Skyrmion configurations with $B = 16$; the tetrahedron and the square [30]. 16

2.1 A visual representation of the double covering space CQ_B in relation to configuration space Q_B. We see that two points in CQ_B correspond to the same point in Q_B [38]. 31

3.1 A representation of the scattering of two $B = 1$ Skyrmions, which coalesce together to form a $B = 2$ torus before moving apart perpendicular to the original direction [21]. 41

3.2 Plots for the various functions that were numerically calculated for $B = 2$ using gradient flow. 52
3.3 Plots for the metric and rotational energy functions, that were calculated from the numerically generated functions from Figure 3.2. 53
3.4 Plots for the Sturm-Liouville functions p, q and w. Notice that we plot two functions for q, corresponding to the two different rotational energy terms. 54
3.5 Plots for the wavefunctions for the deuteron and isospin-1 states. 55

4.1 The scattering mode for four alpha particles in the Skyrme model, taken from [30] and using the colouring convention found in [19]. 65
4.2 From left to right: the 6-punctured sphere, the surface M and the region F [30]. 66
4.3 Three important configurations of the $B = 16$ Skyrmion: from left to right we have the tetrahedron, the square and the bent square [28]. 69
4.4 A figure showing the relationship between the different coloured regions of F using the matrices A and B. 72
4.5 The full six-punctured sphere projected onto the complex upper half-plane. 74

4.6 A plot showing the region F. We use the relationship between the points z^+, z^- and z^0 to determine the conditions on the boundary line $\eta = 1$. 80

4.7 A plot showing the region F. We use the relationship between the points z^+, z^- and z^0 to determine the conditions on the boundary curve C. 82

4.8 A plot showing the region F. We use the relationship between the points z^+, z^- and z^0 to determine the conditions on the extended boundary curve C for standard representation states. 86

4.9 A 3D plot of the potential (4.28) for $\eta > 0$, with $\omega = \sqrt{3}$ and $\mu = 8\sqrt{2}$. The red circle shows the position of the tetrahedral configuration and the blue circles show the squares. 88

4.10 A plot showing ten boundary points as selected by the three different methods. The red stars are equally spaced in η, the blue diamonds are equally spaced along the curve using standard distance measures, and the green circles are equally spaced along the curve using a hyperbolic distance measure. . 97

4.11 Plots for the first four even H functions we include in our ground state wavefunction solution. 99

4.12 The first few functions G_k for the ground state solution. . . . 100

4.13 A contour plot of the ground state vibrational wavefunction in the red region of F. 102

4.14 A contour plot of the ground state vibrational wavefunction on the full region F. 104
4.15 A contour plot of the lowest energy vibrational wavefunction in the sign representation. 105
4.16 Plots for excited vibrational wavefunctions in the trivial (left) and sign (right) representations. 106
4.17 Plots for excited vibrational wavefunctions in the trivial (left) and sign (right) representations, with opposite parities. 109
4.18 A failed attempt to calculate a standard representation state using separation of variables. 111
4.19 Plots for excited vibrational wavefunctions with $\omega = 10$ and $\mu = 1$. 112
4.20 3D plots for the potential with no η dependence and the quartic potential. 125
4.21 3D plots of the two sextic potentials. 127
4.22 Contour plots for the lowest lying vibrational wavefunctions in the trivial and sign representations respectively, for the first sextic potential. 128
4.23 Contour plots for the first excited vibrational wavefunctions in the trivial and sign representations respectively, for the first sextic potential. 128

4.24 Contour plots for the excited vibrational wavefunctions in the trivial and sign representations with the opposite parity condition, for the first sextic potential. 129
4.25 Contour plots for the lowest lying vibrational wavefunctions in the trivial and sign representations respectively, for the second sextic potential. 130
4.26 Contour plots for the first excited vibrational wavefunctions in the trivial and sign representations respectively, for the second sextic potential. 131
4.27 Contour plots for the excited vibrational wavefunctions in the trivial and sign representations with the opposite parity condition, for the second sextic potential. 131
4.28 The colour key used in the production of the FreeFEM++ figures. 134
4.29 Plots for the trivial (left) and sign (right) vibrational wavefunctions calculated using two-dimensional numerics, in order of excitation. 135
4.30 Plots for the trivial (left) and sign (right) opposite parity vibrational wavefunctions calculated using two-dimensional numerics. 136
4.31 Plots for the first three standard representation wavefunctions $u + w$ with positive parity. 137

4.32 Plots for the first three standard representation wavefunctions $u - w$ with positive parity. 138
4.33 Plots for the first three standard representation wavefunctions $u + w$ with negative parity. 138
4.34 Plots for the first three standard representation wavefunctions $u - w$ with negative parity. 139
4.35 A spectrum for Oxygen-16 using the energies calculated in Table 4.6. Here circles represent states we have calculated in our model and crosses represent experimental states. Blue symbols denote states with positive parity and red symbols denote states with negative parity. 141
4.36 The colour key used in the production of the new potential. . 144
4.37 Plots for the two functions V_{tet} and V_{sq} from (4.63) that we will use to construct our new potential. 145
4.38 The new potential, which is now smooth everywhere and finite as $\epsilon \to \infty$. 145
4.39 Plots for the trivial (left) and sign (right) vibrational wavefunctions for the new potential from Figure 4.38, in order of excitation. 148
4.40 Plots for the trivial (left) and sign (right) opposite parity vibrational wavefunctions for the new potential from Figure 4.38. 149

4.41 Plots for the first two standard representation wavefunctions $u + w$ with positive parity for the new potential from Figure 4.38. 149

4.42 Plots for the first two standard representation wavefunctions $u - w$ with positive parity for the new potential from Figure 4.38. 150

4.43 Plots for the first three standard representation wavefunctions $u + w$ with negative parity for the new potential from Figure 4.38. 150

4.44 Plots for the first three standard representation wavefunctions $u - w$ with negative parity for the new potential from Figure 4.38. 151

4.45 The spectrum calculated for Oxygen-16 for the new potential from Figure 4.38. As before, blue symbols denotes positive parity states and red symbols denote negative parity states. Circles denote states predicted by our model and crosses denote experimental energy values where they are known. 152

5.1 A plot of the region F with the three scattering modes clearly marked. 158

5.2 A display of the quantum graph structure obtained from considering the three scattering lines in F. 158

5.3 The separated quantum graph for the trivial and sign representations. 160
5.4 The further reduced quantum graph, which now consists of only one fundamental node. 163
5.5 Plots for the quantum graph solutions, again with trivial states on the left and sign states on the right. The profile solution of the full solution is in green and the quantum graph solution is in red. The dashed black line denotes the position of the tetrahedron where we do not specifically impose a boundary condition. 168

6.1 Plots of the projection of the full three-punctured sphere onto the complex upper half-plane (left) and the projection of one quarter of the surface (right). 175
6.2 A plot of the quarter of the three-punctured sphere from Figure 6.1b, but now displayed on the Poincaré disk. 176

List of Tables

2.1 A table of the predicted and experimental ground state spins and isospins for $B = 1$ to $B = 9$. 34

4.1 A table listing the allowed rigid body spin states with zero isospin for the three main $B = 16$ configurations. 69

4.2 Eigenvalues k for the first ten symmetric functions with even boundary conditions on H. 100

4.3 Coefficients a for the ground state wavefunction. 101

4.4 The first twenty coefficients for the first excited vibrational wavefunction in the trivial representation. 108

4.5 The numerically calculated energies for the eight states we have calculated so far. The states are labelled (a) through to (h). States (a) to (c) are the first three states in the trivial representation in order of excitation, with (d) being the trivial representation state with negative parity. Similarly states (e) to (g) are the first three states in the sign representation with (h) being the sign representation state with positive parity. . . 118

4.6 A table showing the calibrated energies for different states J^P. We also give the relevant vibrational state, and where the experimental value is known this is listed for comparison. All energies are now given in MeV. 140

5.1 A table comparing the vibrational energies of states using the quantum graph and full two-dimensional methods. 169

6.1 A table listing bases of allowed spin states for each J^P for Carbon-12. 180

Chapter 1

Introduction

The Skyrme model is a non-linear field theory of pions that was first proposed by Tony Skyrme in the 1960s [62]. The model supports soliton solutions which have non-trivial topology, and the minimal energy topological soliton solutions are called Skyrmions. The Skyrmions are all labelled by an integer topological charge, which we denote by B as we shall see that it is related to the baryon number in nuclear physics. Skyrmions are static, spatially localised field configurations which are generally highly stable due to the topology of the system.

The key insight of Skyrme was to realise that Skyrmions could be identified with atomic nuclei through their topological charge. For example the simplest Skyrmion with charge $B = 1$ could be identified with the simplest atomic nucleus, Hydrogen, which consists of a single proton and so has baryon number 1. Furthermore, we shall see that the $B = 1$ Skyrmion is spherically

symmetric and behaves essentially like a point particle at low energies (indeed we shall discuss shortly that the Skyrme model is really only applicable in the low energy regime). It is also the case that the long range interaction of two $B = 1$ Skyrmions is reminiscent of experimentally observed interactions between two nucleons [65]. These basic observations indicate that Skyrme's insight of identifying Skyrmions with nuclei is plausible in at least the simplest cases.

If we look at larger values of the topological charge, we see that Skyrmions do not behave in quite the way we might naively expect. That is to say that the minimal energy configurations are not simply clusters of $B = 1$ spheres, but rather the Skyrmions will coalesce together into lower energy configurations, where one cannot easily identify the individual Skyrmions. One example that will be important to much of the work done in this thesis is that of the $B = 4$ Skyrmion. This can be identified with the Helium-4 nucleus (also known as the α-particle), and is described in the Skyrme model not as a collection of four spheres but rather as a cubic configuration. This is an important difference to many more conventional nuclear models which are based on the idea of a set of distinct nucleons interacting through an experimentally motivated potential.

In fact, it is a nice property of the Skyrme model that all of the dynamical and interaction phenomena are determined by just the Skyrme Lagrangian, which we shall see shortly. This Lagrangian has only a handful of free parameters (the exact number depends on whether we include any optional

additional terms), and so an analysis of the Skyrme Lagrangian is less complicated than in the case of many other nuclear models. This mathematical convenience, in combination with the fact that the model unifies baryons and mesons, meant that the theory was very popular when it was first published. More recent developments by Witten and then by Sakai and Sugimoto have demonstrated further connections between the Skyrme model and QCD. Witten showed that in QCD theories with a large number of quark colours, baryons behave like solitons in a way that is based upon how their masses scale [68]. Sakai and Sugimoto demonstrated that the Skyrme Lagrangian could be rederived from a holographic QCD model [61]. These discoveries have kept interest in the Skyrme model alive, and will motivate our studies of it.

It would be useful at this point to briefly discuss some other common nuclear models, so as to provide a point of reference for comparisons and contrasts with the Skyrme model. Ever since the discovery of the nucleus, physicists and mathematicians have attempted to come up with theoretical models that describe experimentally observed nuclear phenomena. It is now understood that nuclear physics is well described by QCD, but since this is a highly complex theory numerous models have been developed to approximate nuclear physics in a way that is more mathematically tractable. We go through a few examples here.

In the shell model atomic nuclei are described as collections of distinct nucleons which interact only through an external potential (that is to say

there is no explicit nucleon-nucleon interaction) [15]. Starting from this idea, one can derive a Schrödinger equation and a discrete energy spectrum. Because of the Pauli Exclusion Principle, these levels are filled as the baryon number increases and each level is called a shell. In certain cases, the number of protons or neutrons in a nucleus is such that shells are perfectly filled, and these are called magic numbers. It turns out that the shell model works very well for magic and nearly magic nuclei, but less well if one is further away from a magic number. The first few magic numbers in the model are $B = 2, 8, 20, 28$ and 50. For higher values, the magic numbers may be different for protons and neutrons. There is also the special case of doubly magic nuclei, where the number of protons and neutrons are both equal to a magic number. Examples include Helium-4, with two protons and two neutrons, and Oxygen-16, with eight protons and eight neutrons. The shell model predicts that these doubly magic nuclei should be highly stable, and this is seen experimentally. For example, Helium-4 is among the most abundant and stable nuclei in the universe [53].

The cluster model starts from a different principle. Rather than building nuclei from individual nucleons, larger nuclei are built from smaller nuclei. The best smaller nucleus to use as a building block is often considered to be the Helium-4 nucleus (α-particle) as it is highly stable due to having a very high binding energy [27]. The α-particles can then be glued together in various different shapes to make larger nuclei where the baryon number B is a multiple of four, and excitations of the nuclei are described by vibrations

of the shapes.

Chiral perturbation theory is an effective field theory where one constructs a Lagrangian that has the relevant symmetry properties of full QCD, namely an approximate chiral symmetry and symmetry under parity and charge conjugation. One then writes down all of the terms that satisfy these symmetries and keeps the leading order terms, discarding terms that are above a certain order. To do this, one must specify a criterion in advance for ranking the order of terms, and there are several different options for doing this. The theory has been applied with some success to nucleons and mesons [22] and to hadron-hadron interactions [46].

Another model is lattice QCD. This is a non-perturbative approach where the QCD theory is formulated on a lattice of points. In the limit where the lattice is taken to be infinitely large and the points infinitesimally close together, the full QCD model is returned. However, if we do not take this limit then we have a discrete version of QCD which naturally introduces a cut-off for the momentum at $1/a$ if a is the spacing of the lattice points. This model allows the investigation of phenomena which cannot be analysed by perturbative models, such as quark confinement which is a non-perturbative effect [67].

A last model to discuss is random matrix theory. Wigner introduced the idea in [66] that random matrices could be used to model the nuclei of heavy atoms. In particular he proposed that the spacings between spectral lines in heavy nuclei could be related to the spacings between the eigenvalues of

a random matrix. This idea works quite well for very large nuclei, and the idea is discussed in detail in [51].

These models take different approaches but all have some successes in different areas. For example, the shell model works well for magic nuclei, the cluster model for nuclei with baryon number equal to a multiple of four and random matrix theory for very large nuclei. Unfortunately no nuclear model works well in all regimes, which is why a variety of models are used. We will make particular use of the cluster model later in this thesis in our discussion of the Oxygen-16 nucleus.

1.1 The Skyrme model

Let us now go into some of the basics of the Skyrme model itself. The model is valid in the low energy limit of QCD as this is where the mesonic degrees of freedom are dominant. Quark and gluon degrees of freedom can be ignored as there are no free quarks or gluons at this energy. In particular, there are no free quarks due to the phenomenon of confinement which we briefly mentioned in our discussion of other nuclear models. At low energies quarks must group together to form hadrons. There are no colour singlets as hadrons consist of either a quark and anti-quark pair of the same colour (mesons) or three quarks of the three different colours (baryons). In each case the colour charges will cancel out.

In the Skyrme model we consider only pions, the lightest mesons, since

this simplification is reasonable from a physics perspective and makes the model more mathematically tractable. As such, the Skyrme Lagrangian is constructed from pion fields. We define the Skyrme field U, which is an $SU(2)$ field, as

$$U(t, \boldsymbol{x}) = \sigma(t, \boldsymbol{x}) + i\boldsymbol{\pi}(t, \boldsymbol{x}) \cdot \boldsymbol{\tau}, \tag{1.1}$$

where π_i are the pion fields, τ_i are the Pauli matrices and σ is a scalar field which is included so that $U \in SU(2)$, meaning that it must satisfy the constraint

$$\sigma^2 + \boldsymbol{\pi} \cdot \boldsymbol{\pi} = 1. \tag{1.2}$$

When constructing the Skyrme Lagrangian, we begin with the motivation that our Lagrangian should retain the properties of the QCD Lagrangian in the low energy limit. In particular, the low energy QCD Lagrangian has Lorentz and chiral symmetry. The chiral symmetry is responsible for up and down quarks in QCD having equal mass, which in turn leads to pions having zero mass. In nature there is in fact a small mass difference between up and down quarks leading to a minor breaking of chiral symmetry, and hence non-zero pion masses. Thus, when we build the Skyrme Lagrangian we begin with a fully chirally symmetric Lagrangian and then add a pion mass term, where the pion mass will be small enough that the chiral symmetry is only broken slightly. Furthermore, we will require that our Lagrangian produces Euler-Lagrange field equations which contain no higher than second order time derivatives, as this is a requirement for physical models. Considering

all of these points, a natural candidate for the Lagrangian is

$$\mathcal{L} = -\frac{F_\pi^2}{16}\,\mathrm{Tr}(R_\mu R^\mu) + \frac{1}{32e^2}\,\mathrm{Tr}([R_\mu, R_\nu][R^\mu, R^\nu]) + \frac{1}{8}m_\pi^2 F_\pi^2\,\mathrm{Tr}(U - 1_2), \quad (1.3)$$

where $R_\mu = (\partial_\mu U)U^\dagger$ is the right current of the Skyrme field U, F_π is the pion decay constant, e is a dimensionless parameter that represents a coupling constant, m_π is the pion mass and 1_2 is the two dimensional identity matrix. Also, we have used the Einstein summation convention where repeated indices are summed over, and this convention will be used throughout this thesis. Note that this Lagrangian is not the only possible choice satisfying the criteria we have outlined. For example, one could also include a term that is sextic in derivatives of U, and some modifications to the Skyrme model do consider this case. The mass term is also not unique, and can be chosen differently.

It will be useful at this point to make a comment on calibration of the model. We would like to fix the parameters F_π, e and m_π. Experimentally it is known that $F_\pi = 186$ MeV and $m_\pi = 138$ MeV [6], so one could argue that the only truly free parameter is e. In practice however, we treat F_π as a renormalised pion decay constant, which allows it to vary, and we also allow e to vary with the baryon number, that is $e = e(B)$. This allows us to get better overall agreement with experiment. The values of our parameters can then be fixed in a number of different ways. The most common method, first proposed in [2] and [3], is to fit the model in the $B = 1$ sector to the masses

of the proton and the delta resonance. A different method is proposed in [50], where the calibration is done by fitting the mass and size of the $B = 6$ Skyrmion to the Lithium-6 nucleus, using the rational map ansatz. Indeed, there have been numerous other methods used to calibrate the model, but we will use the mainstream convention from [2] and [3]. The length and classical energy scales of the model are $2/(eF_\pi)$ and $F_\pi/(4e)$ respectively. If we convert our Lagrangian into these Skyrme units, it takes the tidier form

$$\mathcal{L} = -\frac{1}{2}\,\mathrm{Tr}(R_\mu R^\mu) + \frac{1}{16}\,\mathrm{Tr}([R_\mu, R_\nu][R^\mu, R^\nu]) + m^2\,\mathrm{Tr}(U - 1_2), \qquad (1.4)$$

where we have also defined $m = 2m_\pi/(eF_\pi)$ as the dimensionless pion mass. We keep m_π fixed at the experimental value, so whenever we make a choice for the value of m we fix the length scale and the value of e.

The first term in (1.4) is quadratic in spatial derivatives, and if we include only this term we have a sigma model. However, it turns out from a scaling argument that such a model cannot admit stable soliton solutions. We shall shortly present a scaling argument by Derrick that demonstrates that we must include a term that contains higher powers of derivatives (the Skyrme term which is the second term in (1.4)) in the Lagrangian in order obtain stable soliton solutions.

If we consider the static energy of the Skyrme field we find that it is given

by

$$E = \int -\frac{1}{2}\,\mathrm{Tr}(R_i R_j) - \frac{1}{16}\,\mathrm{Tr}([R_i, R_j][R_i, R_j]) - m^2\,\mathrm{Tr}(U - 1_2)d^3x, \quad (1.5)$$

where we have switched from Greek to Latin indices to indicate that we are now working in spatial coordinates only. It can now be shown that the presence of the pion mass term imposes the boundary condition requirement for finite energy that $U \to 1_2$ as $|\boldsymbol{x}| \to \infty$. Note that making a choice of vacuum breaks chiral symmetry, which in general is given by the Lagrangian being invariant under

$$U \to AUB^\dagger, \quad (1.6)$$

where A and B are constant $SU(2)$ matrices. If we have a non-zero pion mass however, the condition $A = B$ is enforced, which reduces the full chiral symmetry to an $SU(2)$ symmetry, which we shall see later is related to isopsin. We will enforce the boundary condition $U \to 1_2$ as $|\boldsymbol{x}| \to \infty$ by hand, so that the chiral symmetry is broken even for the Skyrme model with massless pions. Note that finite energy forces $U \to 1_2$ at spatial infinity as the only possible choice of vacuum.

Another key point here is that we can now identify all of the points at infinity as a single point as U takes the same value at all of these points. This allows us to compactify physical space $\mathbb{R}^3 \cup \{\infty\}$ to the three-sphere S^3. It is also the case that the $SU(2)$ target space has group manifold S^3 [49], and so our Skyrmions can be thought of as corresponding to maps from S^3

to S^3. It is a well known result from homotopy theory that such maps are indexed by an integer giving the degree of the map. In our case the quantity is the one that we will come to identify with the baryon number and is given by

$$B = -\frac{1}{24\pi^2}\int \epsilon_{ijk}\,\mathrm{Tr}(R_iR_jR_k)d^3x, \tag{1.7}$$

and this quantity is topologically invariant. We refer to this as the topological charge.

However, the existence of a topological charge is not sufficient to give us stable soliton solutions. If we consider equation (1.5), we see that the three terms are of degree two, four and zero respectively in spatial derivatives, that is $E = E_2 + E_4 + E_0$. Thus under rescaling by $\boldsymbol{x} \to \lambda^{-1}\boldsymbol{x}$, the energy becomes

$$E = \frac{1}{\lambda}E_2 + \lambda E_4 + \frac{1}{\lambda^3}E_0. \tag{1.8}$$

We notice that the zeroth and second order terms both scale inversely with lambda and so any solution could be scaled down to a point with zero energy. However the fourth order Skyrme term scales in the opposite direction, and so stabilises the solitons to some preferred scale. This tells us that we require the second order kinetic term and the fourth order Skyrme term to obtain stable solutions. The zeroth order term is not absolutely required (and if we choose the pion mass to be zero it will vanish), but including it can yield more physically relevant results. It should also be noted that the fourth order term we have chosen is the unique fourth order term which satisfies Lorentz

invariance and has at most two time derivatives.

One can also use a Bogomolny type argument (using completing the square) to show that there is a lower bound on the energy of a static Skyrmion configuration [17], given by

$$E \geq 12\pi^2 B. \tag{1.9}$$

The minimal energy configurations are generally close to this bound but equality is never quite obtained for non-trivial configurations. For the $B = 1$ Skyrmion the minimal energy is 1.232 times this amount when $m = 0$ and 1.416 times this bound when $m = 1$. These numbers decrease somewhat towards 1 as B increases but do not reach it, even asymptotically. For the case of an infinite Skyrme crystal, Battye and Sutcliffe calculated in [7] an energy per baryon of $E/B = 1.036$. The idea of the nuclear energy being proportional to the baryon number is well supported by nuclear physics.

It will be useful to define what we mean by the binding energy of a Skyrmion. In nuclear physics the binding energy is the energy required to pull a nucleus apart into its constituent nucleons. In the Skyrme model it is therefore natural to think of the classical binding energy as the energy required to break a Skyrmion down into its constituent $B = 1$ Skyrmions. This is defined simply as

$$E_{\text{binding}} = BE_1 - E_B, \tag{1.10}$$

where E_1 is the energy of a single Skyrmion and E_B is the energy of the

charge B Skyrmion.

1.2 Classical Skyrmions

The Euler-Lagrange equations for the Skyrme model are not solvable analytically but can be solved numerically. In the interest of completeness, we will show them here and they take the form

$$\partial_\mu \left(R^\mu + \frac{1}{4} \left[R^\nu, [R_\nu, R^\mu] \right] \right) = 0. \tag{1.11}$$

An alternative approach to looking for numerical solutions is to consider the rational map ansatz which gives approximate solutions [32] but we will not dwell on that here. When minimal energy configurations have been numerically calculated we will want to display them, so we discuss techniques for visualising solutions here.

1.2.1 Low charge Skyrmions and visualisation

There are two features of a Skyrmion that we want to see when we plot solutions. The first is the baryon density. This is the integrand in equation (1.7) and tells us where the nuclear matter is distributed and lets us see by eye any symmetries the Skyrmion has. The second property we are interested in is the direction of the pion fields $\boldsymbol{\pi} = (\pi_1, \pi_2, \pi_3)$. It is a Skyrme model convention to see this by colouring our baryon density surfaces, typically

using the Runge colour sphere originally proposed by the German painter Philipp Otto Runge in 1810 [60]. Using this colouring scheme gives the convention of colouring the Skyrmion white where $\pi_3 = 1$, black where $\pi_3 = -1$, and then red, green and blue for the combinations of $\pi_1 + i\pi_2$ equal to 1, $\exp(2\pi i/3)$ and $\exp(-2\pi i/3)$ respectively. This precise colouring scheme is first used for Skyrmions in [19].

We now consider the simplest cases as an example. The numerical solutions for topological charges $B = 1$ to $B = 4$ have been well known for some time, for example see [12], and we display the coloured baryon density surfaces in Figure 1.1.

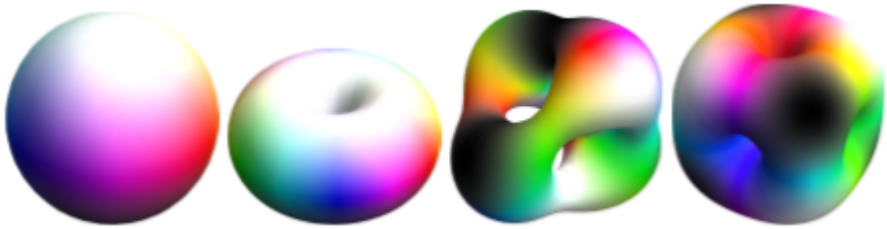

Figure 1.1: Plots for the first four minimal energy Skyrmions (from left to right: $B = 1$ to $B = 4$) [35].

We see that this is a convenient way of visualising Skyrmions, as it allows us to easily see the spherical, toroidal, tetrahedral and cubic symmetries of the four respective Skyrmions. It also lets us see properties of the pion fields, such as for the $B = 1$ Skyrmion we see that the third component of the field is 1 at the north pole and -1 at the south pole, and then each other colour appears once wrapping around the equator. We also note that the highly

symmetric nature of the $B = 4$ cube gives it a high binding energy. This is consistent with it needing to be identified with the α-particle, and also with it potentially being used as a building block in a cluster model of the kind popular in nuclear theory [10].

It is also now easier to explain what a symmetry of a Skyrmion is more precisely. A symmetry is a pairing of a rotation and an isorotation that leaves one of our pictures invariant. Rotations are rotating the Skyrmion in physical space and isorotations can be thought of as a rotation of the colours around the surface. Thus, for a symmetry of a Skyrmion it must be possible to compensate for a rotation by a recolouring of the surface by reorienting the Runge colour sphere. This notion of a symmetry will be important when we come to discuss quantisation of Skyrmions, which is the topic of this thesis, as it will provide constraints on the spin and isospin states that are permitted after quantisation.

1.2.2 Higher charge Skyrmions

We can also produce similar pictures for higher charge Skyrmions. Motivated by the cluster model, we can look at a few nuclei with B equal to a multiple of four, to see if the Skyrme model agrees with the evidence from nuclear physics that these nuclei are comprised of α-particle building blocks. Interestingly, it does. For $B = 8$ we see an object that looks like two cubes glued together and for $B = 12$, we find two configurations with very similar energies. One is with three cubes arranged in a triangle and one has the three cubes arranged

in a chain. In fact, it is known experimentally that Carbon-12 does indeed have two low-lying states, the ground state and the Hoyle state, which can be related to these two Skyrmion configurations. We show all of these pictures in Figure 1.2.

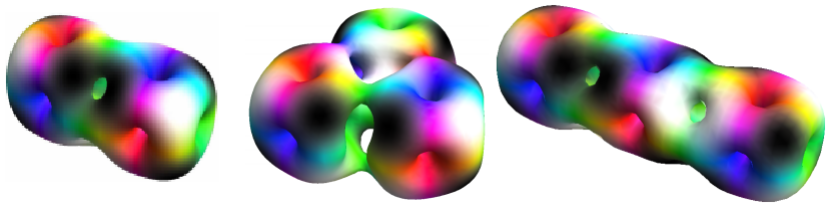

Figure 1.2: A plot of the $B = 8$ Skyrmion (left) and the triangle and chain configurations for $B = 12$ (centre and right respectively) [19],[58]. The triangle and chain configurations have similar energies.

For $B = 16$ there are various ways of sticking together four $B = 4$ cubes, and we display these in Figure 1.3. A key remark here is that experimentally the tetrahedron should be the minimal energy arrangement, with the square arrangement having slightly higher energy. However, in the Skyrme model the ordering is the opposite way around, although the energy gap is still small [31].

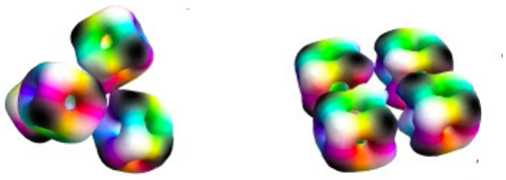

Figure 1.3: Plots for Skyrmion configurations with $B = 16$; the tetrahedron and the square [30].

One could go much further to plot much larger Skyrmions with $B = 4N$, and indeed as B tends to infinity it has been shown that Skyrmions form crystals with an infinite lattice of $B = 4$ cubes [49].

It is important to note that these pictures were all calculated with pion mass $m = 1$. For the case $m = 0$ things look somewhat different, as we do not see clusters but rather we find shell type solutions [9]. As m is increased from zero, we gradually transition from the shell type structures to cluster type ones.

1.3 Modifications to the Skyrme model

Since we want to relate these Skyrmions to real atomic nuclei, there is an important caveat to the model. The classical binding energies that we calculate for Skyrmions are substantially larger than the binding energies for real nuclei [47]. For example, in [9] it is calculated that the $B = 2$ Skyrmion has its binding energy overstated by more than 20%. This has motivated certain modifications that can be made to the Skyrme model in an attempt to remedy this, at least partially.

A popular idea is to add a sixth order term in to the Lagrangian which takes the form

$$\mathcal{L}_6 = \frac{3}{2}\,\mathrm{Tr}([R_\mu, R^\nu][R_\nu, R^\lambda][R_\lambda, R^\mu]), \tag{1.12}$$

and then construct a Lagrangian

$$\mathcal{L}_{BPS} = \mathcal{L}_6 + m\,\mathrm{Tr}(1-U), \tag{1.13}$$

and this is a BPS theory. For this particular case, the Bogomolny energy bound (1.9) is in fact saturated, which means that for this modified model the Skyrmions have zero binding energy. This now obviously understates the binding energies, but we can allow a small binding energy by adding a perturbative correction relating to the second order term

$$\mathcal{L} = \epsilon\mathcal{L}_2 + \mathcal{L}_6 + m\,\mathrm{Tr}(1-U), \tag{1.14}$$

where $\mathcal{L}_2$ is the same second order term we saw in the original model and ϵ is a small parameter. The idea, proposed in [1], is then to solve for the BPS solutions (where $\epsilon = 0$) and then increase ϵ to include the perturbation. However this is numerically very challenging as the BPS model is hard to solve numerically, and for $\epsilon = 0$ only the charge 1 solution is currently known, so more work needs to be done.

Another modification we can make to the original model is to adjust the potential (zeroth order) term. One well studied possibility is to take the new zeroth order term to be $\mathrm{Tr}(1-U)^4$ [24], [23]. This potential actually gives binding energies close to the experimentally determined values but has some different drawbacks. Firstly a quantisation of this model becomes very difficult as there are many local minima in each baryon sector, and so to include

all of these when doing quantisation would make the procedure impractical. Also, in this model the Skyrmions now look like collections of point particles, rather than the novel solutions we saw before where individual nucleons were not distinguishable. Losing this unique feature of the Skyrme model is undesirable.

Lastly, another idea is to include vector mesons by coupling them to the original Skyrme model. As one includes more mesons, the model approaches the BPS limit [64], and even the addition of just the first meson decreases the classical binding energy of the $B = 4$ cube fourfold [63]. More recent work by Naya and Sutcliffe in [54] and [55] has yielded further interesting results.

These modifications both have scope to reduce Skyrmion binding energies but come with other difficulties, and for the purposes of this thesis we shall study the original Skyrme model given by (1.4). We shall see in Chapter 2 that the process of quantisation also goes some way to lowering the high classical binding energies.

1.4 Thesis outline

So far we have discussed classical solutions of the Skyrme model, but clearly if we are to complete the identification with atomic nuclei we must quantise these solutions. It must be noted that one cannot quantise the Skyrme model in the conventional way by using full quantum field theory, as the Skyrme

model is not renormalisable. As such other methods must be considered. In Chapter 2 we will introduce the concept of Skyrmion quantisation. The simplest and most common approach is rigid body quantisation which produces a few plausible results for small nuclei, but has some significant limitations. In this thesis we want to build on recent work done on a method called vibrational quantisation, and we will present some results for different Skyrmions in this vibrational scheme.

We consider first a comparatively simple problem, namely $B = 2$. This is already reasonably well described by the rigid body approximation, but we apply the vibrational method to see if we can obtain some improved results.

We also investigate the $B = 16$ Skyrmion, identifiable with the Oxygen-16 nucleus. Some work on this has already been done but we make several significant generalisations. The general idea behind the improvements is to use two-dimensional rather than one-dimensional numerics to solve the problem, and this allows us to make an unrestricted choice for the potential, rather than the highly restricted potential that could be chosen in the previous framework. We also discuss an interesting approximate approach for Oxygen-16 using quantum graphs, that simplifies the problem considerably, by reducing it to solving ODEs.

We then give a brief discussion about how a very similar numerical method to that used for Oxygen-16 could be applied to Carbon-12 with only minor alterations, before ending with some concluding remarks and an outlook for potential future work in the area of vibrational quantisation.

Chapter 2

Quantisation of Skyrmions

As argued in Chapter 1, if we wish to turn the Skyrme model into a plausible model for atomic nuclei, we must give a quantum description of Skyrmions. So far, all of the solutions we have shown have been classical solutions of the model, and we will build on this base to construct a quantum description. That is to say we will take the classical solutions and then add in quantum corrections.

The simplest corrections arise from considering the zero modes of the Skyrmion. These are any transformations under which the energy of the configuration is invariant. Such transformations fall into four categories: discrete symmetries, translations, rotations and isorotations. Translations are trivial and we shall not consider them here. Parity is the relevant discrete symmetry that we will consider, and will play an important role in our future discussions. Rotation and isorotation zero modes lead to conserved angular

momentum J and isoangular momentum I.

To illustrate the size of the quantum corrections consider a quantity such as the mass of a nucleus. If one takes the classical mass of a Skyrmion as the first approximation of the experimental nuclear mass, the rotational and isorotational corrections give rise to a small corrections of order $\hbar^2$, where as usual $\hbar$ is the reduced Planck constant.

Further corrections to consider come from Skyrmion deformations. It is known that a Skyrmion can deform quite significantly, and this gives rise to extra degrees of freedom. Including general deformations is mathematically challenging but one method is to model deformations as harmonic vibrations, thus the corrections to the nuclear mass are of order $\hbar$. Lastly, interactions between Skyrmions and the pions give rise to a Casimir energy, which also leads to a correction of order $\hbar$.

Overall, the energy of a Skyrmion in the quantum picture is given schematically by its classical mass plus corrections as

$$E = M_B + \hbar \sum_i \omega_i \left(n_i + \frac{1}{2} \right) + \hbar^2 E_{J,I}, \tag{2.1}$$

where ω_i are frequencies of the harmonic vibrations, M_B is the mass of a Skyrmion of charge B and $E_{J,I}$ is the energy contribution from the spin and isospin zero modes. A subtle point is that although we call M_B a mass, it is in fact the static energy of the minimal energy Skyrmion configuration of charge B. This differentiates it from the pion mass, which is the mass of

the pion field as derived from the field theory interpretation of the Skyrme model. If we consider an infinite number of frequencies, then the constant part of the second term is the zero point energy or Casimir energy, when suitably renormalised.

The zero mode corrections have been well understood for some time but the vibrational corrections have only recently started to be analysed, with a notable early success being for the Lithium-7 nucleus in [29]. The calculation of the Casimir correction presents significant difficulties, since calculating it requires the Skyrme model to be renormalised but the model is not renormalisable. However it is a reasonable approximation that the Casimir correction is roughly the same for each state with a given topological charge, and so the correction does not change the order of states or the gaps between them when one is calculating a spectrum. In particular the relative positions of states should be accurate, and one can calibrate calculated values against experiment in order to ensure the values of the energies are also reasonable. Since we are going to be interested primarily in calculating energy spectra, we will not concern ourselves with the Casimir correction. This is because when we calculate a spectrum we are generally more interested in the relative positions of the states rather than their absolute values, and the Casimir correction should not significantly effect these. However for an analysis of how one might go about trying to include the Casimir term more rigorously, the reader is referred to [39] where Krusch and Speight attempt to include the Casimir energy correction for quantum lumps on the two-sphere. Another

useful paper is [52], in which the Casimir energy of the $B = 1$ Skyrmion is calculated, but nothing beyond this has been determined in the full Skyrme model.

2.1 Zero modes

Let us now consider in detail the respective corrections we have just outlined. Firstly, we consider the spin and isospin zero modes. To understand these we must introduce coordinates to describe the orientation of a Skyrmion in space and isospace. Both spaces can be parametrised by Euler angles and by convention we use (ψ, θ, ϕ) for the rotational angles and (α, β, γ) for the isorotational angles. A Skyrmion rotation can always be decomposed into three simple rotations: a rotation of ψ about the $(0, 0, 1)$ axis, then a rotation of θ around $(1, 0, 0)$ and finally a rotation of ϕ around the new $(0, 0, 1)$ axis. Similarly an isorotation can be decomposed in the same way, but the isorotations act on the pion vectors rather than the Skyrmion itself, and so can be visualised as moving the colours around the surface of the Skyrmion.

It is worth noting at this point that the Skyrme Lagrangian (1.4) has what is known as an isopsin symmetry. That is to say the Lagrangian is invariant under the transformation

$$U \to AUA^{\dagger}, \tag{2.2}$$

where A is a constant $SU(2)$ matrix. We saw this previously as the reduction of the full chiral symmetry (1.6). If we denote the 3×3 rotation and isorotation matrices by R^J and R^I respectively, then R^I is related to (2.2) by

$$R^I_{ij} = \frac{1}{2} \operatorname{Tr} \left(\tau_i A \tau_j A^{-1} \right) . \tag{2.3}$$

We can now write down the most general form of Skyrmion configurations that can be generated from a given starting configuration $U_0(\boldsymbol{x})$ by rotations and isorotations. It is given by

$$U(\boldsymbol{x}; \alpha, \beta, \gamma, \psi, \theta, \phi) = A(\alpha, \beta, \gamma) U_0(R^J(\psi, \theta, \phi)\boldsymbol{x}) A(\alpha, \beta, \gamma)^\dagger . \tag{2.4}$$

We call this the zero mode configuration space of Skyrmions, and quantising Skyrmions by including only these modes is known as zero-mode or rigid body quantisation, with the latter name deriving from the fact that this scheme allows the Skyrmions to rotate but not to deform or vibrate. We will briefly outline how this method works here, but for a full discussion the reader is referred to [48], where this method is first outlined for solitons, and also to [3] where it is first applied to Skyrmions directly.

2.1.1 Rigid body quantisation

We will now describe the general idea behind rigid body quantisation. We firstly allow all of our coordinates to depend on time, and then substitute

the ansatz (2.4) into (1.4). This reduces the Lagrangian to the form

$$\mathcal{L} = M_B + \frac{1}{2}(\boldsymbol{a}, \boldsymbol{c})\Lambda(\boldsymbol{a}, \boldsymbol{c})^T, \tag{2.5}$$

where $\boldsymbol{a}$ and $\boldsymbol{c}$ are the classical isospin and spin velocities respectively. We think of them as row vectors of the form $\boldsymbol{a} = (a_1, a_2, a_3)$, and they can be written down explicitly in component form as

$$a_j = -i\,\mathrm{Tr}(\tau_j A^\dagger \dot{A}) \text{ and } c_j = i\,\mathrm{Tr}(\tau_j \dot{C} C^\dagger), \tag{2.6}$$

where C is the rotational analogue of the isospin matrix A in (2.2). Λ is the moment of inertia tensor and is given by

$$\Lambda = \begin{bmatrix} U & -W \\ -W^T & V \end{bmatrix}, \tag{2.7}$$

where U, V and W can be defined in component form as

$$U_{ij} = -\int \mathrm{Tr}\left(T_i T_j + \frac{1}{4}[R_k, T_i][R_k, T_j]\right) d^3x \tag{2.8}$$

$$V_{ij} = -\int \epsilon_{ilm}\epsilon_{jnp} x_l x_n \,\mathrm{Tr}\left(R_m R_p + \frac{1}{4}[R_k, R_m][R_k, R_p]\right) d^3x \tag{2.9}$$

$$W_{ij} = \int \epsilon_{jlm} x_l \,\mathrm{Tr}\left(T_i R_m + \frac{1}{4}[R_k, T_i][R_k, R_m]\right) d^3x, \tag{2.10}$$

where $T_i = \dfrac{i}{2}[\tau_i, U_0]U_0^{-1}$.

If we now move into the Hamiltonian formulation, the classical Hamiltonian is now

$$\mathcal{H} = M_B + \frac{1}{2}(\boldsymbol{K}, \boldsymbol{L})\Lambda^{-1}(\boldsymbol{K}, \boldsymbol{L})^T, \tag{2.11}$$

where $\boldsymbol{K}$ and $\boldsymbol{L}$ are the classical body-fixed isoangular and angular momenta respectively. There are also the usual space-fixed equivalent momenta denoted respectively by $\boldsymbol{I}$ and $\boldsymbol{J}$. These are related to the body-fixed momenta through the rotation matrices by $\boldsymbol{I} = R^I\boldsymbol{K}$ and $\boldsymbol{J} = R^J\boldsymbol{L}$.

The Hamiltonian (2.11) can then be quantised canonically. This means that the momenta are now operators and the Hamiltonian becomes

$$\hat{\mathcal{H}} = M_B + \frac{\hbar^2}{2}(\hat{\boldsymbol{K}}, \hat{\boldsymbol{L}})\Lambda^{-1}(\hat{\boldsymbol{K}}, \hat{\boldsymbol{L}})^T = M_B - \frac{\hbar^2}{2}\nabla^2, \tag{2.12}$$

where ∇^2 is the Laplacian operator on the space of rotations and isorotations.

The momentum operators can be described using the angles we introduced previously. If one consider the space-fixed momentum operators, the third components can be written as $\hat{J}_3 = -i\hbar\partial_\psi$ and $\hat{I}_3 = -i\hbar\partial_\gamma$. These two objects are particularly interesting as they both commute with the Hamiltonian, as do the squares of both angular momentum operators $\hat{\boldsymbol{J}} \cdot \hat{\boldsymbol{J}} = \hat{\boldsymbol{L}} \cdot \hat{\boldsymbol{L}}$ and $\hat{\boldsymbol{I}} \cdot \hat{\boldsymbol{I}} = \hat{\boldsymbol{K}} \cdot \hat{\boldsymbol{K}}$. This tells us that there are four conserved quantities for each energy eigenstate. These are denoted by the quantum numbers J_3, I_3, $J(J+1)$ and $I(I+1)$, where $-J \leq J_3 \leq J$ and $-I \leq I_3 \leq I$.

We will not discuss in detail how to solve this Hamiltonian here, as it is quite complicated, but has been studied in great depth elsewhere with a good

source being [41]. It turns out that the Schrödinger equation corresponding to (2.12) has solutions composed of Wigner-D functions that depend on the momenta, denoted by $D^J_{L_3,J_3}(\psi,\theta,\phi)$ for the rotational basis and $D^I_{K_3,I_3}(\alpha,\beta,\gamma)$ for the isorotational basis. Wavefunctions will then be

$$\Psi = \sum_{L_3,K_3} c_{L_3,K_3} D^J_{L_3,J_3}(\psi,\theta,\phi) D^I_{K_3,I_3}(\alpha,\beta,\gamma), \tag{2.13}$$

which we abbreviate for convenience to

$$|\Psi\rangle = \sum_{L_3,K_3} c_{L_3,K_3} \left|J, L_3, J_3\right\rangle \left|I, K_3, I_3\right\rangle, \tag{2.14}$$

where c_{L_3,K_3} are constants.

It can now be recognised that this wavefunction is the same as that of a generalised rigid rotor, and so we can immediately write down the rotational energy

$$E_{\text{rot}} = -\frac{\hbar^2}{2} \left\langle \Psi \right| \nabla^2 \left| \Psi \right\rangle, \tag{2.15}$$

where $|\Psi\rangle$ here is an eigenfunction of the Laplacian.

In the case of Skyrmions however, there are many additional constraints resulting from the symmetries of the Skyrmion configuration. These symmetries place restrictions on the allowed values of spin J and isospin I, and also on the constants c_{L_3,K_3}. Indeed for highly symmetric configurations such as $B = 1$ and $B = 4$ there are many constraints and these will tell us the allowed quantum states $|J, I\rangle$ permitted by the rigid body quantisation of

the Skyrme model, which we can then compare with experimental data.

2.1.2 Finkelstein-Rubinstein constraints

Let us now consider how these constraints work in practice. A single $B = 1$ Skyrmion is intended to model a single proton or neutron, both of which are fermions and thus have half-integer spins. By contrast, bosons have integer spins. More generally a Skyrmion of charge B can be thought of as describing a nucleus of B nucleons, meaning that such a Skyrmion is a fermion if B is odd (as it will consist of an odd number of constituent particles with half-integer spins and so retain an overall half-integer spin) and a boson if B is even (as it will consist of an even number of constituent particles with half-integer spins and so have an overall integer spin). In quantum mechanics, bosons and fermions are defined by their exchange statistics and spins. For exchange statistics, the definition is that if two identical bosons are exchanged in a system, the wavefunction is invariant, whereas an exchange of two identical fermions will result in the wavefunction changing by a factor of -1. It then follows from the spin-statistics theorem that bosons must have integer spins and fermions must have half-integer spins. One further property that results from these definitions is that we also have the constraint that the wavefunction of a boson should be invariant under a 2π rotation, whereas for a fermion the wavefunction should change by a factor of -1. In quantum field theory, bosons are conventionally described by scalar, vector or tensor fields whereas fermions are described by spinors. We want to quantise Skyrmions

as atomic nuclei composed of fermions, but the Skyrme model is a scalar field theory so this would seem to be a problem.

The first work on this subject was by Finkelstein and Rubinstein [20]. They realised that solitons could be quantised as fermions or bosons in a consistent way. They suggested that one should look at the covering of configuration space rather than the configuration space itself. Let us denote the configuration space of Skyrmion configurations of charge B by Q_B, and then note that this space has fundamental group $\pi_1(Q_B) \cong \mathbb{Z}_2$, which means that the covering space CQ_B is a double cover.

Consider now two points $\tilde{q}_1$ and $\tilde{q}_2$ in CQ_B, corresponding to the point q in Q_B, as shown in Figure 2.1.These two points are connected by a path in CQ_B which projects to a non-contractible loop in Q_B. This insight allows us to think of symmetries of configurations as induced loops in configuration space, but the symmetry also acts on the covering space and the key point is that if we apply the symmetry to $\tilde{q}_1$ we get $\tilde{q}_1$ if the induced loop is contractible and $\tilde{q}_2$ if it is not [38].

If we now define a wavefunction as a map $\psi : CQ_B \to \mathbb{C}$, $\tilde{q} \longmapsto \psi(\tilde{q})$, we can impose the fermionic constraint that $\psi(\tilde{q}_1) = -\psi(\tilde{q}_2)$. We call this a Finkelstein-Rubinstein constraint, and we are now interested in how this constraint affects general rotations and isorotations. It turns out that if we consider a rotation by θ_J about axis $\boldsymbol{n}$ in space combined with an isorotation

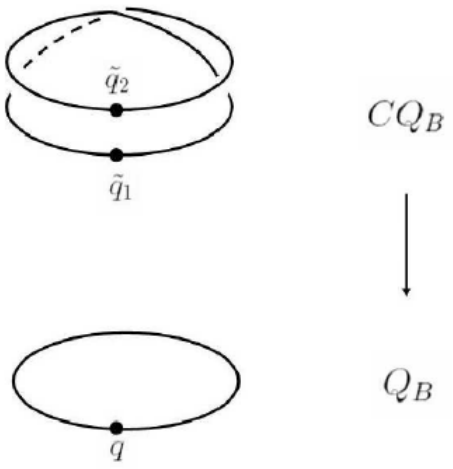

Figure 2.1: A visual representation of the double covering space CQ_B in relation to configuration space Q_B. We see that two points in CQ_B correspond to the same point in Q_B [38].

by θ_I about axis $\boldsymbol{N}$ in isospace we find that

$$\exp(-i\theta_J \boldsymbol{n} \cdot \hat{\boldsymbol{J}}) \exp(-i\theta_I \boldsymbol{N} \cdot \hat{\boldsymbol{I}}) \psi(\tilde{q}) = \chi_{FR} \psi(\tilde{q}), \tag{2.16}$$

where $\chi_{FR} = +1$ if the induced loop is contractible and -1 if it is not. This process produces the correct basic results. It was shown in [25] that a 2π rotation of a Skyrmion gives $\chi_{FR} = +1$ for even B and -1 for odd B. In [37] the same thing was shown for a 2π isorotation. Additionally Finkelstein and Rubinstein themselves showed in [20] that an exchange of two identical Skyrmions gives $\chi_{FR} = +1$ for even B and -1 for odd B. These all agree with the basic principles of quantum mechanics we discussed at the start of this subsection. These restrictions tells us that a Skyrmion with even

or odd baryon number B must have integer or half-integer spin and isospin respectively.

Furthermore in addition to these well known quantum mechanical results that must always hold, there are additional constraints related to the symmetry group of a Skyrmion. There are additional actions which leave Skyrmions invariant beyond the ones just discussed. For example, for the $B = 4$ Skyrmion, which has cubic symmetry, it can be seen that the Skyrmion is invariant under the action of a $2\pi/3$ rotation about the $(1, 1, 1)$ axis followed by a $2\pi/3$ isorotation about the $(0, 0, 1)$ axis. Using the same rules as before, the wavefunction must satisfy

$$\exp\left(\left(2\pi i/\left(3^{3/2}\right)\right)(1,1,1)\cdot\hat{\boldsymbol{L}}\right)\exp((2\pi i/3)\,\hat{K}_3)\,|\Psi\rangle = (-1)^N\,|\Psi\rangle\,, \quad (2.17)$$

where N is equal to 0 or 1. We call N the Finkelstein-Rubinstein number and we call relations of this form Finkelstein-Rubinstein constraints. We can ask how we determine N, and there are several ways of doing so. One method is to approximate the Skyrmion using rational maps [32] and then use the formula derived in [37] to obtain N. It is given by

$$N = \frac{B}{2\pi}(B\alpha - \beta), \quad (2.18)$$

where α and β denote the angles of a rotation and isorotation respectively, and the rational map is required to satisfy a suitable base condition [37]. This method has been generalised further in [36] to be applicable to Skyrme

configurations composed of clusters of rational map Skyrmions, which approximate Skyrmions in Skyrme models with a pion mass.

One can derive Finkelstein-Rubinstein constraints for all of the symmetries of a particular Skyrmion, and once this is done we can deduce the allowed spin and isospin values. A natural first step is to consider the ground state predictions of rigid body quantisation, and compare them to the known ground states found experimentally. We do this for the first nine Skyrmions in Table 2.1. We see that we match the experimental states for $B = 1 \dots 4$ and $B = 6$ and 8 but the model fails for $B = 5, 7$ and 9. Recall that these are only the predictions of the rigid body quantisation of the Skyrme model, not the full predictions of the model. We must now consider how appropriate rigid body quantisation is as a method, and this will give us some insight into why the rigid body model does not agree with experiment for most odd nuclei. We will next consider going beyond zero modes and including some additional modes that allow the Skyrmions to deform and vibrate.

2.2 Vibrational modes

So far we have allowed our Skyrmions to spin and isospin as we quantise them. However, this is obviously not the full picture, as we have already seen that Skyrmions can deform, for example by breaking down into their constituent $B = 1$ Skyrmions, or by changing their shape as they spin [5] or isospin [4]. As such we must consider the space of deformed Skyrmion configurations.

B	Model $\lvert J, I\rangle$	Exp. $\lvert J, I\rangle$	Nucleus	Match?
1	$\lvert 1/2, 1/2\rangle$	$\lvert 1/2, 1/2\rangle$	^{1}H	Y
2	$\lvert 1, 0\rangle$	$\lvert 1, 0\rangle$	^{2}H	Y
3	$\lvert 1/2, 1/2\rangle$	$\lvert 1/2, 1/2\rangle$	^{3}He	Y
4	$\lvert 0, 0\rangle$	$\lvert 0, 0\rangle$	^{4}He	Y
5	$\lvert 1/2, 1/2\rangle$	$\lvert 3/2, 1/2\rangle$	^{5}He	N
6	$\lvert 1, 0\rangle$	$\lvert 1, 0\rangle$	^{6}Li	Y
7	$\lvert 7/2, 1/2\rangle$	$\lvert 3/2, 1/2\rangle$	^{7}Li	N
8	$\lvert 0, 0\rangle$	$\lvert 0, 0\rangle$	^{8}Be	Y
9	$\lvert 1/2, 1/2\rangle$	$\lvert 3/2, 1/2\rangle$	^{9}Be	N

Table 2.1: A table of the predicted and experimental ground state spins and isospins for $B = 1$ to $B = 9$.

Since a single $B = 1$ Skyrmion has 6 degrees of freedom, three translational and three isorotational, a charge B Skyrmion has $6B$ degrees of freedom if we model the individual $B = 1$ Skyrmions as point particles with internal isospin degrees of freedom. If we allow the individual Skyrmions themselves to deform then this number will increase further [26]. Also note that the zero modes are distinct from the deformations and can be separated out by considering a vibrational manifold, which we denote by $\mathcal{M}$, with the addition of a fibre containing the zero modes.

The method of vibrational quantisation as we shall study it was proposed by Halcrow for the $B = 7$ Skyrmion in [29]. The idea is that in order to include deformations one must solve the Schrödinger equation on the total space, rather than just considering the spaces of rotations and isorotations as before. If we put a coordinate $\boldsymbol{s}$ on $\mathcal{M}$ along with a metric g, the kinetic operator (for small energies) is the well known Laplace-Beltrami operator

given by

$$\Delta = \frac{1}{\sqrt{|g|}} \partial_i \left(\sqrt{|g|} g^{ij} \partial_j \right), \tag{2.19}$$

where $\boldsymbol{\partial} = \left(\frac{\partial}{\partial s}, \nabla \right)$ and ∇ is the gradient on the combined zero mode space of rotations and isorotations. The potential energy is the static energy of the deformed Skyrmion at position $\boldsymbol{s}$ on $\mathcal{M}$ (for the minimal energy Skyrmion configuration this is the M_B that we saw in equation (2.1)), and the Schrödinger equation takes the form

$$\left(-\frac{\hbar^2}{2} \Delta + V(\boldsymbol{s}) \right) \Psi = E\Psi, \tag{2.20}$$

where Ψ is the total wavefunction. This equation has been known about for some time but is very difficult to work with and solve. The metric is $6B$ dimensional and in general has no nice properties, and if we hope to solve (2.20) then we must make some simplifying approximations. For example, one simplified case is seen in [44], where (2.20) is solved on a one-dimensional sub-manifold of the vibrational manifold for $B = 2$. A caveat here is that the authors of this paper are working in the instanton approximation. This work provides some new insight into the deuteron compared to rigid body quantisation but can be generalised much further, as we shall discuss later in this thesis.

In [29], Halcrow makes some further simplifications which we shall also follow. He assumes that $\mathcal{M}$ is Euclidean and that the metric g is block

diagonal, such that the kinetic operator separates into distinct rotational and vibrational parts. This assumption ensures that wavefunctions will likewise be separable into a vibrational part and a spin part, that is

$$\Psi = \sum_i u_i(\boldsymbol{s}) \left|\Theta\right\rangle_i , \tag{2.21}$$

where we call u_i the vibrational wavefunctions and $\left|\Theta\right\rangle_i$ the spin wavefunctions. We refer to the total wavefunction as a rovibrational state. Note that the spin states are precisely those spin states found for the zero modes, as the vibrational contributions have been separated out. The rotational equation is

$$-\nabla^2 \left|\Theta\right\rangle_i = E_{J,I}(\boldsymbol{s}) \left|\Theta\right\rangle_i , \tag{2.22}$$

where $E_{J,I}$ is the rotational contribution to the total energy and depends on $\boldsymbol{s}$ via the moment of inertia tensor (2.7).

More interesting is the vibrational Schrödinger equation which is given by

$$-\frac{\hbar^2}{2}\nabla_E^2 u(\boldsymbol{s}) + \left(V(\boldsymbol{s}) - \frac{\hbar^2}{2}E_{J,I}(\boldsymbol{s})\right) u(\boldsymbol{s}) = E_{\text{vib}} u(\boldsymbol{s}), \tag{2.23}$$

where ∇_E^2 is the Laplacian on Euclidean space and E_{vib} is the vibrational contribution to the total energy.

This equation (2.23) can be solved exactly with the aid of two further assumptions. First we assume that the deformations we are considering vary the moment of inertia tensor only slightly, meaning that we can approximate

$E_{J,I}(\boldsymbol{s})$ to be constant, up to some small corrections that can be added in later using perturbation theory. Secondly we must make a suitable choice for the potential. The paper [29] argues that a good assumption for the potential is to take it to be harmonic around its minimum (which is the minimal energy Skyrmion configuration for the relevant value of B) which can be taken to be at $\boldsymbol{s} = 0$ without loss of generality. We will argue in this thesis that this can be generalised further. Observe that both of these assumptions are reasonable for small deformations. This is true near the origin of $\mathcal{M}$, which is where one would expect to find low energy solutions. As such, if we wish to calculate an energy spectrum using this method, it should be valid to do so for low energy states.

We will give some further details on the way in which to perform these calculations in Chapter 3 when we consider applying this method to the case of $B = 2$ but for further background the reader is referred to [29]. It is useful at this point though, to make a brief reconnection with rigid body quantisation and see how the two techniques compare. Clearly the method of vibrational quantisation is much more involved than the rigid body approach, so is this extra effort justified by additional insights? A positive observation is that the binding energy of a Skyrmion that has been vibrationally quantised will be lower than one that has been quantised in the rigid body scheme. If we use a vibrational scheme where the Skyrmion is allowed to decompose into its constituent $B = 1$ parts, then we must include $6B - 9$ vibrational modes [28]. By considering the terms in (2.1) and neglecting the Casimir

term, the energy of a charge B Skyrmion will be

$$E_B = M_B + \frac{1}{2}\hbar\bar{\omega}(6B-9) + \frac{\hbar^2}{2}E_{J,I}, \tag{2.24}$$

where $\bar{\omega}$ is an averaged frequency over the $6B-9$ vibrations, which are approximated here to be harmonic. Again, M_B is the mass of a charge B Skyrmion. By comparison the energy of B charge one Skyrmions is given by

$$BE_1 = BM_1 + BE_{J,I|B=1}, \tag{2.25}$$

where $E_{J,I|B=1}$ and M_1 denote the rotational energy and mass of a $B=1$ Skyrmion respectively. This formula is valid only for $B \geq 2$, as we cannot define a vibrational energy for $B=1$ since it cannot be broken down any further. From these formulae we can see that the binding energy ($BE_1 - E_B$) of a charge B Skyrmion is lowered by an amount $\frac{1}{2}\hbar\bar{\omega}(6B-9)$ in the vibrational scheme compared to the rigid body scheme. This brings the binding energies of the Skyrme model closer to those of experimental data.

One other point to make is that vibrational quantisation tells us something about where the rigid body regime is appropriate and where it falls down. In particular it can be argued that rigid body quantisation fails if there is more than one Skyrmion configuration for a given B with a high degree of symmetry, and the effect is increased if the symmetric configurations lie close together on $\mathcal{M}$. For example, we shall later study the Oxygen-16 nucleus and for $B=16$ there are multiple highly symmetric configurations

as we saw in Figure 1.3. Because these configurations lie reasonably close together on $\mathcal{M}$ the effect is significant and the rigid body approach does not work well. A final remark is that zero mode quantisation always predicts an infinite tower of states, whereas vibrational quantisation for realistic potentials will only give a finite number of bound states.

2.3 Summary

We have introduced the concept of quantisation in the Skyrme model and observed some of the limitations of the rigid body approach. It predicts incorrect spins for the $B = 5$ and $B = 7$ ground states, with the latter having already been corrected by vibrational quantisation in [29]. We will consider the cases of $B = 2$ and $B = 16$, as well as touching on $B = 12$. We must also always recall that Skyrmion symmetries are important when discussing quantisation, and Skyrmions with multiple highly symmetric configurations must be treated with care.

Chapter 3

Vibrational quantisation of the B=2 Skyrmion

3.1 The B=2 Skyrmion

Let us consider the interaction of two charge one Skyrmions. Two separated charge one Skyrmions will experience the greatest attractive force if one Skyrmion is rotated by π radians relative to the second Skyrmion, around a line perpendicular to the line joining them [44]. This set up is known as the attractive channel, and for the $B = 2$ case the configuration will interpolate between a pair of charge one Skyrmions and the toroidal $B = 2$ Skyrmion which is the lowest energy $B = 2$ configuration as shown in Figure 3.1. Note that for a head on collision, the two Skyrmions scatter at an angle perpendicular to the line of their approach. In the case of off-centre collisions,

the scattering is more complicated [21].

Figure 3.1: A representation of the scattering of two $B = 1$ Skyrmions, which coalesce together to form a $B = 2$ torus before moving apart perpendicular to the original direction [21].

It is worth noting that the $B = 2$ configuration has a relatively high degree of symmetry. There are certain combinations of reflections in space and in isospace which leave the Skyrme field U invariant, which we will now consider. Let us follow [44] by defining a transformation O_{ai} as a simultaneous rotation by π around the a-th axis in isospace and the i-th axis in physical space. Note that O_{0i} denotes a rotation by π around the i-th axis in physical space with no rotation in isospace and similarly O_{a0} denotes a rotation by π around the a-th axis in isospace with no rotation in physical space.

Let us also define the parity operator P as

$$P : U(\mathbf{x}) \to U^{\dagger}(-\mathbf{x}), \tag{3.1}$$

noting that this is the combined parity operator in space and isospace, which

we can think of as acting in the following way;

$$P : (\pi_1, \pi_2, \pi_3) \to (-\pi_1, -\pi_2, -\pi_3) \text{ and } (x_1, x_2, x_3) \to (-x_1, -x_2, -x_3). \tag{3.2}$$

We can then define a transformation $P_{ai} = PO_{ai}$, and note that under certain such transformations the Skyrmion field remains invariant. In particular these transformations are

$$P_{21} : (\pi_1, \pi_2, \pi_3) \to (\pi_1, -\pi_2, \pi_3) \text{ and } (x_1, x_2, x_3) \to (-x_1, x_2, x_3), \tag{3.3}$$

$$P_{22} : (\pi_1, \pi_2, \pi_3) \to (\pi_1, -\pi_2, \pi_3) \text{ and } (x_1, x_2, x_3) \to (x_1, -x_2, x_3), \tag{3.4}$$

$$P_{33} : (\pi_1, \pi_2, \pi_3) \to (\pi_1, \pi_2, -\pi_3) \text{ and } (x_1, x_2, x_3) \to (x_1, x_2, -x_3), \tag{3.5}$$

where π_i are the pion fields, which we can think of as coordinates in isospace, and x_i are the coordinates in physical space [44].

These symmetries help us to determine what the Finkelstein-Rubinstein constraints are for $B = 2$, in line with the discussion in Chapter 2. For example, the O_{21} symmetry could be encoded as

$$e^{\pi i \hat{L}_1} e^{\pi i \hat{K}_2} \Psi = \chi_{FR} \Psi, \tag{3.6}$$

where $\hat{L}_1$ and $\hat{K}_2$ are the relevant components of the angular momentum and isoangular momentum operators. This can the be combined with parity. In our case here we have $\chi_{FR} = +1$ as $B = 2$ is even, and it is known that

an even B produces a Finkelstein-Rubinstein number of +1 [38], [37]. The symmetries of the configuration are of course important when we consider quantisation because of the constraints they provide, but we shall see for our vibrational quantisation they will restrict the form of the metric to something manageable.

3.2 Vibrational quantisation for $B = 2$

Our goal is to quantise the B=2 Skyrmion configuration taking into consideration one vibrational mode. In particular it makes sense to consider a vibration along a direction that best preserves the toroidal symmetry of the problem as this will be the lowest energy vibrational mode.

The manifold we must quantise can be thought of as being parametrised by a vibrational coordinate, which as before denote by $\mathbf{s}$ so as to be consistent with [29], as well as the three rotational (ϕ,θ,ψ) and three isorotational (α,β,γ) angles that we saw before. As before we allow all of these parameters to vary with time, which allows us to define an isoangular velocity $\mathbf{a}$ and angular velocity $\mathbf{c}$. We can then express the kinetic energy in a way that depends on the metric on our vibrational manifold which in turn depends on $\mathbf{s}$ as

$$T = \frac{1}{2}(\dot{\mathbf{s}}, \mathbf{a}, \mathbf{c})g(\mathbf{s})(\dot{\mathbf{s}}, \mathbf{a}, \mathbf{c})^T, \tag{3.7}$$

where as usual the dots denote time derivatives, and where $g(\mathbf{s})$ is the metric. This is now the analogue of the second term in the Lagrangian (2.5).

We then know from our previous discussion that the kinetic operator is proportional to the Laplace-Beltrami operator (2.19) and the Schrödinger equation takes the form (2.20).

In general for problems such as these we can split the metric into submatrices whose forms are restricted by the symmetry of the configuration. The standard convention is to write our 7-dimensional matrix as follows [11]

$$g = \begin{pmatrix} \lambda & 0 & 0 \\ 0 & U & -W \\ 0 & -W^T & V \end{pmatrix}, \tag{3.8}$$

where U, V and W are all 3×3 matrices and λ is a scalar. Observe that the lower right 6×6 block of this matrix is exactly the moment of inertia tensor (2.7) that we encountered for the rigid body case, and the quantity λ is a new object unique to the vibrational method. It is defined [29] as

$$\lambda = -\int \mathrm{Tr}(R_\tau R_\tau + [R_\tau, R_i][R_\tau, R_i]) d^3x. \tag{3.9}$$

We make the assumptions outlined previously that the wavefunction is separable into vibrational and rotational parts (2.21). We also notice that for the $B = 2$ case the vibrational manifold is one-dimensional and is defined simply by the separation of the two Skyrmions. This means that our parameter $\mathbf{s}$ is in fact a scalar quantity s. The Schrödinger equation thus becomes

a 1-dimensional equation

$$\left(-\frac{\hbar^2}{2\sqrt{|g|}}\frac{d}{ds}\left(\frac{\sqrt{|g|}}{\lambda}\frac{d}{ds}\right)+V(s)+E_J(s)\right)u(s)=Eu(s). \tag{3.10}$$

In order to set about solving such an equation, we must first determine $g(s)$,$V(s)$ and $E_J(s)$ by using a numerical simulation. The two charge one Skyrmions in the attractive channel represent our initial configuration, and this is then evolved in fictitious time τ in such a way as to reduce the potential energy of the system before ending at a stationary point.

It should be noted that once we have numerically determined the relevant quantities it is prudent to change our variable from numerical time τ to a more convenient distance parameter. We first define a distance d from τ using

$$d(\tau)=\int^{\tau}\sqrt{\lambda(\tau')}d\tau'. \tag{3.11}$$

We call this distance measure a geodesic distance, and it has the advantage of effectively scaling λ out of the Schrödinger equation by setting it to be equal to one. There are other possible distance measures we could consider, such as the distance between the centres of mass of the two Skyrmions or the distance between pre-images of the anti-vacuum, but we shall use the geodesic distance here.

We must be careful in choosing the limits of our integration as d and τ do not behave in the same way. First we must observe that we start off at time $\tau=0$ with two well separated Skyrmions, so we want this to correspond to d

being maximal. If we take the equation (3.11) then d increase as τ increases, so to get the inverse behaviour we want we perform a change of variables. If we define $d_{\max}$ as the maximum value of d and $\tau_{\max}$ as the maximal value of the numerical time, then we can define the new variable $\tilde{d} = d_{\max} - d$. This new variable now has the correct relationship to τ, that is $\tilde{d} = d_{\max}$ at $\tau = 0$ and $\tilde{d} = 0$ at $\tau = \tau_{\max}$.

A second point is that the distance measure $\tilde{d}$ does not yet define a physical distance, only a numerical one. That is, if we took the two Skyrmions to have an initial physical separation of $s_{\max}$ we would not find our value of $d_{\max}$ to be equal to $s_{\max}$. In order to scale the distance to be physically meaningful, we will perform a second change of variables which will introduce a scaling factor. We define a new variable $s = \beta\tilde{d}$, where $\beta = s_{\max}/d_{\max}$, and this new variable s now has the properties we desire. Relating back to the original equation (3.11), the equation for s in terms of d is given by

$$s = \frac{s_{\max}}{d_{\max}}(d_{\max} - d) = \beta(d_{\max} - d) = s_{\max} - \beta d. \tag{3.12}$$

This new variable s is the rescaled geodesic distance, and in future when we refer to the geodesic distance, this is the quantity we are referring to.

If we then expand (3.10) and perform the change of variables, the Schrödinger equation becomes

$$\left(-\frac{\hbar^2}{2}\beta^2\frac{d^2}{ds^2} - \frac{\hbar^2}{4}\beta^2\frac{d}{ds}\left(\log(|g|)\right)\frac{d}{ds} + V(s) + E_J(s)\right)u(s) = Eu(s), \tag{3.13}$$

which we can more conveniently solve numerically. We observe that the equation can be reformulated as a Sturm-Liouville problem

$$-\frac{d}{ds}\left(p(s)\frac{du}{ds}\right)+q(s)u(s)=Ew(s)u(s), \tag{3.14}$$

where p,q and w are functions which can be determined from (3.13) and are given by

$$p(s)=\sqrt{(|g(s)|)}, \tag{3.15}$$

$$q(s)=\frac{2}{\beta^2\hbar^2}(V(s)+E_J(s))\sqrt{(|g(s)|)}, \tag{3.16}$$

$$w(s)=\frac{2}{\beta^2\hbar^2}\sqrt{(|g(s)|)}. \tag{3.17}$$

By considering the aforementioned symmetries of the $B=2$ Skyrmion it can be demonstrated that the only components of the metric that we need to calculate are λ, U_{11}, U_{22}, U_{33}, V_{11}, V_{22}, V_{33} and W_{33} as all of the other components will be zero. As such, these functions were calculated using a gradient flow numerical method [1]. We begin the simulation with two $B=1$ Skyrmions at a geodesic distance $s=5$ apart (i.e at positions $+2.5$ and -2.5 such that $s_{\max}=5$) and allow the configuration to relax into the $B=2$ torus ($s=0$). In doing so we numerically calculate the relevant functions as functions of gradient flow time. Then using equation (3.12) we can obtain the value of s at each time step, and hence easily convert all of our functions into

[1]Note that the gradient flow numerical data comes from Chris Halcrow, whereas the use of this data to numerically solve the Sturm-Liouville problem was my own work.

functions of the geodesic distance. We find that in our simulation the value of $d_{\max}$ is 554.4, giving a value of $\beta = 0.009019$ to four significant figures.

We will also need to explicitly write down an expression for $E_J(s)$ in terms of the functions that we calculate numerically. The paper [44] will be our guide here. The authors correctly identify that the possible two nucleon bound states can fall into two possible categories, either having spin $J = 1$ and isospin $I = 0$ or spin $J = 0$ and isospin $I = 1$. The first case ($(J, I) = (1, 0)$) can be identified with the deuteron, and the second case can be identified with an alternative nucleon-nucleon bound state. Since the expression for $E_J(s)$ will obviously depend on J, the expression will be different for each of these two cases. If we adapt the notation from [44] into our own style, the expressions we find are

$$E_J(s)(J = 1, I = 0) = \frac{\hbar^2}{2}\left(\frac{1}{V_{11}} + \frac{1}{V_{22}}\right) \tag{3.18}$$

and

$$E_J(s)(J = 0, I = 1) = \frac{\hbar^2}{2}\left(\frac{1}{U_{11}} + \frac{1}{U_{22}}\right), \tag{3.19}$$

and we will use these expressions in calculating results.

Another point we need to consider before we can produce results is boundary conditions. Obviously, we will want to impose the condition that as $s \to \infty$ the wavefunction and its derivative will go to zero, that is $u(\infty) = 0$ and $u'(\infty) = 0$. However, we must also think about the condition we should impose at $s = 0$. We know that the torus is the minimal energy configuration

of the $B = 2$ Skyrmion and this corresponds to $s = 0$, so we would expect our wavefunction to be maximal at that point. This gives us the boundary condition $u'(0) = 0$. It is important to check when imposing this condition that the torus is allowed by the Finkelstein-Rubinstein constraints, but it does turn out that for both the $(J, I) = (1, 0)$ and $(J, I) = (0, 1)$ states the torus is an allowed configuration. Therefore the derivative boundary condition is perfectly reasonable, and that is what we shall use going forward.

3.3 Previous work on $B = 2$

Two notable papers that have done previous work on the $B = 2$ Skyrmion are [44] and [11]. In particular [44] gives formulae for how all of the functions we have calculated should behave asymptotically (with the exception of λ). This will allow us to check that our numerically calculated functions look plausible. A point of caution is that all of this work was for pion mass $m = 0$ whereas for our calculations we shall be using pion mass $m = 1$ in order to break new ground. Explicit formulae for the asymptotics for $m = 1$ are not known exactly, but are known to be qualitatively similar to the massless case for leading order. In [44], they write down the following asymptotic formulae for the spin (V_{ii}) and isospin (U_{ii}) moments of inertia

$$U_{11} \sim 2\Lambda \ , \ U_{22} \sim 2\Lambda \ , \ U_{33} \sim 2\Lambda, \tag{3.20}$$

$$V_{11} \sim 2\Lambda \ , \ V_{22} \sim 2\Lambda + \frac{1}{2}Ms^2 \ , \ V_{33} \sim 2\Lambda + \frac{1}{2}Ms^2, \tag{3.21}$$

$$W_{33} \sim -2\Lambda, \tag{3.22}$$

where M is the mass of a single Skyrmion and Λ is the moment of inertia of a single Skyrmion. For pion mass $m = 1$ these values are $M = 1.416 \times 12\pi^2 = 167.7$ and $\Lambda = 47.6$ [8]. Some of these formulae have corrections of order $1/s$ or $1/s^3$, but we do not include these here, and these corrections would in any case be different for $m \neq 0$ and would include exponential factors of the form $\exp(-ms)$. For the asymptotics of the energy, [21] gives the formula

$$V \sim 2M - \frac{2C^2}{3\pi}\exp(-ms)(m^2s^2 + 2ms + 2)\frac{1}{s^3}, \tag{3.23}$$

where C is a constant depending on m, and is given as $C = 1.79$ for $m = 1$.

The paper [44] also gives us a guide for calibration. We recall from Chapter 1 that the length and energy scales of our model are $F_\pi/4e$ and $2/eF_\pi$ respectively, and now in the quantum picture we have also introduced the parameter $\hbar$. Using the values found in [2], we find that our Skyrme units are related to physical units by

$$\frac{F_\pi}{4e} = 5.58 \text{ MeV and } \frac{2}{eF_\pi} = 0.755\text{fm}, \tag{3.24}$$

and this leads us to

$$\hbar = 197.3 \text{ MeV fm } = 46.8 \left(\frac{F_\pi}{4e}\right)\left(\frac{2}{eF_\pi}\right). \tag{3.25}$$

In these units, it therefore follows that $\hbar = 46.8$, and following [44] this is the value that we will take in our work on $B = 2$.

3.4 Results

3.4.1 The numerically generated functions

Keeping in mind the asymptotic formulae just given, we now display some plots of the numerically generated functions. We display results in Figure 3.2.

We see that all of these plots match up with the asymptotics (where they are known) to a reasonable degree of numerical accuracy, with the worst matches being for U_{11} and U_{22} which still agree to within approximately 2%. This gives us confidence to now go ahead and solve (3.10) for the vibrational wavefunctions $u(s)$. We do this by considering (3.10) as a Sturm Liouville problem defined by equations (3.15) to (3.17), as this will allow us to use a convenient MATLAB package to do our numerics.

We can also generate a plot for the determinant of the metric g. Using the knowledge we have that many of the components of our 7×7 matrix are

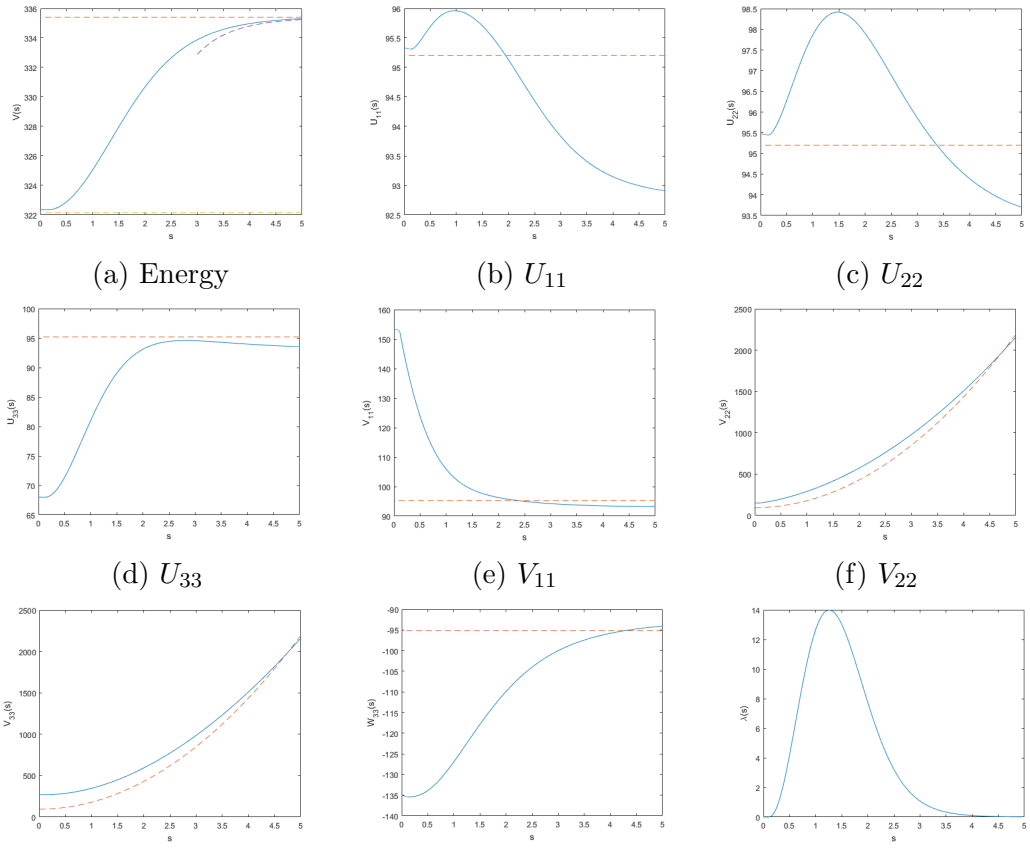

(a) Energy (b) U_{11} (c) U_{22}

(d) U_{33} (e) V_{11} (f) V_{22}

(g) V_{33} (h) W_{33} (i) λ

Figure 3.2: Plots for the various functions that were numerically calculated for $B = 2$ using gradient flow.

zero, we can calculate that the determinant is given by

$$|g| = \lambda U_{11} U_{22} V_{11} V_{22} (U_{33} V_{33} - W_{33}^2), \tag{3.26}$$

and a plot for this determinant is given in Figure 3.3, where we also give plots for the rotational energies for the spin-0 and spin-1 states as expressed in equations (3.18) and (3.19). We see that these rotational energy corrections are relatively small in comparison to the overall energy, but not so small as to be negligible. We also see that the rotational term for the isospin-1 state is slightly larger, which is responsible for this state having a higher energy. This is expected as we know that the ground state for $B = 2$ should be the deuteron.

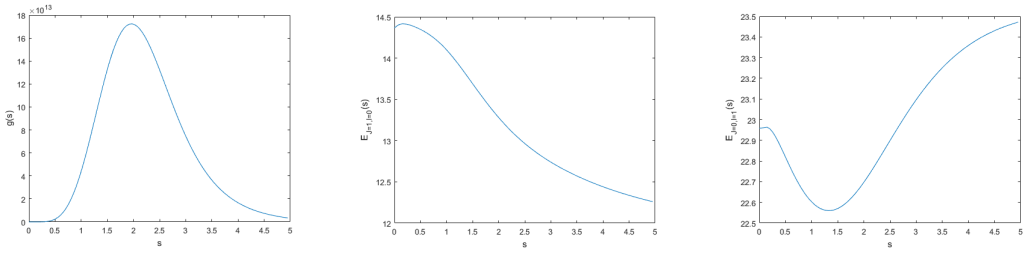

(a) $|g|$ (b) $E_J(s)(J = 1, I = 0)$ (c) $E_J(s)(J = 0, I = 1)$

Figure 3.3: Plots for the metric and rotational energy functions, that were calculated from the numerically generated functions from Figure 3.2.

Lastly, in Figure 3.4, we display plots for the Sturm-Liouville functions p, q and w, where we display two plots for q corresponding to the two different possible E_J terms.

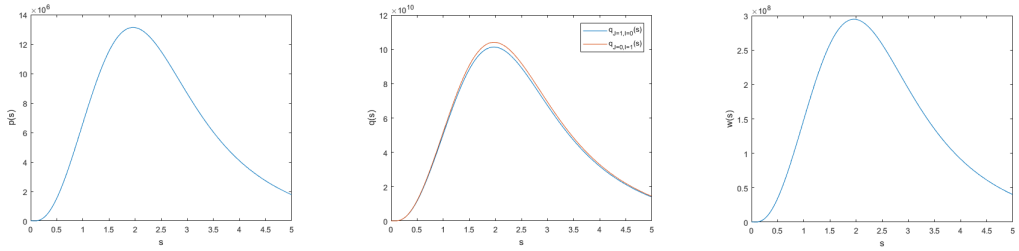

(a) p (b) q (c) w

Figure 3.4: Plots for the Sturm-Liouville functions p, q and w. Notice that we plot two functions for q, corresponding to the two different rotational energy terms.

3.4.2 Wavefunctions

We now want to calculate vibrational wavefunctions for the deuteron and the isospin-1 state. This is done numerically by solving the Sturm-Liouville problem defined by equations (3.15) to (3.17). We display the two vibrational wavefunctions in Figure 3.5. The numerical energies for the two states are 2.9221 and 2.9286 for the deuteron and isospin-1 state respectively. These values are physically somewhat meaningless before calibration, but we do see that the isospin-1 state has a slightly higher energy than the deuteron, as we would expect.

3.4.3 Comparison with experiment

We want to calibrate these energies against experiment. Note that in nature, the deuteron is the only bound state of two nucleons, but there is also an isospin-1 state which is only marginally unbound. The paper [16] gives the experimental binding energy of the deuteron as -2.225 MeV, and we

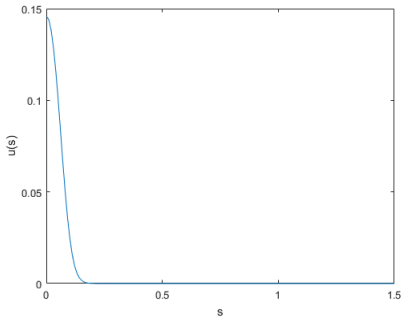

(a) $u_{J=1,I=0}(s)$

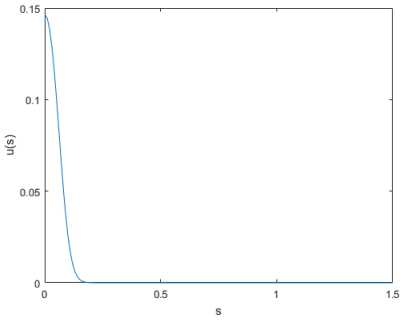

(b) $u_{J=0,I=1}(s)$

Figure 3.5: Plots for the wavefunctions for the deuteron and isospin-1 states.

must think about how to interpret our numerical energies in the context of a binding energy. The energy of two well separated nucleons in the attractive channel with total spin and isospin quantum numbers $J = 1$ and $I = 0$ is given by $2M + \hbar^2/4\Lambda$ [44], where M and Λ are the mass and moment of inertia of a single Skyrmion. For us, the values of the parameters are $M = 167.7$, $\Lambda = 47.6$ [8] and $\hbar = 46.8$. These differ from those seen in [44] as we are considering the case of massive pions with $m = 1$, rather than the massless case. This leads to an energy for two well separated Skyrmions of 346.90 in Skyrme units. Recalling from equation (3.24) that to convert to a physical energy in MeV we must multiply by a factor of 5.58, this gives us a physical energy of 1935.7 MeV. We must next also convert the energy of our deuteron bound state into MeV. Let us take the numerical energy for the deuteron, which was $2.9221 \times 12\pi^2 = 346.08$. The binding energy of the deuteron in Skyrme units is then $346.08 - 346.90 = -0.82$. Converting this into physical

units we get a binding energy of

$$E_{\text{deuteron}} = -0.82 \times 5.58 = -4.58 \text{ MeV}. \tag{3.27}$$

Using the same mechanism for the isospin-1 state, we calculate a binding energy of

$$E_{I=1} = ((2.9286 \times 12\pi^2) - 346.90) \times 5.58 = -0.28 \text{ MeV}. \tag{3.28}$$

As expected, the model admits no other bound states. The deuteron binding energy of -4.58 MeV compares relatively favourably with the experimental value of -2.225 MeV, compared to the -6.18 MeV found in [44], although it is still too large. We conjecture that this improvement may in part be due to the inclusion of a pion mass, and it would be interesting to investigate in the future whether the value can be further improved for larger pion masses than the $m = 1$ we have used here. It is also the case that unlike [44] we work in the full Skyrme model rather than the instanton approximation, so this may also be relevant in our improved results. We find that the isospin-1 state is also a bound state in our model, although only just. It is much less tightly bound than the equivalent isospin-1 state found in [44], but physically this state should be marginally unbound. Again it would be interesting to see if this state becomes unbound as the pion mass is increased further.

3.5 Remarks on the relative contributions of the vibrational mode and the pion mass term

One important remark to be made on the work presented in this chapter is that we have made two fundamental changes to the work done in [44]. Specifically, we have worked in the full Skyrme model with a vibrational mode rather than including a vibrational mode in the instanton approximation to the Skyrme model, and we have also included a non-zero pion mass. We have seen that the inclusion of these two refinements gives an improved value for the binding energy, but it is not clear which of these factors makes the most significant contribution to the improvement. Indeed, it could be the case that only one of these refinements makes any appreciable difference, or even that one of the changes has a negative effect which is more than offset by the positive effect of the other change.

In order to investigate this there are two ideas that we could consider. Firstly, we could rerun our simulation with a pion mass of zero, which would give us the results in the full Skyrme model with a vibrational mode, to compare directly with the results for the instanton approximation from [44]. Alternatively, we could investigate the results that we obtain if we neglect the vibrational mode contribution but retain the non-zero pion mass. This latter case is easier to investigate as we do not have to rerun the simulation but

instead remove the vibrational contribution by setting the function $\lambda = 1$, and then solve the modified Schrödinger equation. It is also more physically interesting as the ultimate purpose of this work was to consider a non-zero pion mass case, so we wish to retain that feature. We now give a brief discussion of this latter idea.

The equation (3.13) will take the same form as for the vibrational case, but with the difference that s and β are defined differently. Let us consider why this is so. In converting the Schrodinger equation from the form (3.10) to the form (3.13), we effectively scale λ out of the equation through the definition of the distance d in (3.11). We can now define $\lambda = 1$ in (3.11), which reduces the equation to the rather trivial form

$$d(\tau) = \int^{\tau} d\tau'. \tag{3.29}$$

This means that our distance d is now the same as our numerical time τ. In our previous calculations our simulation had 1951 time steps, so we now have that d takes integer values from 1 to 1951 with $d_{max} = 1951$. Our geodesic distance s (3.12) takes the same form, with $s_{\max} = 5$ as before, but now we have $\beta = s_{\max}/d_{\max} = 5/1951 = 0.002563$, compared to the value of $\beta = 0.009019$ we had previously.

We then solve the Schrödinger equation (3.13) again, with this new value for β and a distance measure s that has been redefined through the change in the definition of d. The process is much the same as before, and we do not

show plots here as they are qualitatively very similar to the pictures produced for the vibrational case. What we are interested in here are the values of the calibrated energies of the two states. It turns out that the numerical values we now obtain are 2.9207 and 2.9251 for the deuteron and the isospin-1 state respectively. Using the same calibration idea as previously, these translate to physical binding energies of -5.50 MeV for the deuteron and -2.59 MeV for the isospin-1 state.

There are several remarks to be made about these values. Firstly we notice that the deuteron binding energy here of -5.50 MeV is still an improvement on the -6.18 MeV found in [44], although less so than for the vibrational case. This suggests that working in the full Skyrme model with a pion mass, rather than the instanton approximation with massless pions, is worthwhile, even without the inclusion of a vibrational mode. We also see that the result when we include a vibrational mode (-4.58 MeV) gives further improvement, and gets us closer to the experimental value of -2.225 MeV, which provides some justification for the method. From this we can reasonably conjecture that both the inclusion of a vibrational mode in the full Skyrme model and the inclusion of a pion mass are both making positive contributions toward moving the binding energy closer to the experimental value. This suggests that increasing the pion mass to higher values may yield further improvement, and this should be investigated in the future. With regard to the isospin-1 state, for this case we find that the state is still bound, and more tightly so than before. Furthermore, the gap between the two

states is now smaller at 2.91 MeV, compared to the gap of 4.30 MeV when the vibrational mode was included. Since we ideally want the isospin-1 state to be unbound, it seems that the inclusion of a vibrational mode is again justified as it gets us closer to achieving this.

3.6 Discussion and outlook

The improvement to the deuteron binding energy is clearly a promising result, as is the fact that the isospin-1 state moves closer to becoming unbound. There are other observable quantities that we might like to calculate in the future to further investigate the accuracy of our model. Some obvious examples are the root mean square (rms) electric charge radius of the deuteron, its electric quadrupole moment and its magnetic dipole moment. Expressions for all of these observables are written down in [44], but for completeness we will give them here in our notation. We first define the rms electric charge radius of an attractive channel field, which is given by

$$r^2_{\text{rms}}(s) = \frac{1}{2}\int |\boldsymbol{x}|^2 B^0(s,\boldsymbol{x}) d^3x, \tag{3.30}$$

where $B^0(s,\boldsymbol{x})$ is the zeroth component of the conserved baryon number current defined by

$$B^\mu = \frac{\epsilon^{\mu\nu\alpha\beta}}{24\pi^2}\,\text{Tr}(R_\nu R_\alpha R_\beta). \tag{3.31}$$

Here $\epsilon^{\mu\nu\alpha\beta}$ is the four-dimensional Levi-Civita symbol and R_μ are the same fields we defined in equation (1.3). The electric charge radius of the deuteron is then defined as

$$r_c^2 = \int_0^\infty r_{\text{rms}}^2 u_d^2 \sqrt{|g|} ds, \tag{3.32}$$

where u_d denotes the deuteron vibrational wavefunction. We can do something similar for the quadrupole tensor. For a general attractive channel field we have

$$Q_{ij} = \frac{1}{2} \int \left(3x_i x_j - |\boldsymbol{x}|^2 \delta_{ij}\right) B^0(s, \boldsymbol{x}) d^3x, \tag{3.33}$$

where δ_{ij} is the usual Kronecker delta symbol. From symmetries of the attractive channel, one can deduce for our case that Q is diagonal and traceless. It thus contains only two independent components, say Q_{11} and Q_{22}, which are equal at $s = 0$ [44]. The overall quadrupole tensor can then be expressed as

$$Q = \frac{1}{5} \int_0^\infty \left(Q_{11} + Q_{22}\right) u_d^2 \sqrt{|g|} ds. \tag{3.34}$$

Finally, we consider the magnetic dipole moment, which is generally defined as

$$\mu_i(s) = \frac{1}{4} \int \epsilon_{ijk} x_j B_k(s, \boldsymbol{x}) d^3x, \tag{3.35}$$

where ϵ_{ijk} is now the three-dimensional Levi-Civita symbol, and B_k are the spatial components of the baryon number current. In the standard orienta-

tion it can be expressed in terms of the quantities

$$M_{ia} = \frac{1}{32\pi^2} \int x_j \, \mathrm{Tr} \left([R_i, R_j][-\frac{i}{2}\tau_a, U]U^\dagger \right) d^3x \tag{3.36}$$

and

$$m_{ik} = -\frac{1}{32\pi^2} \int \epsilon_{kmn} x_j x_m \, \mathrm{Tr} \left([R_i, R_j] R_n \right) d^3x, \tag{3.37}$$

where U is the Skyrme field defined in Chapter 1 and τ_a is one of the Pauli matrices. Again, the symmetries of our case mean that in fact all of the M_{ia} are zero and the only non-zero components we need in order to write down an expression for the magnetic dipole moment of the deuteron are m_{11} and m_{22}. These can be expressed explicitly as

$$m_{11} = \frac{1}{4} \int \left(x_2^2 + x_3^2 \right) B^0(s, \boldsymbol{x}) d^3x \tag{3.38}$$

and

$$m_{22} = \frac{1}{4} \int \left(x_1^2 + x_3^2 \right) B^0(s, \boldsymbol{x}) d^3x. \tag{3.39}$$

Then we can write down an expression for the magnetic dipole moment as

$$\mu = \frac{\hbar}{2} \int_0^\infty \left(\frac{m_{11}}{V_{11}} + \frac{m_{22}}{V_{22}} \right) u_d^2 \sqrt{|g|} ds. \tag{3.40}$$

As we did not calculate the baryon number current (3.31) during our simulation, we do not calculate these quantities here, but it is a realistic aspiration that this could be done in the near future. Experimental values

for these quantities are $r_c = 2.095$ fm, $Q = 0.2859$ fm^2 and $\mu = 0.8574$ nm [16], so once these quantities are calculated within our model we can compare them to these values.

In summary, there is good evidence that this vibrational approach has had a positive effect, raising the binding energy of both the deuteron and isospin-1 state to be closer to their experimental values. An analysis of what happens when the pion mass is varied is likely to be worthwhile, and we might like to consider the cases $m = 0.5$, $m = 1.5$ and $m = 2$ in addition to the cases $m = 0$ and $m = 1$ already seen. In particular we conjectured in the previous section that increasing the pion mass further beyond $m = 1$ may take us closer to the experimental binding energy. In [6], the authors argue that the choice of m should be made such that the calculated mean charge radius of the Skyrmion agrees with the experimental value of the zero isospin nucleus for that value of B. They calculate the appropriate value of m for several values of B, in particular for $B = 4, 6, 8, 10$ and 12, and find that m should always take a value between 0.6 and 1.2. As such, although they do not calculate a value for $B = 2$, it would seem sensible to look at values of m around this range, or indeed to calculate the appropriate value. Finally, a calculation of other physical observables will allow us to further test the validity of the model against experiment.

Chapter 4

Vibrational quantisation of the Oxygen-16 nucleus

This work is based upon the paper [30] by Chris Halcrow, Chris King and Nick Manton, and aims to reproduce and generalise some of the results it presents. The idea is to treat the Oxygen-16 nucleus (which we model as a $B = 16$ Skyrmion) as a cluster of four alpha particles, which we can interpret as four $B = 4$ Skyrmions that evolve according to the Skyrme model. In particular if we collide two pairs of alpha particles we find that there is a dynamical mode that passes through a tetrahedral configuration, then transitions into a square configuration and a dual tetrahedron, before breaking back into two pairs of alpha particles again as shown in Figure 4.1. This scattering mode will now be used to construct a vibrational manifold and we can then quantise the system in line with the vibrational approach seen in [29]. We

Figure 4.1: The scattering mode for four alpha particles in the Skyrme model, taken from [30] and using the colouring convention found in [19].

identify the degrees of freedom in our manifold as the positions of the alpha particles, which lie on a surface, and note that each configuration has D_2 symmetry. There are three scattering modes to consider which correspond to lines passing through the three pairs of opposing faces of the tetrahedron. As such we must choose as our manifold a surface which asymptotically stretches out to infinity in six directions. The choice made in [30] is the 6-punctured sphere with constant negative curvature.

The D_2 symmetry that we noted previously means that we can study one quarter of the space, and the other three regions will be related by symmetry. We call this quarter surface M. We then map M onto a region of the complex upper half plane which we call F where $F = \mathbb{H}/\Gamma(2)$, where $\mathbb{H}$ is the entirety of the complex upper half plane and $\Gamma(2)$ is a modular subgroup. We show the relevant surfaces in Figure 4.2 where we note that regions of the same colouring are related by D_2 symmetry and the solid black lines represent the scattering mode from Figure 4.1. Tetrahedral configurations are at points where three colours meet and square configurations are at points where four colours meet.

We are now in a position to formulate the problem. Starting from the

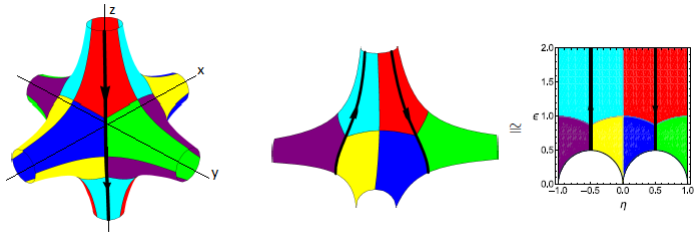

Figure 4.2: From left to right: the 6-punctured sphere, the surface M and the region F [30].

standard Schrödinger equation

$$\left(-\frac{\hbar^2}{2}\Delta + V(\mathbf{x})\right)\psi = E\psi, \tag{4.1}$$

we can split the total wavefunction $|\Psi\rangle$ into a vibrational part ϕ and a component $|\Theta\rangle$ corresponding to the rigid body angular momentum states. The angular part of the problem can be solved easily with solutions related to spherical harmonics. We will be considering the vibrational problem for ϕ which reduces to

$$-\Delta_{\text{vib}}\phi + V(\mathbf{x})\phi = (E - E_J)\phi, \tag{4.2}$$

where E is the total energy of $|\Psi\rangle$ and E_J is its rotational energy, which we have to subtract from the total energy to give the vibrational energy. We approximate E_J to be constant for each J. The E_J term provides a coupling between the vibrational and spin equations, as it depends on the spin J of the angular state and the moments of inertia of the Skyrme configurations. We will neglect E_J for the time being and introduce it again at a later stage.

We wish to solve (4.2) on our region F, and to do so we define a complex coordinate $z = \eta + i\epsilon$ on $\mathbb{H}$. Our choice of metric on F is the hyperbolic metric

$$ds^2 = \frac{d\eta^2 + d\epsilon^2}{\epsilon^2}, \tag{4.3}$$

which we use as an approximation to the Skyrme metric. The uniformisation theorem allows us to equip any hyperbolic surface with a constant negative curvature metric, so this choice is allowed and mathematically natural. However, it must be noted that the metric should ideally be the induced metric from Skyrmion-Skyrmion scattering which might be very different. It is also likely to be much more complicated to work with, so we use the simplifying assumption of the hyperbolic metric here. Using this metric it can then be shown [30] that the kinetic operator in (4.2) reduces to

$$-\Delta_{\text{vib}} = -\epsilon^2 \left(\frac{\partial^2}{\partial \eta^2} + \frac{\partial^2}{\partial \epsilon^2} \right). \tag{4.4}$$

Here the prefactor of ϵ^2 is a consequence of the choice of metric. We now have an explicit form for our Schrödinger equation (4.2), up to a choice for the potential which we shall make later.

4.1 The rigid body case for Oxygen-16

Before we begin an analysis of the vibrational quantisation method for $B = 16$, it might be useful to recap what is known for the rigid body case. It

is well understood that all known Skyrmion configurations for $B = 16$ can be thought of as being composed of four $B = 4$ cubes. The three most notable configurations are the tetrahedron, the square and the bent square, and these are displayed in Figure 4.3.They exhibit respectively T_d, D_4 and D_2 symmetries, and it is these symmetries which lead to constraints on the permitted spin states allowed by rigid body quantisation.

The tetrahedral (T_d) symmetry leads to the constraints

$$\exp\left(\frac{2i\pi}{3\sqrt{3}}(\hat{L}_1+\hat{L}_2+\hat{L}_3)\right)\exp\left(\frac{2i\pi}{3\sqrt{3}}(\hat{K}_1+\hat{K}_2+\hat{K}_3)\right)\Psi=\Psi \tag{4.5}$$

$$\exp\left(i\pi\hat{L}_3\right)\Psi=\Psi, \tag{4.6}$$

for some wavefunction Ψ.

Similarly, the square (D_4) symmetry leads to the constraints

$$\exp\left(\frac{i\pi}{2}\hat{L}_3\right)\exp\left(i\pi\hat{K}_1\right)\Psi=\Psi \tag{4.7}$$

$$\exp\left(i\pi\hat{L}_1\right)\Psi=\Psi, \tag{4.8}$$

and the bent square (D_2) symmetry leads to

$$\exp\left(i\pi\hat{L}_3\right)\Psi=\Psi \tag{4.9}$$

$$\exp\left(i\pi\hat{L}_1\right)\Psi=\Psi. \tag{4.10}$$

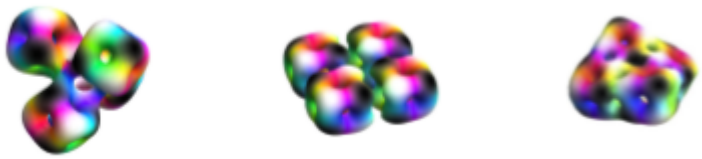

Figure 4.3: Three important configurations of the $B = 16$ Skyrmion: from left to right we have the tetrahedron, the square and the bent square [28].

If we apply these constraints in the rigid body scheme we obtain the allowed spin states, and these are given in Table 4.1. Note that we only consider isospin zero states here.

J	Tetrahedron	Square	Bent Square
0	$\|0,0\rangle$	$\|0,0\rangle$	$\|0,0\rangle$
2		$\|2,0\rangle$	$\|2,0\rangle$ $\|2,2\rangle+\|2,-2\rangle$
3	$\|3,2\rangle - \|3,-2\rangle$		$\|3,2\rangle - \|3,-2\rangle$
4	$\|4,4\rangle + \frac{\sqrt{14}}{5}\|4,0\rangle + \|4,-4\rangle$	$\|4,0\rangle$ $\|4,4\rangle + \|4,-4\rangle$	$\|4,0\rangle$ $\|4,2\rangle + \|4,-2\rangle$ $\|4,4\rangle + \|4,-4\rangle$
5		$\|5,4\rangle - \|5,-4\rangle$	$\|5,2\rangle - \|5,-2\rangle$ $\|5,4\rangle - \|5,-4\rangle$
6	$\|6,4\rangle - \frac{\sqrt{2}}{7}\|6,0\rangle + \|6,-4\rangle$ $\frac{\sqrt{5}}{11}\|6,6\rangle - \|6,2\rangle - \|6,-2\rangle + \frac{\sqrt{5}}{11}\|6,-6\rangle$	$\|6,0\rangle$ $\|6,4\rangle + \|6,-4\rangle$	$\|6,0\rangle$ $\|6,2\rangle + \|6,-2\rangle$ $\|6,4\rangle + \|6,-4\rangle$ $\|6,6\rangle + \|6,-6\rangle$

Table 4.1: A table listing the allowed rigid body spin states with zero isospin for the three main $B = 16$ configurations.

Some comments to make here are that we expect vibrational quantisation to improve upon the rigid body picture, but clearly any new method should still reproduce the well understood results from rigid body analysis.

We observe that for the tetrahedron there is no allowed spin-2 state, and for the square there is no allowed spin-3 state. As such, the wavefunctions describing such states cannot be found from rigid body quantisation, and one must instead consider a configuration space that contains both the tetrahedron and the square, which we go on to do shortly. It will also turn out in the vibrational picture that there are some vibrational wavefunctions (for example for spin-2) which vanish at the tetrahedron, even when they are not explicitly forbidden from being there. This does not occur in rigid body quantisation. These are limitations of the rigid body approach, and demonstrate how the rigid body scheme cannot fully capture all of the low lying states for Oxygen-16.

4.2 Important properties of the region F

The region F has many interesting properties. Firstly observe that the full six-punctured sphere has cubic symmetry O, and so the quarter of the sphere M and its corresponding projection onto the complex plane F have $O/D_2 \cong S_3$ symmetry. This S_3 symmetry will be very important later on, when we consider the different representations into which our solutions can fall. In particular, the group S_3 has three different representations which we shall call the trivial, sign and standard representations, and we discuss these later.

We would like to understand more about the region F on which we will solve our problem. We begin by noting that the region coincides with the

fundamental domain of the modular subgroup $\Gamma(2)$ [18]. This group is defined as

$$\Gamma(2) = \left\{ \begin{bmatrix} a & b \\ c & d \end{bmatrix} \in \mathrm{PSL}(2,\mathbb{Z}); a \equiv d \equiv 1 (\mathrm{mod}\ 2), b \equiv c \equiv 0 (\mathrm{mod}\ 2) \right\}. \tag{4.11}$$

This group is freely generated by two matrices, which we denote by $A = \begin{bmatrix} 0 & -1 \\ 1 & 0 \end{bmatrix}$ and $B = \begin{bmatrix} 1 & 1 \\ 0 & 1 \end{bmatrix}$. We also admit the inverses of these matrices, and combinations of them. It then turns out that these matrices can be used to map between different coloured regions in F. If we take the red region to be the base region, with points in the red region defined by their complex coordinate z, then such a point is related to points in the other coloured regions by the mappings shown in Figure 4.4.

To acquire more of an understanding of how these matrices act, it is helpful to realise that they can also be thought of as Möbius transformations. If we consider a point z in the red region and think of it as the fraction $z/1$, we then represent this as a 2-component column vector with the first entry as the numerator and second entry as the denominator. We then act on this vector with our matrices. For example, if we consider the matrix B we find that

$$B(z) = \begin{bmatrix} 1 & 1 \\ 0 & 1 \end{bmatrix} \begin{bmatrix} z \\ 1 \end{bmatrix} = \begin{bmatrix} z+1 \\ 1 \end{bmatrix}, \tag{4.12}$$

and it is now obvious that the matrix B takes a point z to the point $z+1$.

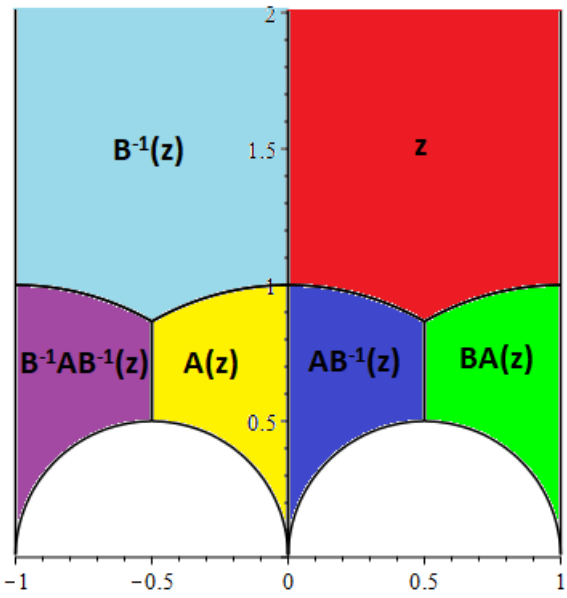

Figure 4.4: A figure showing the relationship between the different coloured regions of F using the matrices A and B.

That is to say that B clearly acts as a simple translation by one unit in the positive real direction. The inverse matrix B^{-1}, then acts as the opposite translation of one unit in the negative real direction. The matrix A is slightly more complicated but we can do the same calculation to find that

$$A(z) = \begin{bmatrix} 0 & -1 \\ 1 & 0 \end{bmatrix} \begin{bmatrix} z \\ 1 \end{bmatrix} = \begin{bmatrix} -1 \\ z \end{bmatrix}, \tag{4.13}$$

and so we see that A takes a point z to the point $-1/z$, acting as an inversion. It turns out that for the inverse matrix A^{-1}, we get the same transformation as for A, namely $z \mapsto -1/z$.

We see that A and B represent fairly simple Möbius transformations, but we also recall from Figure 4.4 that some of the mappings are described by compositions of these matrices. For example the map from the red to the green region is given by the matrix $BA = \begin{bmatrix} 1 & -1 \\ 1 & 0 \end{bmatrix}$. Using the same arguments as before, this is the Möbius transformation $z \mapsto (z-1)/z$, and it is less obvious how this acts. However we can understand the properties of any Möbius transformation by recalling that it can be decomposed into four simple transformations. For the transformation

$$f(z) = \frac{az+b}{cz+d}, \tag{4.14}$$

we can write it as $f(z) = f_4 \circ f_3 \circ f_2 \circ f_1(z)$ where

$$f_1(z) = z+d/c \ , \ f_2(z) = 1/z \ , \ f_3(z) = \frac{bc-ad}{c^2}z \text{ and } f_4(z) = z+a/c. \tag{4.15}$$

This decomposition can make many properties of the transformation more obvious. It is now apparent that the transformation acts firstly as a translation by d/c, then f_2 is an inversion and reflection with respect to the real axis. The third part is a dilation and a rotation, and the fourth part is another translation, this time by a/c. For the case of the transformation characterised by BA, we have $a = 1$, $b = -1$, $c = 1$ and $d = 0$, yielding the functions $f_1(z) = z$, $f_2(z) = 1/z$, $f_3(z) = -z$ and $f_4(z) = z + 1$. We check

this decomposition works for this example

$$f_4 \circ f_3 \circ f_2 \circ f_1(z) = f_4 \circ f_3 \circ f_2(z) = f_4 \circ f_3(1/z) = f_4(-1/z) \\ = (-1/z) + 1 = \frac{z-1}{z}. \tag{4.16}$$

We can do this for any of the composite transformations to investigate how they act on F. One could in fact take this even further and relate back to the full six-punctured sphere. The projection of the full surface on to the complex upper half-plane is shown in Figure 4.5. Again, the regions are all related by combinations of the matrices A and B and their inverses, and for the exact transformations the reader is referred to [18]. Regions of the same colour are related by D_2 symmetry as mentioned previously.

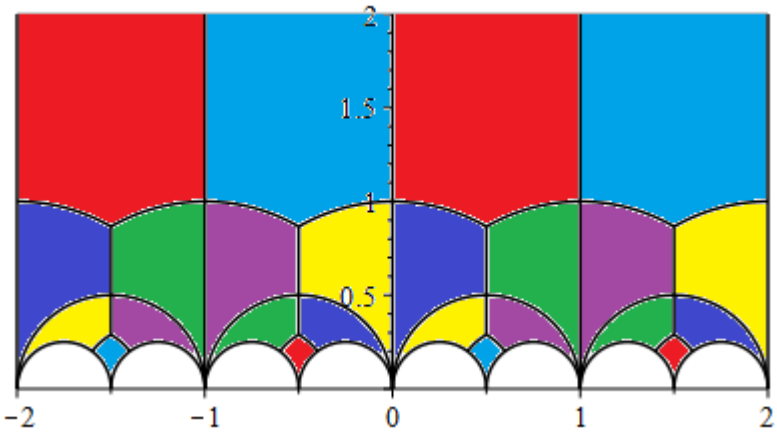

Figure 4.5: The full six-punctured sphere projected onto the complex upper half-plane.

Let us now return to the quarter of the 6-punctured sphere, and note some important points on our region F. As previously mentioned, points

where three or four coloured regions meet are significant as they represent the positions of tetrahedral and square configurations respectively. There are tetrahedral configurations at the point $1/2 + i\sqrt{3}/2$ where the red, blue and green regions meet and the point $-1/2 + i\sqrt{3}/2$ where the light blue, yellow and purple regions meet. There is clearly a square configuration at the point i where the red, blue, light blue and yellow regions meet. More subtly there are two halves of square configurations at the points $1 + i$ and $-1 + i$ which can be identified with each other, and so are effectively one point where the red, green, purple an light blue regions meet. Similarly the points $1/2 + i/2$ and $-1/2 + i/2$ can be identified with each other and are effectively one point where the blue, green, purple and yellow regions meet, so again each of these points can be thought of as hosting half of a square configuration.

It will also be useful for later reference to formulate equations for the boundaries of regions of F. Obviously the equations of the straight boundaries are trivial but we will list the equations of the curved boundaries below for the sake of convenience. The red/green boundary is characterised by the equation

$$\epsilon = \sqrt{\eta(2 - \eta)}, \tag{4.17}$$

the red/blue boundary by the equation

$$\epsilon = \sqrt{1 - \eta^2} \tag{4.18}$$

and the lower right semicircle by

$$\epsilon = \sqrt{\eta(1-\eta)}. \tag{4.19}$$

Similarly in the $\eta < 0$ region the light blue/yellow boundary is defined by

$$\epsilon = \sqrt{1-\eta^2}, \tag{4.20}$$

the light blue/purple boundary by

$$\epsilon = \sqrt{-\eta(2+\eta)} \tag{4.21}$$

and the lower left semicircle by

$$\epsilon = \sqrt{-\eta(1+\eta)}. \tag{4.22}$$

Now is a good moment to consider the way in which parity acts on M and hence F. In general the parity operator acts such that $(x, y, z) \mapsto (-x, -y, -z)$. In this case due to D_2 symmetry the action can be written as $(x, y, z) \mapsto (x, -y, z)$, which corresponds to $\eta \mapsto -\eta$ on F, or in terms of our complex coordinate or $z \mapsto -\bar{z}$. More formally we write the parity operator as

$$P\phi(z) = \phi(-\bar{z}). \tag{4.23}$$

If the wavefunction is invariant under this operator it has positive parity and

if it picks up a minus sign then it has negative parity.

One other symmetry that we will be interested in is the $\eta \mapsto 1 - \eta$ symmetry. If we look at the red region of F which runs from $\eta = 0$ to $\eta = 1$, this symmetry is a symmetry about the line $\eta = 1/2$. We can think of it as a combination of the translation symmetry described by B and parity. More precisely

$$P(B\phi(z)) = P(\phi(z-1)) = \pm\phi(1-\bar{z}) = \pm\phi(1-\eta,\epsilon)$$

where the $\pm$ sign is dependent on the parity of the vibrational wavefunction ϕ. We shall see that many of the states we discuss shall exhibit symmetry or anti-symmetry under the the $\eta \mapsto 1 - \eta$ transformation, although for states in the standard representation this will only be true for certain types of solution.

4.3 The different representations

Since we have already alluded to them before, now would be a good time to formally introduce the three different representations into which our states may fall. As discussed previously, F has a overall S_3 symmetry, and the group S_3 has three different representations which we call the trivial, sign and standard representations. S_3 actions can be broken down into two categories, namely transpositions and permutations. If we number our group elements

on which S_3 acts as 1, 2, 3 then a transposition exchanges two elements (e.g. $1 \mapsto 2$, $2 \mapsto 1$ and 3 is fixed). A permutation cycles the three elements around (e.g. $1 \mapsto 2$, $2 \mapsto 3$ and $3 \mapsto 1$).

We say a vibrational wavefunction is in the trivial representation if it is invariant under either of these actions. On the other hand a sign representation vibrational wavefunction is still invariant under permutations but picks up a minus sign under transpositions.

The standard representation is two dimensional so we need some slightly different notation. We label a full standard representation wavefunction as $|\psi\rangle = u\,|\Theta\rangle_1 + v\,|\Theta\rangle_2 + w\,|\Theta\rangle_3$ where the $|\Theta\rangle_i$ are the spin states with which the vibrational wavefunction has been combined. Here u, v and w describe the vibrational wavefunction and are the elements on which S_3 acts. It still acts as either transpositions or permutations. For example, under a (1 2) transposition the wavefunction becomes $|\psi\rangle = v\,|\Theta\rangle_1 + u\,|\Theta\rangle_2 + w\,|\Theta\rangle_3$ (i.e. elements 1 and 2 are permuted), and under a (1 2 3) permutation it becomes $|\psi\rangle = v\,|\Theta\rangle_1 + w\,|\Theta\rangle_2 + u\,|\Theta\rangle_3$ (i.e. the three elements are permuted cyclically). We must also observe that this three-dimensional basis of objects is in fact reduced to a two-dimensional one, since the vibrational wavefunction $u+v+w$ is invariant under both transpositions and permutations. This yields the constraint

$$u + v + w = 0. \tag{4.24}$$

Note that when we calculate states in the standard representation we can

calculate combinations of u, v and w. However as we shall see, only certain combinations have boundary conditions which are convenient to work with and only certain combinations exhibit symmetry or anti-symmetry under the $\eta \mapsto 1 - \eta$ transformation.

The different representations will be critical shortly when we discuss boundary conditions. We should also be aware that vibrational wavefunctions in the different representations act differently under Möbius transformations, trivial states will be invariant under all transformations whereas sign states can pick up a minus sign.

4.4 Boundary conditions on the vibrational wavefunctions

Now that we understand the symmetries of our region F, we are in a position to think about how these can be used to determine the boundary conditions on our vibrational wavefunctions as we solve (4.2). As previously argued, F has S_3 symmetry and the group S_3 has three representations called the trivial, sign and standard representations. The potential (4.28) is invariant under all elements of S_3 meaning all vibrational wavefunctions can be labelled by their representation and parity, and these properties will determine boundary conditions.

Our technique for the trivial and sign representations will be to solve (4.2) in the red region of F and then map the solution to the rest of F using

A, B and parity. As such we need to fix conditions on the boundaries of the red region. These boundaries consist of two vertical lines at $\eta = 0$ and $\eta = 1$, and two arcs of circles on the lower boundary. The condition on the vertical line at $\eta = 0$ is simple and is fixed entirely by parity. Because parity is essentially a reflection about the line $\eta = 0$ in our coordinates, states with positive parity must have vanishing derivative across the line $\eta = 0$ whereas states with negative parity must themselves vanish on that line. The condition on the line at $\eta = 1$ is also fixed by parity and will be the same as for the line at $\eta = 0$. To understand why, observe Figure 4.6. Consider a point z^+ in the red region which is arbitrarily close to the line

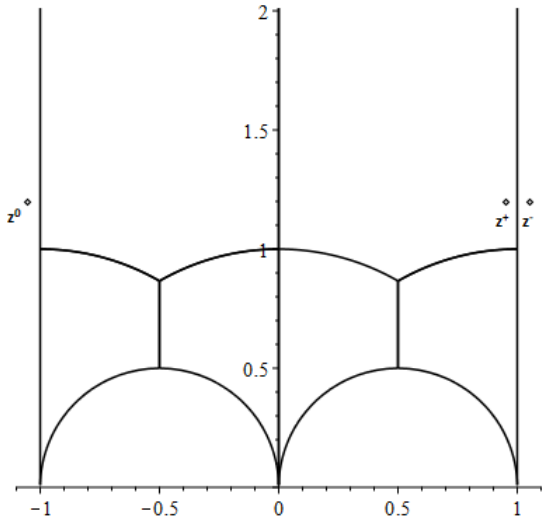

Figure 4.6: A plot showing the region F. We use the relationship between the points z^+, z^- and z^0 to determine the conditions on the boundary line $\eta = 1$.

$\eta = 1$. Then consider acting twice with the action B^{-1}, which translates

the point two units to the left so that it is now just outside (to the left of) the region F altogether. We label this point z^0. Since it can be shown that B^{-1} acts as a (1 2) transposition, trivial wavefunctions will take the same value at these two points. Sign wavefunctions pick up a minus sign under a transposition, but since we act with B^{-1} twice this cancels out, so the sign wavefunctions also take the same value at these two points. We then consider acting with the parity operator on the new point, which takes it to the point z^-, which is now again arbitrarily close to the line $\eta = 1$, but this time on the right hand side outside of the red region. If we take the limiting case where these two points approach the line $\eta = 1$ we can deduce a boundary condition. In particular the wavefunction at the two points takes the same value if the state has positive parity, meaning that the derivative of the wavefunction across the line must be zero. If the state has negative parity then the wavefunction takes opposite signed values at the two points, so in order for the wavefunction to be continuous it must vanish on the line. These are the same conditions as for the line $\eta = 0$.

To understand the boundary conditions on the curved boundary we consider Figure 4.7. We mark a boundary of interest in red, and label it C. Note that the right hand part of the curve is related by the $\eta \mapsto 1 - \eta$ symmetry so fixing the conditions on C is sufficient for the trivial and sign representations. For the standard representation we will have to think a little harder, as we explain shortly. We again consider three points z^+, z^- and z^0. The points z^+ and z^0 are now related by one action of the matrix A and

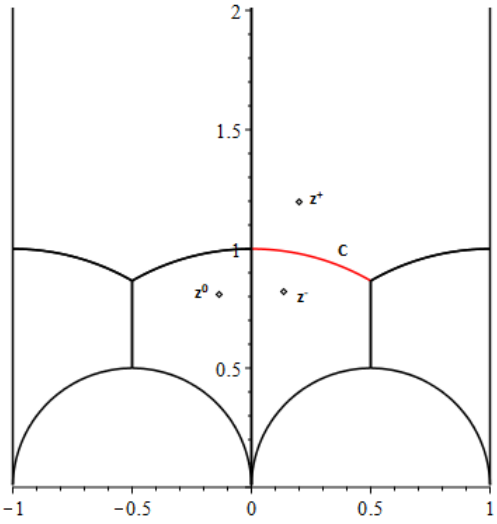

Figure 4.7: A plot showing the region F. We use the relationship between the points z^+, z^- and z^0 to determine the conditions on the boundary curve C.

then z^0 and z^- are related by parity. Again it can be shown that A acts as a transposition, this time a (1 3) transposition. As a result, in the trivial representation the wavefunction does not change in mapping from z^+ to z^0, whereas in the sign representation the wavefunction will change sign. The wavefunction then picks up a sign in mapping from z^0 to z^- corresponding to the parity of the state. In fact, we discover that the value of the wavefunction at the points z^+ and z^- are the same for positive parity trivial representation states and negative parity sign representation states. Conversely they are of equal magnitude but opposite sign for negative parity trivial representation states and positive parity sign representation states. Because we require our wavefunctions to be continuous and have continuous derivative across C we

can conclude that for positive parity trivial states and negative parity sign states the derivative must be zero across C whilst for negative parity trivial states and positive parity sign states we find that the value of the function must be zero. This can be summarised for the trivial representation as

$$\begin{aligned} \phi(z) = 0 \text{ for negative parity and} \\ \partial_{\perp}\phi(z) = 0 \text{ for positive parity,} \end{aligned} \tag{4.25}$$

and for the sign representation as

$$\begin{aligned} \phi(z) = 0 \text{ for positive parity and} \\ \partial_{\perp}\phi(z) = 0 \text{ for negative parity.} \end{aligned} \tag{4.26}$$

The condition on the right hand curved boundary will be related by the $\eta \mapsto 1 - \eta$ symmetry to the condition on C. Recalling that the symmetry is a combination of the translation symmetry described by B (a transposition) and parity, we can deduce that positive parity trivial states and negative parity sign states exhibit symmetry under this action, and conversely negative parity trivial states and positive parity sign states exhibit anti-symmetry under this action. As such, positive parity trivial states and negative parity sign states will have the same zero derivative condition on the right hand curve as they had on C, whereas negative parity trivial states and positive parity sign states should take the opposite value on the right hand curve. However, since the condition for these states is that the wavefunction vanishes on these

lines, this condition is in fact also replicated.

In summary we find that in the trivial representation the boundary conditions are that for positive parity states the wavefunction has zero derivative on all four boundaries of the red region and for negative parity states the wavefunction vanishes on all four boundaries of the red region. For the sign representation states with positive parity have the condition that the wavefunction has zero derivative on the vertical lines and vanishes on the curved lines, whilst for negative parity states the wavefunction vanishes on the vertical lines and has zero derivative on the curved lines.

For the standard representation things are more complicated. The conditions on the vertical lines work in the same way. The condition on $\eta = 0$ is fixed simply by parity and the condition on $\eta = 1$ is fixed using the same argument as before. Here we must take care to check that when acting twice with B^{-1} our wavefunction is still invariant. Recalling that B^{-1} acts as a (1 2) transposition, this means that after one action we take $u \mapsto v$ and $v \mapsto u$, but then after a second application this is undone, so the argument applies as before.

However, for the curved lines we must be careful. We fixed the boundary condition previously by considering a single action of A and parity to relate points on either side of the curve C. For the standard representation though, we will only be able to use this argument for certain combinations of u, v and w, namely those which are invariant up to a change of sign under an action of A. Since A acts as a (1 3) transposition, the combinations in question will

be $u + w$, which will be invariant under A, and $u - w$, which will change by a minus sign under A. We could consider more complicated functions of u and w but these are the simplest and most convenient to work with. However this argument leads to a further difficulty. We previously derived the boundary condition on the right hand curve by using the condition on the C plus the $\eta \mapsto 1 - \eta$ symmetry. However the $\eta \mapsto 1 - \eta$ symmetry does not apply to the combinations $u + w$ and $u - w$. This is because the symmetry involves an action of B^{-1} which is a (1 2) transposition and so transforms $u + w$ and $u - w$ into combinations involving v which cannot be related to their original forms by a simple sign. In short, there is no reason to expect that $u + w$ and $u - w$ should exhibit any kind of symmetry under $\eta \mapsto 1 - \eta$. In fact, examples of standard representation states that would exhibit such a symmetry are $u+v$ (symmetric) and $u-v$ (anti-symmetric), but these do not allow us to derive a boundary condition on C in the first place for the reason argued previously. To summarise, there is no combination of u, v and w for which we can derive a boundary condition on both of the curved boundaries simultaneously. Therefore for the standard representation we will do things slightly differently by considering a slightly different region. We take the continuation of the curve C down to its intersection with the line $\eta = 1$. This gives us a region that now contains the red region of F and part of the green region. In turn this means that when we solve the Schrödinger equation on this region we will have to define the potential in a piecewise way, as it takes a different form in the two coloured regions. This is not too difficult

however, as the equations of the potential in the coloured regions are related by the relevant Möbius transformation. Our redefined boundaries now divide F into four rather than six regions, no longer entirely based on colouring, and we can now make a similar type of argument to before. In Figure 4.8 we again consider two points z^+ and z^- arbitrarily close to C, related by a Möbius transformation plus parity via a point z^0. If the wavefunctions we

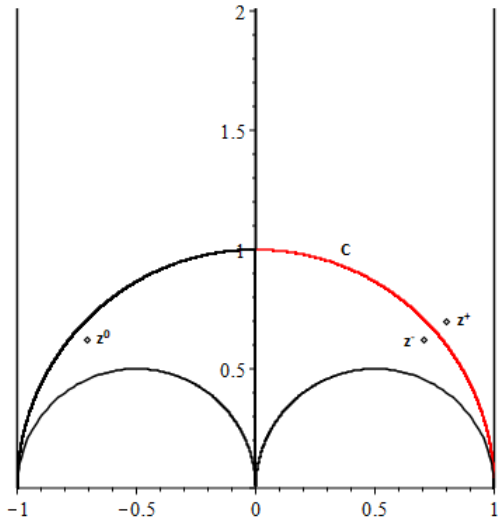

Figure 4.8: A plot showing the region F. We use the relationship between the points z^+, z^- and z^0 to determine the conditions on the extended boundary curve C for standard representation states.

consider are of either the form $u + w$ or $u - w$, then we can say that the Matrix A, a (1 3) transposition which relates the points z^+ and z^-, leaves the wavefunction $u+w$ invariant and flips the sign of the wavefunction $u-w$. If we then combine with parity, it emerges that $u + w$ wavefunctions with positive parity take the same value at z^+ and z^-, whereas those with negative

parity are related by a minus sign. On the other hand, $u - w$ wavefunctions with negative parity take the same value at z^+ and z^- but ones with positive parity are related by a minus sign. This leads to the boundary conditions

$$\begin{aligned} u - w = 0,\ \partial_\perp(u + w) = 0 \text{ for positive parity and} \\ u + w = 0,\ \partial_\perp(u - w) = 0 \text{ for negative parity,} \end{aligned} \tag{4.27}$$

where $\partial_\perp$ denotes a derivative normal to the curved boundary.

4.5 The potential

We must now make a choice for our potential function. There are many possibilities for this, but the choice made in [30] is

$$V(\eta, \epsilon) = \epsilon^2 \left(\omega^2 \left(\eta - \frac{1}{2} \right)^2 + \mu^2 \right), \tag{4.28}$$

where ω and μ are constant parameters. This choice is motivated by two ideas. Firstly, this potential is minimal at the tetrahedron, and this is desirable due to the physical observation that the minimal energy Oxygen-16 state has a tetrahedral shape. Secondly, the overall prefactor of ϵ^2 in (4.28) ensures that (4.2) is a separable equation, by cancelling with the prefactor in the metric. We note that at the tetrahedron, given by $(\eta, \epsilon) = (1/2, \sqrt{3}/2)$, the potential takes the value 96, and at the squares, given by $(\eta, \epsilon) = (0, 1), (1, 1)$ and $(1/2, 1/2)$, it takes the value 128.75. We plot the potential in Figure 4.9,

with the tetrahedron and squares clearly marked and using the parameter choice for ω and μ made in [30].

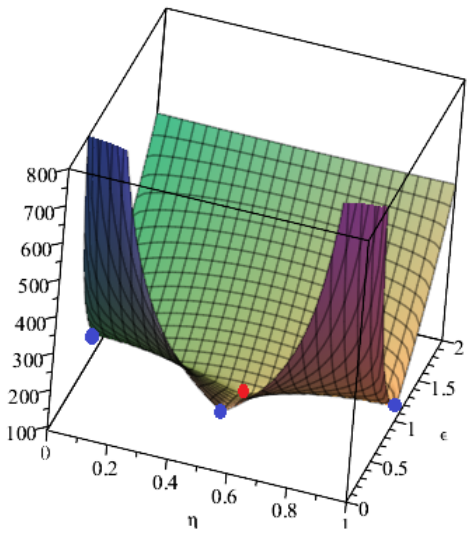

Figure 4.9: A 3D plot of the potential (4.28) for $\eta > 0$, with $\omega = \sqrt{3}$ and $\mu = 8\sqrt{2}$. The red circle shows the position of the tetrahedral configuration and the blue circles show the squares.

It is important to note that this expression for the potential applies only in the top right (red) region of F. To obtain the potential for the other regions we can define V to take the same value at points related by symmetry. We see that the potential is continuous but not smooth across the boundaries of the coloured regions, and this is in fact the best that we are able to do.

One comment to make is that our region F extends to ∞ in the ϵ-direction and this potential approaches ∞ as $\varepsilon \to \infty$. This is not physically realistic and also is not consistent with the standard Skyrmion potential which attains a finite value at ∞.

The use of a potential that yields a separable Schrödinger equation allows Halcrow, King and Manton to use one-dimensional numerics to obtain solutions to (4.2) in [30]. Our ambition is to use two-dimensional numerics to solve (4.2), which allows us to make a more general choice of potential. However let us first consider the potential (4.28) and other possible separable potentials.

As stated previously, the Schrödinger equation for potential (4.28) is separable, and solutions take the form

$$\phi(\eta, \epsilon) = \sum_n a_n H_n(\eta) G_n(\epsilon), \tag{4.29}$$

where H_n and G_n actually have an analytic form (H are hypergeometric functions and G are modified Bessel functions). However we solve the problem numerically as the method is then able to be generalised to other separable potentials that may not share this analytic property. The coefficients a_n are determined by matching boundary conditions and symmetries on F.

4.6 Constructing solutions

In the interest of completeness, we will now briefly discuss the case of using separable potentials and one-dimensional numerics, before turning our attention to the more complicated non-separable case later in this chapter.

We will now solve (4.2) with potential (4.28) by separation of variables.

This leads to the following ordinary differential equations for $G(\epsilon)$ and $H(\eta)$. It is important to point out that we do not introduce a factor of $\sqrt{\epsilon}$ to (4.29) as is seen in [30], as our method of obtaining solutions does not depend on G being an analytic function (in this case a Bessel function). As such our ODEs are

$$\frac{G''(\epsilon)}{G(\epsilon)} + \frac{E}{\epsilon^2} - k = 0, \tag{4.30}$$

and

$$\frac{H''(\eta)}{H(\eta)} = \left(\eta - \frac{1}{2}\right)^2 \omega^2 + \mu^2 - k, \tag{4.31}$$

where k is the constant associated with separation of variables, and we observe that E does not appear in the second equation. As such the only free parameter in the ODE for H is k, and we can treat this equation as an eigenvalue problem to find values of k. We can in fact solve (4.31) by treating it as a Sturm-Liouville Problem. As we saw previously in Chapter 3, this involves rewriting the equation in the form

$$-\left(p(x)\frac{dy}{dx}\right)' + q(x)y = kw(x)y, \tag{4.32}$$

where y is a function of x which we solve for. In our case the variable x is replaced by η and the function $y(x)$ replaced by $H(\eta)$, and the functions p, q and w can then be determined. It turns out that $p(\eta) = w(\eta) = 1$ and $q(\eta)$ is given by

$$q(\eta) = \omega^2 \left(\eta - \frac{1}{2}\right)^2 + \mu^2. \tag{4.33}$$

We can then solve the Sturm-Liouville problem easily, and obtain a set of eigenvalues k and corresponding eigenfunctions H_k.

We then obtain solutions of (4.30) numerically in Matlab, by imposing the boundary conditions $G(\sqrt{3}/2) = 1$ (at the tetrahedron) and $G(\infty) = 0$, and solving the equation for each eigenvalue k to obtain a set of functions G_k. As one would expect we find that for larger k the solutions become more localised around the tetrahedron and tail off to zero more quickly. Note that for numerical reasons we do not actually impose the boundary condition at ∞, but rather at a sufficiently large value of ϵ such that the functions have all decayed to sufficiently near zero. It was found, by experimenting with various values for the cutoff, that imposing the boundary condition at $\epsilon = 10$ was adequate for this purpose.

In what follows we choose our parameters to be $\omega = \sqrt{3}$ and $\mu = 8\sqrt{2}$, in line with [30], and we seek to solve our equation on only the red region of F, and then later we will use the transformations we saw earlier to map to the full solution on the whole of F.

For the various states that we will be interested in we have seen that there will be two different types of boundary condition on the curved boundary of the red region. For some states, including the ground state that we will discuss shortly, the condition will be that the derivative of the wavefunction normal to the boundary should be zero, and for other states it will be the case that we require the value of the wavefunction itself to be zero on the boundary.

The procedure that we will use to calculate our energy E and coefficients a_i will be as follows. We first select m points (η_i, ϵ_i) on the curved boundary from $\eta = 0$ to $\eta = 1/2$ where these points satisfy the equation of the red/blue boundary (4.18) such that $\epsilon_i = \sqrt{1-\eta_i^2}$. We recognise that the curved boundary from $\eta = 1/2$ to $\eta = 1$ is then related by either symmetry or antisymmetry depending on the parity of the state (symmetry in the case of the ground state as it has positive parity). We also have n unknown coefficients from a_1 to a_n (in principle n should go to ∞ but we can truncate the sum at a finite point as the coefficients approach zero). We can then construct an $m \times n$ matrix $\tilde{\Pi}$ whose entries take one of two possibilities depending on the boundary conditions.

For the simpler case where we have the condition $\phi = 0$ on the curved boundary, the entries of $\tilde{\Pi}$ are

$$\tilde{\Pi}(i,j) = H_j(\eta_i)G_j(\epsilon_i), \tag{4.34}$$

for $i = 1 \dots m$ and $j = 1 \dots n$. We use notation such that G_j and H_j are the solutions of the respective ODEs corresponding to the jth eigenvalue k_j. We then define an $n \times 1$ column vector $\tilde{\Gamma}$ whose entries are all the coefficients from (4.29), that is

$$\tilde{\Gamma}(i) = a_i, \tag{4.35}$$

where $i = 1 \dots n$. We will then make a first guess for a value of the energy E and look to solve the equation $\tilde{\Pi}\tilde{\Gamma} = 0$ for the coefficients. We do however

run into a couple of difficulties when doing this. Firstly, when attempting to solve this system numerically we will always end up returning the trivial solution, that is $a_1 = a_2 \cdots = a_n = 0$. Clearly this is not the solution we are interested in, and we get around this by fixing $a_1 = 1$. This means we have to slightly redefine $\tilde{\Gamma}$ and $\tilde{\Pi}$ as Γ and Π, and introduce a new vector Ω as follows

$$\Gamma(i) = a_{i+1} \text{ for } i = 1..n-1, \tag{4.36}$$

$$\Pi(i,j) = H_{j+1}(\eta_i)G_{j+1}(\epsilon_i) \text{ for } i = 1..m, j = 1..n-1, \tag{4.37}$$

$$\Omega(i) = -H_1(\eta_i)G_1(\epsilon_i) \text{ for } i = 1..m, \tag{4.38}$$

and then seek to solve the system

$$\Pi\Gamma = \Omega \tag{4.39}$$

for the remaining $n-1$ coefficients. We then observe a potential second difficulty which is that we may have an overdetermined system. Solving (4.39) essentially means solving m equations for $n-1$ unknown coefficients. Therefore in order for the system to be solvable we must have at least $m = n-1$ in which case the system is not overdetermined, but if we want to take lots of boundary points which we might expect to improve accuracy, then this would give $m > n-1$. Fortunately Matlab has a routine for solving such a system even if it is overdetermined, using a least squares fitting method. The routine also calculates an error associated with the fitting. Our aim is

to find the value of E that minimises this error and this will be our energy eigenvalue. We do this by sweeping through a range of values of E and determining the error for these energies, and ultimately constructing an error function of which we can then easily look for a minimum. We perform a wide scale sweep to roughly identify the locations of the minima and then perform a golden ratio bracketing search [57] to precisely identify the value of E at which the minimum occurs, up to a desired degree of precision.

For the $\partial_\perp \phi = 0$ boundary conditions the approach is the same, but the matrix Π and the vector Ω are different. The condition now is no longer $\phi = 0$ on the boundary but rather $\nabla\phi.\hat{\alpha} = 0$ where

$$\nabla\phi = \left(\sum_n a_n H'_n(\eta) G_n(\epsilon), \sum_n a_n H_n(\eta) G'_n(\epsilon) \right) \tag{4.40}$$

and $\alpha = (\eta, \sqrt{(1-\eta^2)})$ parametrises the curve. Ultimately it can be shown that

$$\Pi(i,j) = \eta_i H'_{j+1}(\eta_i) G_{j+1}(\epsilon) + \epsilon_i H_{j+1}(\eta_i) G'_{j+1}(\epsilon_i) \text{ for } i = 1..m, j = 1..n-1, \tag{4.41}$$

$$\Omega(i) = -(\eta_i H'_1(\eta_i) G_1(\epsilon_i) + \epsilon_i H_1(\eta_i) G'_1(\epsilon_i)) \text{ for } i = 1..m, \tag{4.42}$$

and we then again seek to solve (4.39) with the modified Π and Ω.

We then have a value of E and coefficients a_i and can construct our solution ϕ in the red region. We can then use the various maps shown previously to map the solution to the other coloured regions of F to get our

full solution.

It is important to note that this numerical method is different to the one used in [30]. They use a method that involves calculating the null eigenvector of a matrix to give the coefficients. Clearly if our method is reasonable we should produce the same results. One advantage of our method is that it is less reliant on the ODEs for G and H having analytic solutions, as everything is done numerically.

Let us briefly consider how we select our boundary points. There are several ways we could do this. Remember we want to choose points along the curve $\epsilon = \sqrt{1-\eta^2}$ from 0 to 1/2 which forms the left hand part of the curved boundary of the red region. It is natural to take equally spaced points as there is no obvious reason to concentrate the points at any particular part of the curve, since there is no one part of the curve where the function is likely to be significantly more complicated or interesting than elsewhere. We can however ask exactly what we mean by equally spaced. One simple possibility is to choose points equally spaced in the η direction (notice that choosing equally spaced points in the ϵ direction is also possible but not as good, since the ϵ distance is very small so the points get squashed together very quickly and one gets very few points close to $\eta = 0$). However, although these points are equally spaced in one direction, the distance along the curve between each pair of points is not equal. We could change this relatively simply. Note that the curve is a part of the unit circle so we can parametrise it by $\eta(t) = \sin(t)$ and $\epsilon(t) = \cos(t)$. This is a slightly unorthodox parametrisation

as we are starting at the top of the circle rather than the right most point as is conventional, since the right most point does not appear on the part of the unit circle we are parametrising. It is nonetheless a perfectly good parametrisation for $t = 0..\pi/6$. We could then take points which are equally spaced along t and these would be spaced at equal distances along the curve. A last and most complicated option comes from recalling that the complex upper half plane $\mathbb{H}$ can be thought of as having hyperbolic geometry, and so one can instead use hyperbolic distance measures to determine the distance between boundary points. This means equipping a non-Euclidean metric to $\mathbb{H}$, and convention is to take $ds^2 = (dx^2 + dy^2)/y^2$. For this metric the magnitude of the velocity along our boundary curve is given by

$$v(t) = \frac{1}{\epsilon(t)}\sqrt{\left(\frac{d\eta}{dt}\right)^2 + \left(\frac{d\epsilon}{dt}\right)^2}, \tag{4.43}$$

and we can then substitute in the parametrisation of our circle. Note that for the Euclidean case we get $v(t) = 1$ as the curve is already arc length parametrised. In the hyperbolic case we find $v(t) = \sec(t)$. We can then determine the arc length parameter s by integrating the velocity to find

$$s = \int_0^t \sec(\tau)d\tau = \ln(\sec(t) + \tan(t)). \tag{4.44}$$

We can then invert this function to find t as a function of s which yields

$$t = \arccos(\operatorname{sech}(s)), \tag{4.45}$$

which we then substitute back into our curve parametrisation giving $\eta(s) = \sin(\arccos(\text{sech}(s)))$ and $\epsilon(s) = \text{sech}(s)$. One can check that this indeed an arc length parametrisation of the boundary curve in Figure 4.10 when using hyperbolic geometry. The range of s is $s = 0 \ldots \ln(\sqrt{3})$. We can now consider taking points along the curve that are equally spaced along s and these points would be at equal distances from each other along the curve according to hyperbolic measures. For ease of comparison, all of the points are plotted in Figure 4.10.

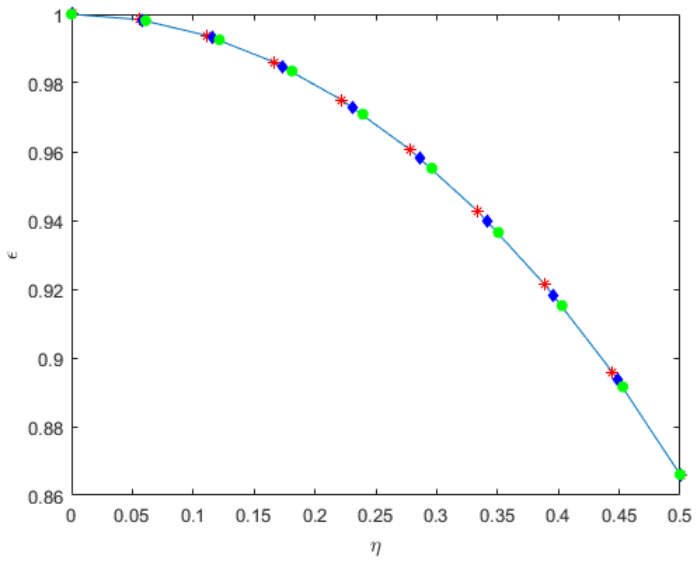

Figure 4.10: A plot showing ten boundary points as selected by the three different methods. The red stars are equally spaced in η, the blue diamonds are equally spaced along the curve using standard distance measures, and the green circles are equally spaced along the curve using a hyperbolic distance measure.

One could make reasonable arguments in favour of any of these three methods of point selection. The first option has the advantage of being

the simplest and the second is also relatively straightforward whilst looking perhaps slightly neater. The third option is more mathematically involved but is very elegant and uses the hyperbolic model of the complex upper half plane which is a natural thing to do in our case as we are thinking of our domain $F \in \mathbb{H}$ as being mapped from a punctured sphere which has non-Euclidean geometry.

In practise however the choice seems to make essentially no difference to the results or to the scale of the error, and so it seems sensible to pick the simplest option of taking equally spaced points in the η direction which we shall do from here on.

Let us now consider the first vibrational wavefunction in the trivial representation. We expect this state to be the lowest energy vibrational wavefunction, which will eventually become the ground state once combined with a suitable spin state. It should have positive parity. We also recall that positive parity states in the trivial representation exhibit the $\eta \mapsto 1-\eta$ symmetry we discussed previously.

This last point is important. The $\eta \mapsto 1 - \eta$ symmetry allows us to say something about the functions $H(\eta)$ that we can take in our solution. The solutions to the Sturm-Liouville problem come in an alternating series, with the first entry having the $\eta \mapsto 1 - \eta$ symmetry, the second being antisymmetric and so on. Therefore since we know in this case we are looking for a symmetric state we include only the even numbered functions $H_0, H_2...$ in our sum. Similarly if we know we are looking for an antisymmetric state (as

we will do later) then we include only the odd numbered functions.

We will first seek to solve (4.31) to obtain a set of functions $H(\eta)$ corresponding to a set of eigenvalues k. Since we are looking for a state with positive parity we know the boundary conditions on the straight lines at $\eta = 0$ and $\eta = 1$ are that the derivative across the lines must be zero, and so we are interested in even solutions $H(\eta)$. The first few functions are shown in Figure 4.11.

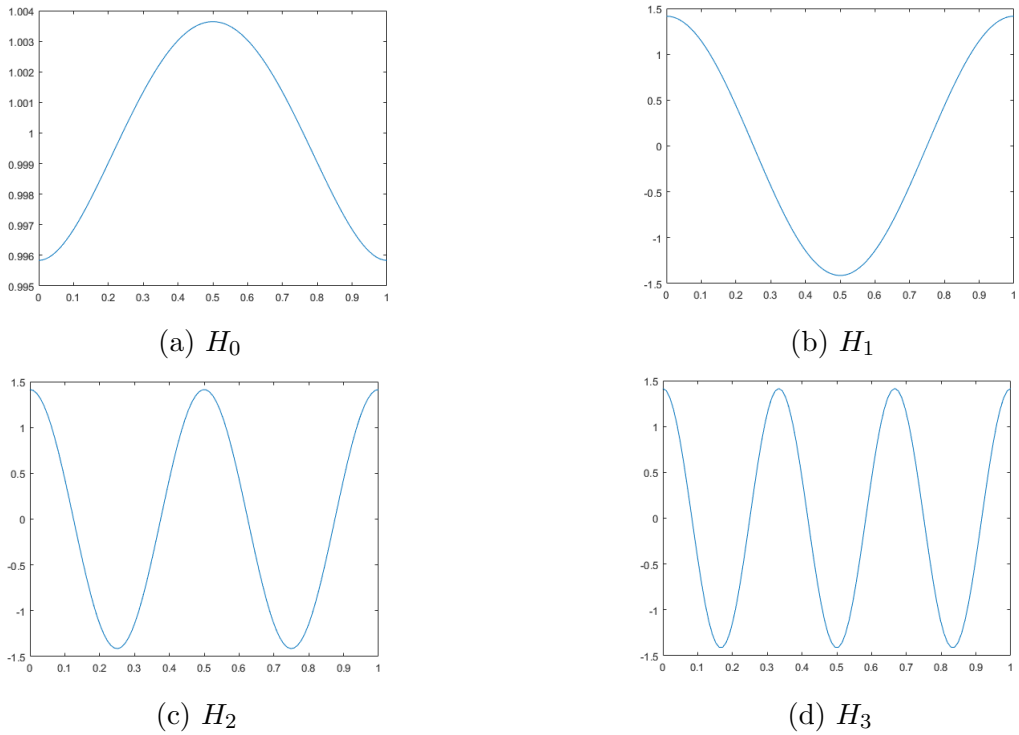

(a) H_0 (b) H_1

(c) H_2 (d) H_3

Figure 4.11: Plots for the first four even H functions we include in our ground state wavefunction solution.

In Table 4.2 we give the first ten relevant eigenvalues k for the ground state (that is to say we have set $n = 10$, which we justify later).

k_n	Eigenvalue
k_1	128.2488
k_2	167.7673
k_3	286.1733
k_4	483.5600
k_5	759.9071
k_6	1115.212
k_7	1549.474
k_8	2062.693
k_9	2654.869
k_{10}	3326.002

Table 4.2: Eigenvalues k for the first ten symmetric functions with even boundary conditions on H.

We can then use the procedure outlined earlier to construct the ground state wavefunction in the red region of F. We first calculate ten functions G_k corresponding to each of the ten eigenvalues k, and place these functions into our sum (4.29). The first few G_k functions are shown in Figure 4.12, and we see they approach zero increasingly quickly as k increases.

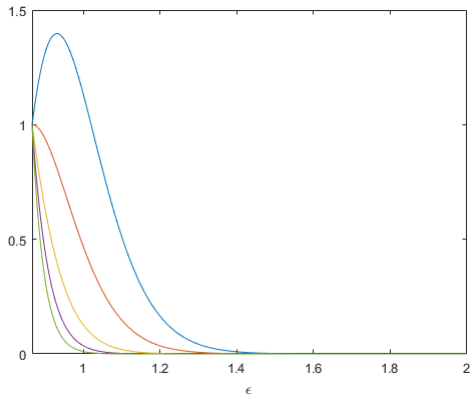

Figure 4.12: The first few functions G_k for the ground state solution.

We fix the first coefficient $a_1 = 1$ and choose m points on the boundary. For the following calculation we choose $m = 20$ but we will discuss this choice later. We then calculate Γ (4.36), Π (4.37) and (4.41), and Ω (4.38) and (4.42), and solve our system.

We calculate an energy eigenvalue to three decimal places of $E = 150.561$, with coefficients shown in Table 4.3. We see that the coefficients after a_1 are decreasing in magnitude as would be expected for the ground state, and approach zero sufficiently rapidly for us to curtail the calculation at $n = 10$. For some of the excited states later on, we shall have to increase the value of n for which we truncate our sum as the coefficients do not approach zero so rapidly, but $n = 10$ is clearly sufficient for the ground state. In fact it turns out that a_{11} and higher coefficients are zero up to the four decimal places quoted in Table 4.3.

Coefficient	Value
a_1	1
a_2	-0.6078
a_3	0.1130
a_4	-0.0144
a_5	0.0027
a_6	-0.0009
a_7	0.0002
a_8	-0.0007
a_9	-0.0008
a_{10}	-0.0008

Table 4.3: Coefficients a for the ground state wavefunction.

The least squares 2-norm fitting error associated with this calculation is

0.0015. Of course, the numerical value of the error will depend upon the number of function n and boundary points m that are chosen, but for any values of n and m the minimal value of the error is located at this value of E to an acceptable level of precision.

In Figure 4.13 we display a contour plot of the ground state vibrational wavefunction in the red region. We use the colouring convention that red

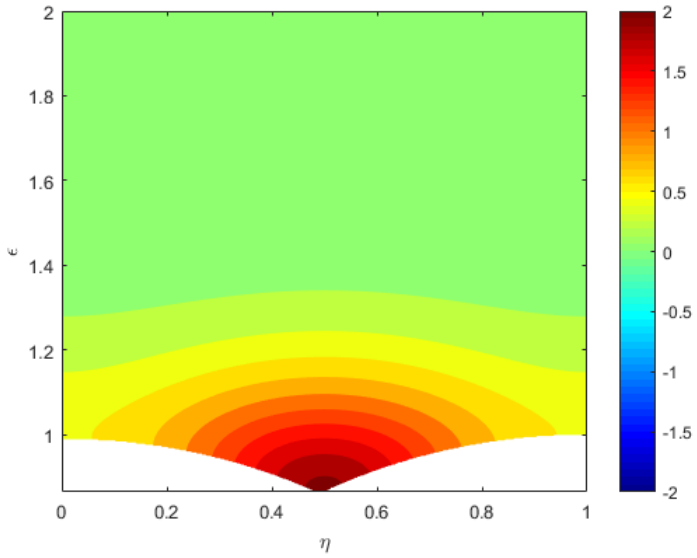

Figure 4.13: A contour plot of the ground state vibrational wavefunction in the red region of F.

is positive, blue is negative and pale blue/green is zero. We now want to be able to go from these pictures to ones on the whole of F which we shall investigate in the next section.

4.7 Mapping to the full solutions

At this point we appreciate the fact that we can use our matrices A and B to map our red region solution to the full region F. If we could not do this, obtaining the solution on the full space would be very laborious as we would have to transform the kinetic operator Δ_{vib} and the potential function, and then re-solve the transformed Schrödinger equation. To demonstrate the challenges this would entail we calculated the transformed potential and kinetic operator and display them below. Recalling our original potential in the red region as (4.28), which we will refer to here as V_{red}, the transformed potentials are

$$V_{\text{green}} = \frac{2\epsilon^2(13\epsilon^4 + 26\epsilon^2\eta^2 + 13\eta^4 - 50\epsilon^2\eta - 50\eta^3 + 50\eta^2)}{(\epsilon^2 + \eta^2)^4} \tag{4.46}$$

and

$$V_{\text{blue}} = \frac{2\epsilon^2(13\epsilon^4 + 26\epsilon^2\eta^2 + 13\eta^4 - 2\epsilon^2\eta - 2\eta^3 - 24\epsilon^2 - 22\eta^2 - 2\eta + 13)}{(\epsilon^2 + \eta^2 - 2\eta + 1)^4}. \tag{4.47}$$

The transformed kinetic operator is also far more complicated. Instead of containing simply second order derivatives in η and ϵ with coefficient ϵ^2, it now contains additional first order terms with far more complicated coefficients, although it should be noted that the mixed second derivative term still remains zero. The coefficients were calculated but are too complicated to list here. Clearly, solving the Schrödinger equation with these functions

would be a tedious task but fortunately this is not necessary here. Instead we apply the relevant transformations (see Figure 4.4) directly to our solution and transport the wavefunction into the other coloured regions.

Doing this for the ground state we produce Figure 4.14. Note that as we expect the ground state is fully localised around the two global minima at the tetrahedral configurations. We can now go through the same process for the

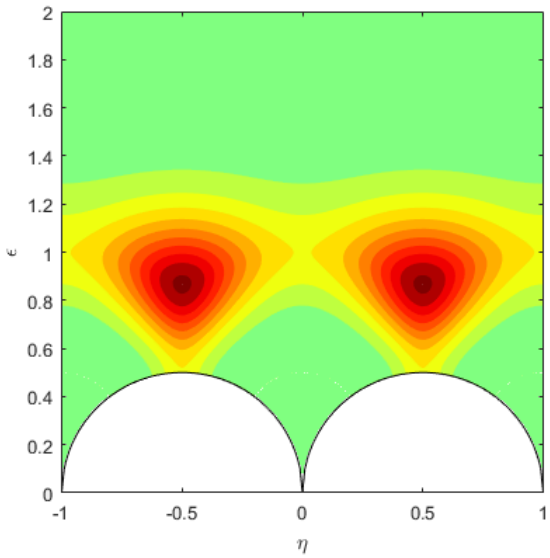

Figure 4.14: A contour plot of the ground state vibrational wavefunction on the full region F.

lowest energy state in the sign representation. We expect this to be a negative parity state because as we argued previously states in the sign representation with positive parity are forced to have nodes at the tetrahedron so are forced away from the energy minima. recall that the lowest spin state allowed for the sign representation is $J = 3$ so we can identify this with an experimental 3^-

state. For a negative parity sign state we have the same boundary conditions on the curved boundaries as the ground state solution, from the arguments previously discussed. We end up with Figure 4.15. Again we see this is

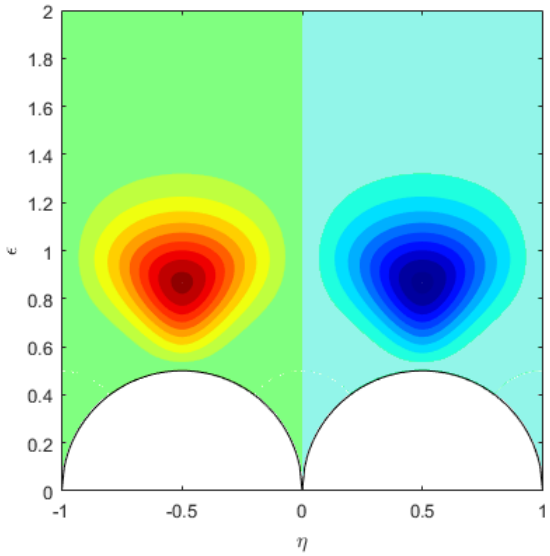

Figure 4.15: A contour plot of the lowest energy vibrational wavefunction in the sign representation.

localised entirely around the tetrahedron, this time with one positive peak and one negative peak, and a nodal line at $\eta = 0$ as a result of the negative parity.

We now consider looking for some excited states with the same parity and boundary conditions. In Figure 4.16 we display the first two excited states in the trivial and sign representations. These states have the same boundary conditions and parities as the lowest energy state in each representation. We see that the excited states in the trivial representation now have additional

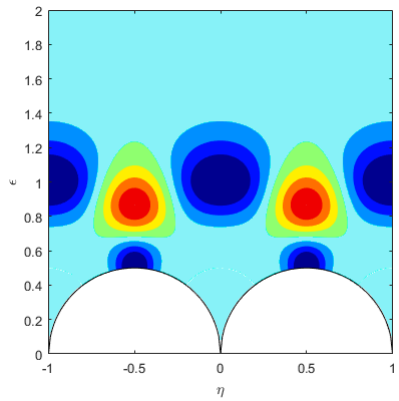

(a) First excited trivial state

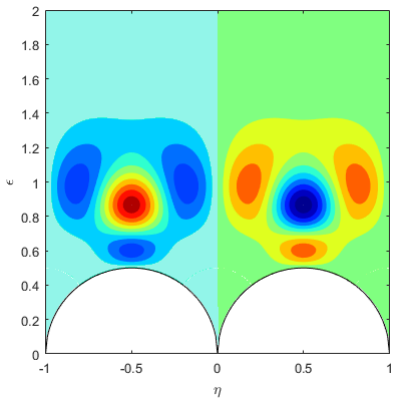

(b) First excited sign state

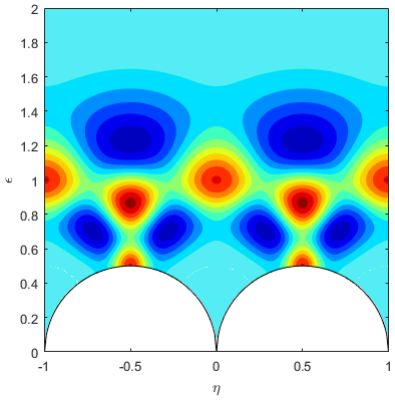

(c) Second excited trivial state

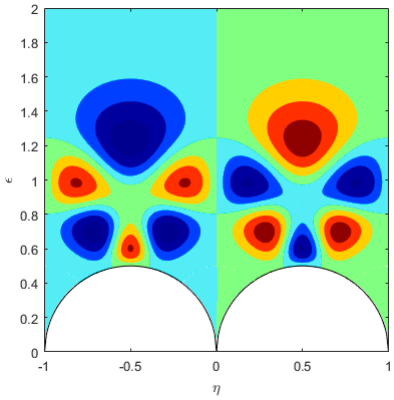

(d) Second excited sign state

Figure 4.16: Plots for excited vibrational wavefunctions in the trivial (left) and sign (right) representations.

localisations around the squares as well as the tetrahedron. This seems fairly natural as we might expect the first excited state to seek out other local stationary points away from the global minimum. Furthermore, for the second excited state we have additional excitations away from both the tetrahedron and the square. Also notice that in the sign representation we get localisations close to but not at the squares. This is because the square is forbidden for all negative parity states since the square sits at $(0, 1)$ which lies on the line $\eta = 0$, and negative parity states are forced to be zero on this line.

Notice that for the excited states we might want to include more functions, as argued previously. As an example, we take $n = 20$ for this state and show the coefficients calculated in Table 4.4. We see that the first couple of coefficients are in fact larger in magnitude than a_1, and that the rest of the coefficients do not tail off to zero quite as quickly as for the ground state. This justifies taking a larger value of n. This is something we will need to do for most of the excited states we are about to see. Since our potential goes off to ∞ for large ϵ rather than approaching some finite value, we expect that we would have an infinite spectrum of discrete states. This is indeed the case but for higher excited states we find that we simply pick up extra oscillations in the ϵ-direction. These are not especially interesting and do not seem to correspond to any physical states so we do not go any further here. Note that for all of the excited states we have just displayed, the key point is that they are centred around more than one configuration and so could never have been derived from rigid body quantisation alone. This means that these are

Coefficient	Value
a_1	1
a_2	-10.4451
a_3	2.5588
a_4	-0.1866
a_5	0.0247
a_6	-0.0069
a_7	0.0055
a_8	0.0005
a_9	0.0035
a_{10}	0.0007
a_{11}	0.0026
a_{12}	0.0069
a_{13}	0.0137
a_{14}	0.0273
a_{15}	0.0498
a_{16}	0.0674
a_{17}	00623
a_{18}	0.0318
a_{19}	0.0045
a_{20}	-0.0019

Table 4.4: The first twenty coefficients for the first excited vibrational wavefunction in the trivial representation.

definitely new states to come out of this approach.

So far we have considered only positive parity trivial representation states and negative parity sign representation states. The reason for this is that we are primarily interested in the low energy spectrum for Oxygen-16, and we expect that negative parity states in the trivial representation and positive parity states in the sign representation will have much higher energies. The reason for this is that these states are forbidden by boundary conditions to be located around either the tetrahedral or square configurations, which will force up their energies considerably. However, we can still consider these cases as potential excited states. We display the first such states in the trivial and sign representations in Figure 4.17. Both of these states are zero on the

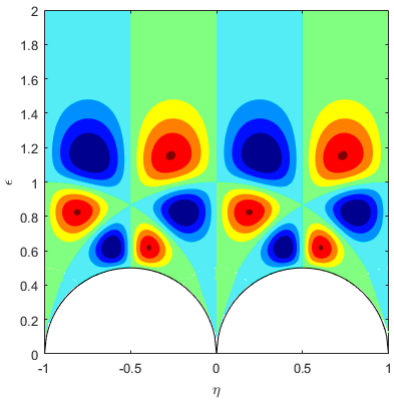

(a) First negative parity trivial state

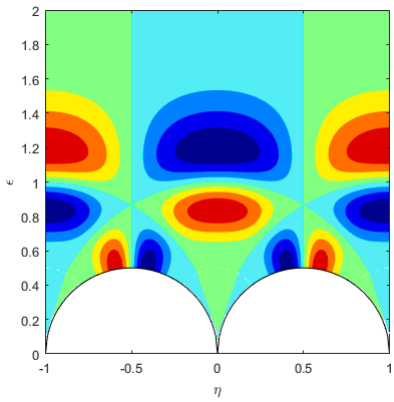

(b) First positive parity sign state

Figure 4.17: Plots for excited vibrational wavefunctions in the trivial (left) and sign (right) representations, with opposite parities.

curved internal boundaries, and as expected have much higher energies than the first states with the more natural choice of parity.

So far, we have not displayed any results for states in the standard representation. Unfortunately, we ran into difficulties calculating the standard representation states in MATLAB. The reason for this is to do with the boundary conditions. Recall the method we outlined earlier in this section for fixing the boundary conditions on standard representation states, where we divided our region F into four regions, rather than the six we had used for the other representations. The new larger region that we consider now has a potential that must be defined in a piecewise way, as it is defined differently in the two parts of the new region. However, because the boundary separating the two parts of the potential is a curve relating both η and ϵ, it is not possible to define the potential in a piecewise way that is also separable. Therefore if we wish to use separation of variables, this method of defining the boundary conditions is not practicable, but as we shall see later in this section it is the correct method to use when considering a full two-dimensional numerical approach. For separation of variables though, we must consider trying to solve for the standard representation states only on the original red region of F. For the trivial and sign representations, we applied the boundary condition on the left hand curved boundary and used a symmetry argument to fix conditions on the right hand curved boundary. However, for the standard representation recall that the relevant symmetry, $\eta \mapsto 1 - \eta$, is not exhibited by the combinations $u + w$ and $u - w$ for which we can fix a boundary condition on the left hand curve. The technique used in [30] is to leave the right hand boundary curve open with no imposed con-

dition. However, when we attempted to apply this method, we encountered a problem, specifically that the eigenfunctions we calculated would concentrate themselves near the open boundary, and satisfy the condition on the left hand boundary curve by always being essentially zero close to it. An example of such an eigenfunction, intended to be the first $u+w$ state, is shown in Figure 4.18. This eigenfunction is clearly erroneous, and there is evidently an error in our method. Fortunately, we shall shortly present a more rigorous method for solving the problem using two-dimensional numerics, so we shall not dwell on attempting to rectify this flaw in the separation of variables calculation.

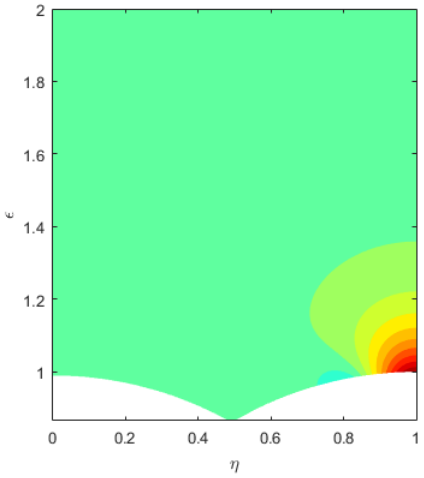

Figure 4.18: A failed attempt to calculate a standard representation state using separation of variables.

4.7.1 Comments on the parameters

So far we have made the same parameter choice for ω and μ found in [30]. However we can consider what happens if we change the parameter values. For example we considered the pairing $\omega = 10$ and $\mu = 1$. Most of the states look very similar, although the numerical energies we calculate are very different before calibration. One visual difference we do notice for these parameters is that we do not find states that look like the first excited states we found previously for the trivial and sign representations. We instead find that when we look for excited states we go immediately to states that have oscillations in the ϵ-direction. For completeness, we display the contour plots for these states in Figure 4.19.

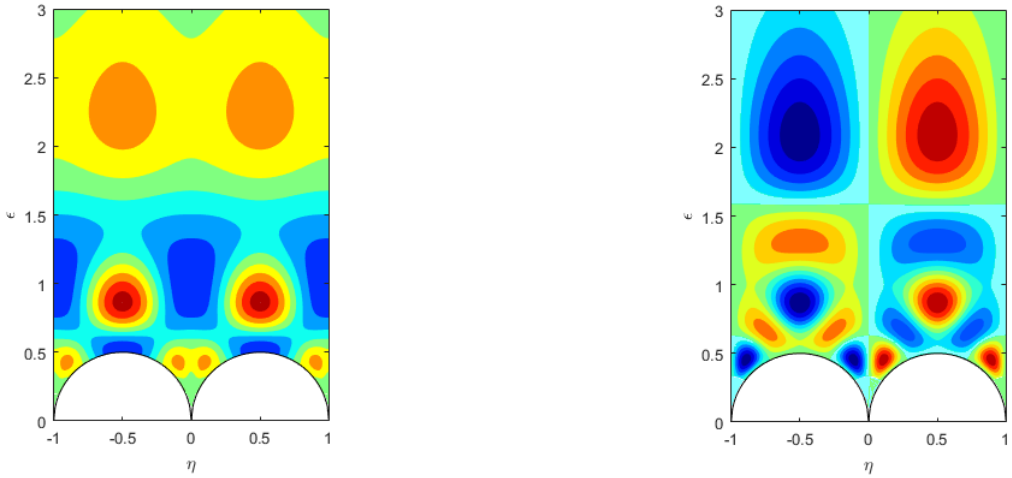

(a) (b)

Figure 4.19: Plots for excited vibrational wavefunctions with $\omega = 10$ and $\mu = 1$.

The rest of the states look very similar. The main reason for the choice of

parameters made in [30] is that after calibration they yield a plausible spectrum for the Oxygen-16 nucleus when compared with experimental values, as we shall see shortly.

4.8 Allowed spins in the different representations

We have been solving (4.2) to obtain vibrational wavefunctions, but these must be combined with spin states to form rovibrational states [30]. The combinations that are permitted depend upon the representation into which the wavefunction falls.

We will denote a rovibrational wavefunction by $\phi\,|\Theta\rangle$, where ϕ is the vibrational wavefunction and $|\Theta\rangle$ is the spin wavefunction. Rovibrational states in the trivial and sign representations can be determined quite easily. For vibrational wavefunctions in the trivial representation, the attached spin state must be invariant under all elements of S_3, both transpositions and permutations. On the other hand, the spin states that are attached to the sign representation vibrational wavefunctions must be invariant under permutations but change sign under transpositions. Ultimately, this sign factor for sign representation states means that spin states with positive intrinsic parity can be combined with trivial representation vibrational wavefunctions, and spin states with negative intrinsic parity can be combined with sign representation vibrational wavefunctions.

As such, if we consider the states in Table 4.1, the first allowed states that can be combined with lowest energy trivial representation state are spin-0 and spin-4 states

$$|0,0\rangle \text{ and } |4,4\rangle + \frac{\sqrt{14}}{5}|4,0\rangle + |4,-4\rangle\,, \tag{4.48}$$

since these states are allowed at both the tetrahedral and square configurations, as is necessary for this state which has positive intrinsic parity. In the sign representation, we look for spin states with negative intrinsic parity, meaning that they vanish at the squares. This tells us the first allowed spin state that can be combined the lowest energy vibrational state in the sign representation is a spin-3 state

$$|3,2\rangle - |3,-2\rangle\,, \tag{4.49}$$

which is permitted at the tetrahedron but forbidden at the square. If one again consults Table 4.1, we can see that for spin-6 there are various combinations of spin-6 states that can be combined with either of these vibrational wavefunctions. We will not go beyond spin-6 in this thesis, since there is little known experimental data for Oxygen-16 beyond this. We also will continue to consider only isospin zero states for simplicity. Some work on states with non-zero isospin has been touched on in [31].

For the excited trivial and sign vibrational wavefunctions, we can make exactly the same argument for the first two excited states in each represen-

tation with the same spin states being allowed in each case. We must also consider the opposite parity states in each representation. For the trivial representation wavefunction with negative parity we make an interesting observation. We denote a rovibrational state with the notation J^P, where J is the spin of the state and P is the parity denoted by either $+$ or $-$. It is possible to construct a 0^- state by combining the $|0,0\rangle$ spin state, which has positive intrinsic parity, with this vibrational wavefunction as it vanishes at all configurations with intrinsic parity. This is an important point as the rigid body method does not allow for a 0^- state, and such a state is known to exist experimentally. This observation in fact holds for higher spin states too. That is to say that because the vibrational wavefunction in question vanishes at all points with intrinsic parity, it can readily be combined with the same spin states (spin-4 and spin-6) as the lowest energy trivial wavefunction. This leads to 4^- and 6^- states. By a similar argument the positive parity sign representation wavefunction is allowed to be combined the same spin states (spin-3 and spin-6) as the lowest energy sign wavefunction, leading to 3^+ and 6^+ states. Again, a 3^+ state is something that had previously been forbidden by the Skyrme model using the rigid body regime.

In summary, the allowed spins J in the trivial representation are $J = 0, 4, 6\ldots$ and the allowed spins in the sign representation are $J = 3, 6\ldots$, with either parity being possible by combination with the correct vibrational wavefunction. Note also that if we combine the ground state vibrational wavefunction with either the spin-0 or spin-4 state given above, or if we com-

bine the lowest energy sign representation wavefunction with the spin-3 state given above, then these states are all concentrated around the tetrahedron. In rigid body quantisation these states, the $0^+, 3^-$ and 4^+ states, form an exact rotational band. In the vibrational picture this is only approximately true, as the energy of the 3^- state lies slightly above this band since the vibrational wavefunction is more constrained by being forbidden to lie at the square.

In the standard representation, we again use u, v and w to describe the vibrational wavefunction and we denote the full rovibrational wavefunction by $u\left|\Theta\right\rangle_1 + v\left|\Theta\right\rangle_2 + w\left|\Theta\right\rangle_3$. We demand that he spin states $\left|\Theta\right\rangle_i$ transform inversely under S_3 compared to the vibrational wavefunctions, for example under a cyclic (1 2 3) permutation they permute anti-cyclically as $\left|\Theta\right\rangle_1 \mapsto \left|\Theta\right\rangle_3 \mapsto \left|\Theta\right\rangle_2$. Let us consider the case of $J = 2$ as an example. For spin-2, $\left|\Theta\right\rangle_i$ are the states with zero projection on the i^{th} axis, meaning they satisfy

$$\hat{L}_i\left|\Theta\right\rangle_i = 0 \text{ and } \left|\Theta\right\rangle_1 + \left|\Theta\right\rangle_2 + \left|\Theta\right\rangle_3 = 0. \tag{4.50}$$

If we consider the vibrational wavefunctions $u + v$ and $u - v$ (recall from our discussion of boundary conditions that these are the combinations that exhibit symmetry or anti-symmetry under $\eta \mapsto 1 - \eta$), and if we consider the first positive parity state in the standard representation, then for spin-2 we

can write down the full wavefunction

$$|\Psi\rangle = \frac{\sqrt{3}}{2\sqrt{2}}(u-v)(|2,2\rangle + |2,-2\rangle) - \frac{3}{2}(u+v)\,|2,0\rangle\,. \tag{4.51}$$

This wavefunction gives a 2^+ state and is concentrated around the square configurations. Indeed at the square, it is the case that u and v are equal and so the first term in the above wavefunction vanishes, and the whole state is proportional to $|2,0\rangle$. This is as expected since this is the only spin-2 state which is permitted at the flat square according to Table 4.1. Note that there are no spin-0 states which are dominated by the square, so the square rotational band begins at spin-2, not at spin-0. This is another difference from rigid body quantisation. Observe also that the state constructed above is written with a two-dimensional basis of spin states. This can also be done for the first negative parity standard representation state. Here the vibrational wavefunction vanishes at the squares so the overall parity is negative, but it can still be combined with the above spin-2 state, with the result now being a 2^- rovibrational state. We can again make similar arguments for higher spins and it turns out that the allowed spins for the standard representation are $J = 2, 4, 5, 6\ldots$, with either parity again being allowed in combination with the correct vibrational wavefunction.

4.9 Energies

4.9.1 Vibrational energies

We now list the numerically calculated energy eigenvalues for the vibrational states we have produced, and they are given in Table 4.5. At this point these values have no physical meaning, but we will discuss shortly how to calibrate them against experimental values, and include the rotational energy corrections (in MeV), so as to give a physical spectrum. Also observe that we do not give energies for the standard representation as these have not been calculated, as discussed previously.

State (J^P)	Numerical Energy
(a)	139.29
(e)	139.67
(b)	171.27
(f)	189.80
(h)	215.78
(c)	216.01
(d)	228.61
(g)	233.64

Table 4.5: The numerically calculated energies for the eight states we have calculated so far. The states are labelled (a) through to (h). States (a) to (c) are the first three states in the trivial representation in order of excitation, with (d) being the trivial representation state with negative parity. Similarly states (e) to (g) are the first three states in the sign representation with (h) being the sign representation state with positive parity.

4.9.2 The rotational energy E_J

So far we have neglected the term E_J in our equation (4.2). The reason for this is that this term depends on the spin J and the spin is in turn dependent on the rotational state with which we choose to combine our vibrational wavefunction. As discussed previously we can choose to combine vibrational wavefunctions in the trivial representation with rotational states of spin $J = 0, 4, 6 \ldots$, vibrational wavefunctions in the sign representation with rotational states of spin $J = 3, 6 \ldots$ and vibrational wavefunctions in the standard representation with rotational states of spin $J = 2, 4, 5, 6 \ldots$. The term E_J then looks like

$$E_J = \frac{\hbar^2}{2\Lambda_{\text{tet}}} J(J+1) + E_J^{(1)}(\eta, \epsilon), \tag{4.52}$$

where Λ_{tet} is the moment of inertia of the tetrahedral configuration. Note that our solutions for Oxygen-16 are not solutions of the full Skyrme model (specifically we do not use a Skyrme potential), but rather our idea is only motivated by Skyrme model and physical observations concerning Oxygen-16 and the $B = 16$ Skyrmion. Therefore we do not have the usual Skyrme calibration of $\hbar = 46.8$. Instead, we have the freedom to choose $\hbar$ arbitrarily, and choosing $\hbar = 1$ is the natural choice. This means that we have to think about the process by which we calibrate our energies, which we discuss later. The second term in equation (4.52) is a small correction term which can be

derived from perturbation theory in line with [30]. It is given by

$$E_J^{(1)} = -\frac{\hbar^2}{2}\int \langle\Psi|\,\nabla^2\,|\Psi\rangle\, dz - \hbar^2\frac{J(J+1)}{2\Lambda_{\text{tet}}}. \tag{4.53}$$

However, since these corrections are relatively small in most cases we do not calculate them here. We will work with only the zeroth order term E^0 for the rotational energy. For a full discussion of the first order term, the reader is referred to [28].

We can clearly observe that if we take only this term, the rotational energy scales like J^2, and is zero for $J = 0$. This means that if we combine our vibrational wavefunctions with a spin zero state (which we can do only for the trivial representation) then there is no contribution from the E_J term. Since the energies we calculated earlier were actually in effect $\tilde{E} = E - E_J$, it is clear that higher spin states will have their actual energies increased by a greater amount compared to what was calculated, as we would expect. The value of Λ will be fixed when we calibrate our rotational energy units later.

4.9.3 Remarks on calibration

We want to calibrate our energies in such a way that they can be compared to experiment. We will do this by first shifting the energies calculated in Table 4.5 such that the ground state has zero energy. We then scale our vibrational energies so that the first excited 0^+ state (b) has energy 6.05 MeV to agree with experiment, and this fixes our vibrational energy units.

When we include the spin state corrections, we scale the rotational energy units such that the lowest lying spin 4^+ state has energy 10.35 MeV, again to agree with experiment. This will also fix a value for Λ in these units. We will give a full table of the calibrated energies later, once we are in a position to also give energies for the standard representation states. We will remark that the calibrated energies of the states (a) to (h) that we have calculated so far are in agreement with the energies originally calculated in [30], up to some very minor differences that may be a result of our slightly different numerical method. In particular, the main flaw highlighted by [30] is that the energy calculated for the 0^- state is too high. The vibrational wavefunction corresponding to this state is (d), the trivial representation state with negative parity. We calculate after calibration that this state has energy 16.90 MeV, whereas the correct experimental value is known to be 10.96 MeV [33]. This overestimation for the energy of the 0^- state is a flaw that we would like to correct, and one possible way to do this is to investigate alternative choices for the potential.

4.10 Alternative potentials

We also have the ambition of investigating what happens for a change of potential. The key feature of the potential chosen in [30] is that it makes the equation (4.2) separable, and so the problem can be reduced from a PDE to two ODEs which is numerically much easier. Let us look at why

the potential (4.28) makes (4.2) separable and if there are any other choices which also have this property. To do this let us go through the process of separation of variables for (4.2) in detail. We start by substituting the ansatz $\phi(\eta, \epsilon) = H(\eta)G(\epsilon)$ into the equation. Using this and the form of the operator given by (4.4) we obtain the equation

$$-\epsilon^2(H''(\eta)G(\epsilon) + H(\eta)G''(\epsilon)) + V(\eta, \epsilon)H(\eta)G(\epsilon) = EH(\eta)G(\epsilon).$$

Dividing through by a factor $\epsilon^2 H(\eta)G(\epsilon)$ yields

$$-\frac{H''(\eta)}{H(\eta)} - \frac{G''(\epsilon)}{G(\epsilon)} + \frac{V(\eta, \epsilon)}{\epsilon^2} = \frac{E}{\epsilon^2},$$

and we can see that this is separable into η and ϵ terms if and only if the term V/ϵ^2 is separable, as the other terms are already separated. We then deduce that the most general form of the potential for which this condition is satisfied is

$$V(\eta, \epsilon) = \epsilon^2(f_1(\epsilon) + f_2(\eta)), \tag{4.54}$$

so that the prefactor of ϵ^2 cancels with the denominator, leaving a term separated into a function of only ϵ and a second function of only η. This yields two separated ODEs

$$H''(\eta) = H(\eta)(f_2(\eta) - k), \tag{4.55}$$

$$G''(\epsilon) = G(\epsilon)\left(k + f_1(\epsilon) - \frac{E}{\epsilon^2}\right), \tag{4.56}$$

where we note that the potential (4.28) that we have used so far has $f_1(\epsilon) = 0$ and $f_2(\eta) = \omega^2(\eta - 1/2)^2 + \mu^2$.

Let us now consider some interesting special cases of (4.54). The most trivial special case is where $f_1(\epsilon)$ and $f_2(\eta)$ are both identically zero and so we have the zero potential. This yields the ODEs

$$H''(\eta) = -kH(\eta) \tag{4.57}$$

$$G''(\epsilon) = G(\epsilon)(k - E/\epsilon^2). \tag{4.58}$$

We see that solutions to $H(\eta)$ are solutions of the classical simple harmonic oscillator problem (sine and cosine functions with suitably determined coefficients) and the equation for $G(\epsilon)$ is the same as our original one and can be solved numerically.

A second case is for us to choose a potential with no dependence on η. That is to say we pick $f_2(\eta) = 0$. Strictly speaking we could choose $f_2(\eta)$ to be some non-zero constant, but if we were to do this we could actually absorb the constant into $f_1(\epsilon)$ and so rescale $f_2(\eta)$ to be zero in any case. This gives the ODEs

$$H''(\eta) = -kH(\eta) \tag{4.59}$$

$$G''(\epsilon) = G(\epsilon)(k + f_1(\epsilon) - E/\epsilon^2), \tag{4.60}$$

where the $H(\eta)$ equation is again that of the classical simple harmonic oscillator and the equation for $G(\epsilon)$ is now slightly more complicated but can still be solved numerically for reasonable choices of $f_1(\epsilon)$. A natural candidate is $\tilde{f}_1(\epsilon) = \omega^2(\epsilon - \sqrt{3}/2)^2 + \mu^2$, where we now write $\tilde{f}_1(\epsilon) = \epsilon^2 f_1(\epsilon)$ to absorb the factor of ϵ^2 for convenience. This choice gives a minimum at $\epsilon = \sqrt{3}/2$, the position of the tetrahedron.

We plot the full potential for this case in Figure 4.20a, and it should be noted that the minimum here is in fact along the whole line $\epsilon = \sqrt{3}/2$ rather than specifically at the position of the tetrahedron.

A natural alternative special case to consider is the potential with no ϵ dependence, but due to the prefactor of ϵ^2 in (4.54) that is necessary to give separability this is not in fact possible (except for the trivial case already discussed). We can consider removing any ϵ dependence from the sum however, that is to say we can fix $f_1(\epsilon) = 0$. Notice that this particular special case includes the potential that we have so far been considering, as the potential (4.28) is simply a factor of ϵ^2 multiplied by a function of η chosen in such a way that there is a minimum at $\eta = 1/2$, the position of the tetrahedron.

For this case more generally, we obtain the ODEs

$$H''(\eta) = H(\eta)(f_2(\eta) - k) \tag{4.61}$$

$$G''(\epsilon) = G(\epsilon)(k - E/\epsilon^2). \tag{4.62}$$

Now it is the equation for $H(\eta)$ that is more complicated, but it can still

be solved as a Sturm Liouville problem for reasonable choices of $f_2(\eta)$. The equation for $G(\epsilon)$ returns to being the same one we have solved previously. An obvious candidate for the choice of $f_2(\eta)$ here is obviously the quadratic chosen by Halcrow and King in [30], but another interesting if slightly more complicated alternative is the quartic function $f_2(\eta) = -\omega^2((\eta - 1/2)^4 + 0.5(\eta - 1/2)^2) + \mu^2$. The advantage of this choice is that it still provides a minimum at $\eta = 1/2$ but now the function has the added benefit of having local maxima at $\eta = 0$ and $\eta = 1$, which gives genuine saddle points at the square configurations when the function is combined with the quadratic in the ϵ-direction. We plot the full potential for this case in Figure 4.20b.

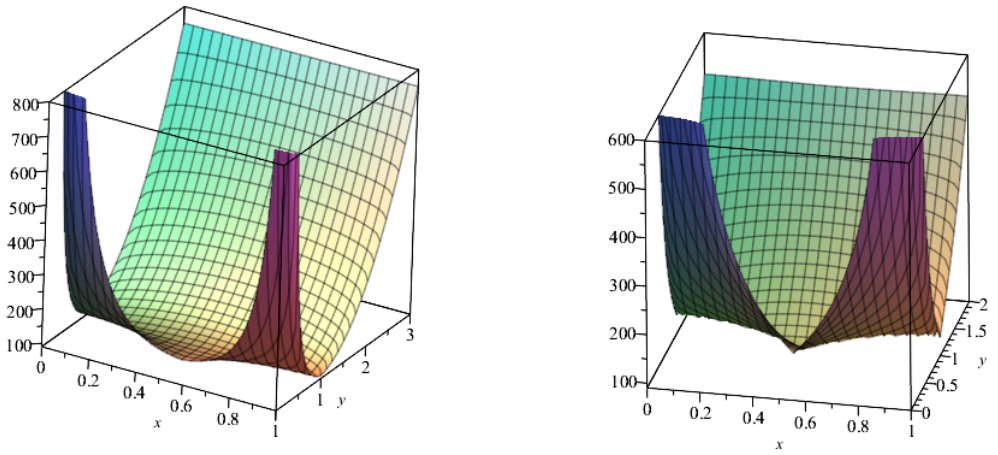

(a) Potential with $f_2(\eta) = 0$.

(b) Quartic Potential

Figure 4.20: 3D plots for the potential with no η dependence and the quartic potential.

Another option for this special case is to choose a sextic potential in η. This would allow us to have a global minimum at the tetrahedron and a

local minimum (rather than a saddle) at the squares. Alternatively we could choose to have a global minimum at the squares and a local minimum at the tetrahedron. The first of these is more physical but the second is consistent with some versions of the Skyrme model, depending on the choice of mass parameters.

We define a sextic potential by taking $f_2(\eta) = a(\eta - 1/2)^6 + b(\eta - 1/2)^4 + c(\eta - 1/2)^2 + d$. We can then vary the shape of our potential by varying the parameters. Recall that for the potential (4.28) we had the square at a value of 128.75 and the tetrahedron at 96. We use these values to motivate our parameter choice for the sextic potential.

For the first case where we want a global minimum at the tetrahedron and a higher local minimum at the squares we choose $a = 5000$,$b = -2512$,$d = 128$ and we require $c = -(3a/16 + b/2)$ to give the right position for the minima. This gives a value of 96 for the tetrahedron and 128.75 for the squares as before.

For the second case where we want a global minimum at the square and a higher local minimum at the tetrahedron we take $a = 20000$, $b = -26416/3$ and $d = 512/3$ with c as before. This puts the squares at 96 and the tetrahedra at 128.75.

We plot the two potentials in Figures 4.21a and 4.21b, and we notice that the first case looks roughly similar to what we had seen before but with small local minima at the squares. The second case on the other hand looks markedly different with pronounced global minima at $(0, 1)$, $(1, 1)$ and

$(1/2, 1/2)$ where the square configurations lie.

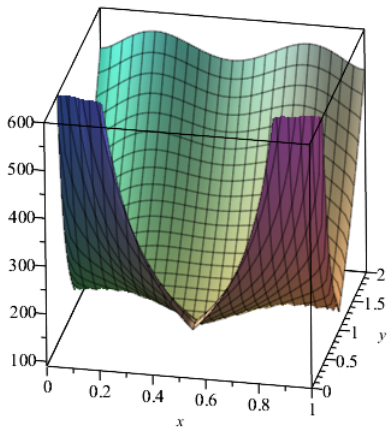

(a) Sextic potential with global minimum at the tetrahedron.

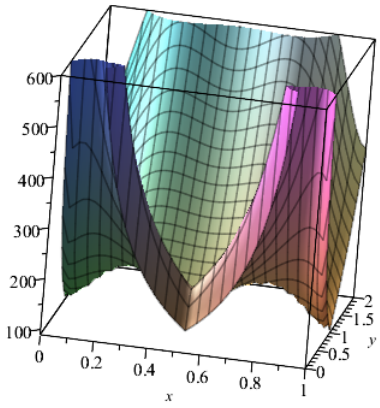

(b) Sextic potential with global minimum at the square.

Figure 4.21: 3D plots of the two sextic potentials.

The two sextic potentials are the most interesting of the various special cases we have discussed so we will now present some results for these potentials.

4.10.1 Results for the first sextic potential

We now present contour plots for the same states that we calculated for the original potential, although this time we only include one of the excited states with the natural parity rather than two. For the first sextic potential the ground state vibrational wavefunction and lowest sign representation wavefunction are displayed in Figures 4.22a and 4.22b. The first excited states in each representation are displayed in Figures 4.23a and 4.23b. Finally, we

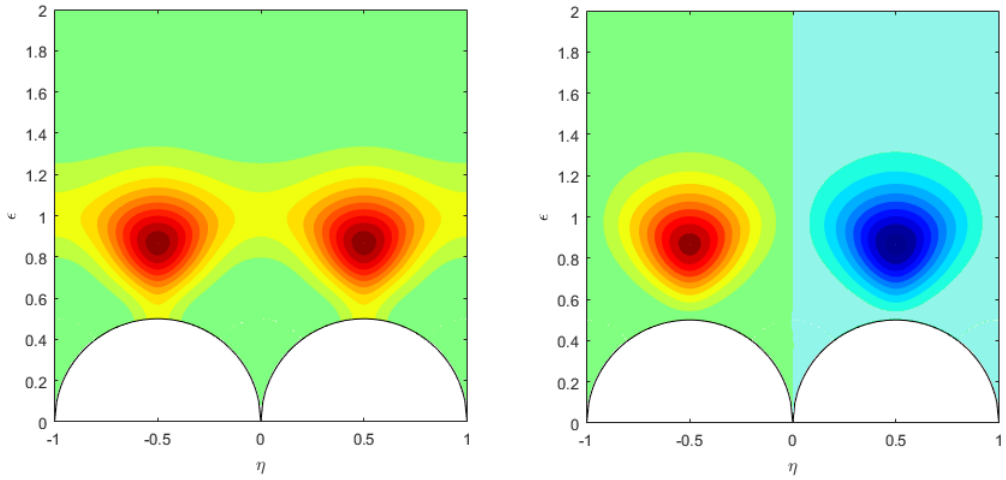

(a) Trivial Representation (b) Sign representation

Figure 4.22: Contour plots for the lowest lying vibrational wavefunctions in the trivial and sign representations respectively, for the first sextic potential.

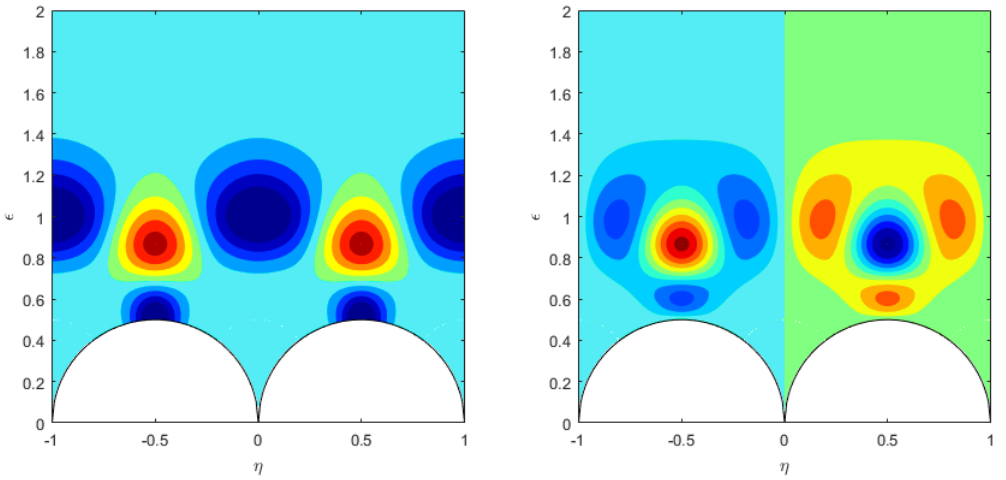

(a) Trivial Representation (b) Sign representation

Figure 4.23: Contour plots for the first excited vibrational wavefunctions in the trivial and sign representations respectively, for the first sextic potential.

display the states with opposite parity in each representation in Figures 4.24a and 4.24b. Again, we do not plot standard representation states here, due

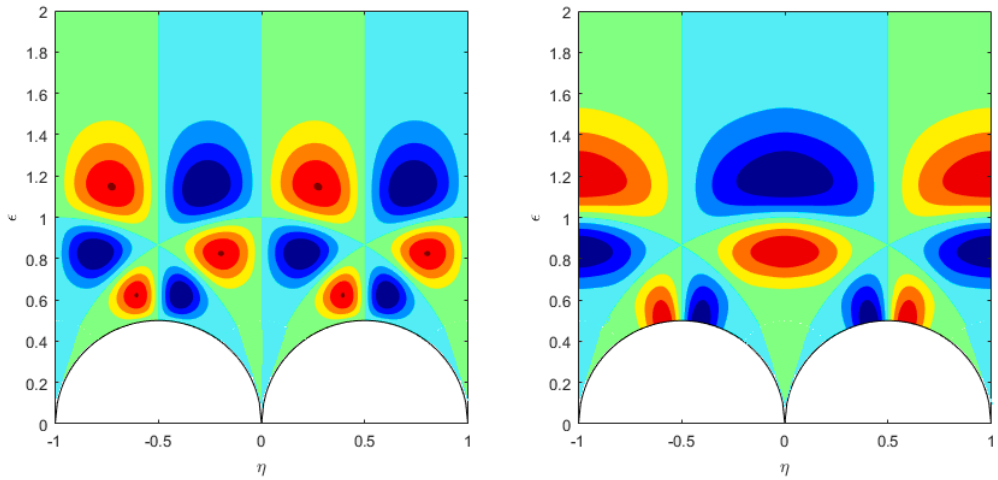

(a) Trivial Representation (b) Sign representation

Figure 4.24: Contour plots for the excited vibrational wavefunctions in the trivial and sign representations with the opposite parity condition, for the first sextic potential.

to the same difficulties as before.

We notice that these pictures all look essentially very similar to the original potential (4.28). This is to be expected as physically not a lot has been changed, with the only difference that the square is now a stable minimum in all directions rather than a saddle point. The shapes of some of the peaks look slightly different but all of the states are still localised around the same points as before.

We can check what this new potential does to our energies, in particular the 0^- state which we hope to correct. We find, after calibration, that the 0^-

state has an energy of 17.78 MeV, compared to the 16.90 MeV we calculated previously. This is very similar and is still too high, so this choice of potential does not correct this flaw.

4.10.2 Results for the second sextic potential

We now present contour plots for the same states for the second sextic potential. The ground state vibrational wavefunction and lowest sign representation wavefunction are displayed in Figures 4.25a and 4.25b. The first

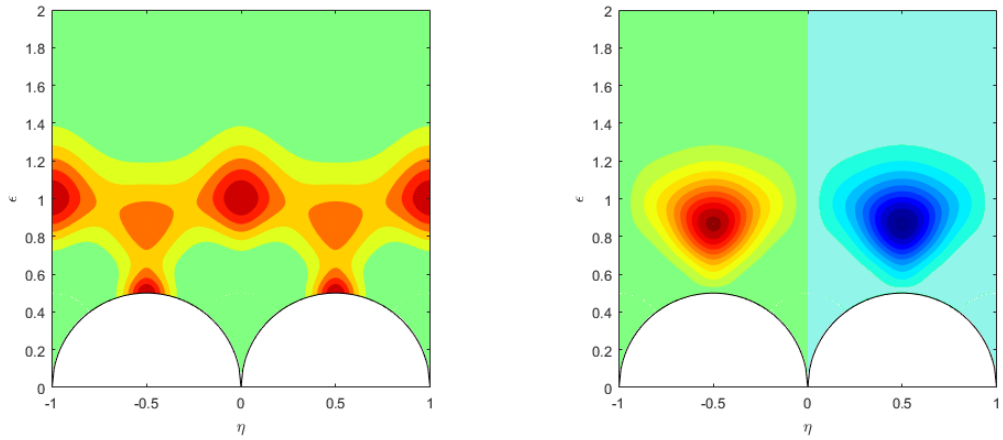

(a) Trivial Representation

(b) Sign representation

Figure 4.25: Contour plots for the lowest lying vibrational wavefunctions in the trivial and sign representations respectively, for the second sextic potential.

excited states in each representation are displayed in Figures 4.26a and 4.26b. Finally, we display the states with opposite parity in each representation in Figures 4.27a and 4.27b.

We notice that these pictures now look somewhat different for some states.

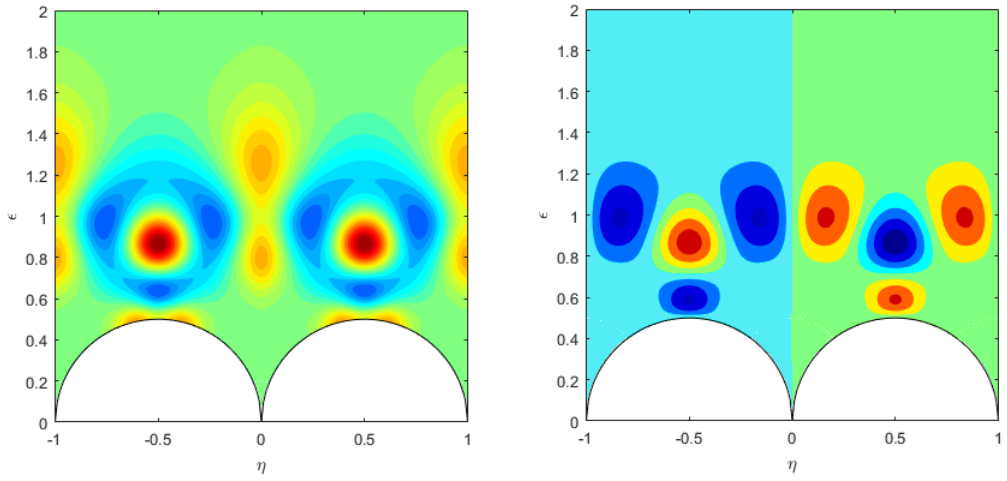

(a) Trivial Representation (b) Sign representation

Figure 4.26: Contour plots for the first excited vibrational wavefunctions in the trivial and sign representations respectively, for the second sextic potential.

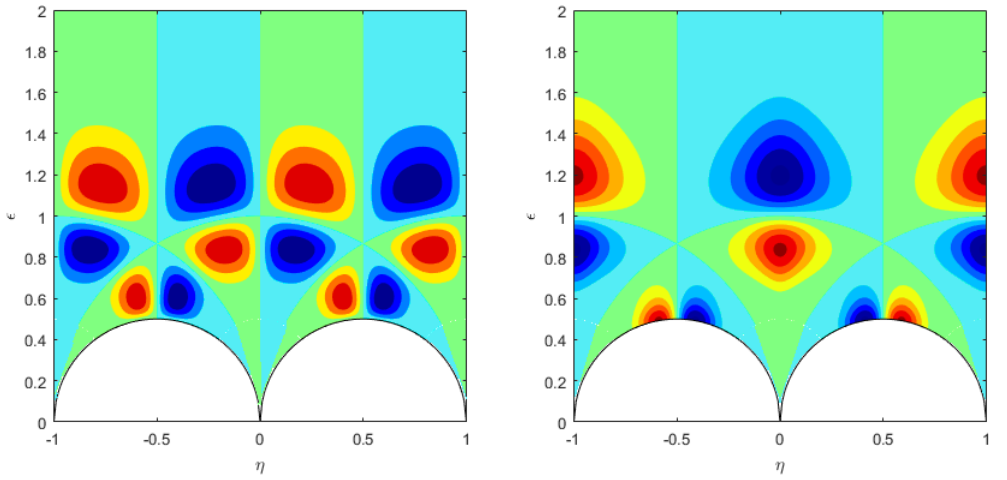

(a) Trivial Representation (b) Sign representation

Figure 4.27: Contour plots for the excited vibrational wavefunctions in the trivial and sign representations with the opposite parity condition, for the second sextic potential.

In particular the ground state is now primarily localised around the squares as we would expect since it is now the global minimum. The first excited trivial state also looks very different and turns out to have a rather higher energy. This will make a difference when we do calibration as we use this state to scale our vibrational units. We also observe that the sign representation states look quite similar to before. The reason for this is that the lower sign states have negative parity and this prevents them from being localised at the squares, indeed they must vanish at those points. As a result they still want to be localised around the tetrahedron as it is the next minimum energy point.

We can again check what this new potential does to the energy of the 0^- state. We find, after calibration, that the 0^- state now has an energy of 6.72 MeV. This is radically different to before and is now too low, but it may be possible for different parameter choices to find something that gives us a value somewhere in the middle, to allow us to get close to the experimental value of 10.96 MeV. This is something that we would like to investigate further in the future, and is one possible avenue for future work. However, we wish to focus for now on the approach laid out in the next section where we use a full two-dimensional numerical approach to replace the separation of variables idea. This will remove the constraints on our choice of potential, and allow us to be much more general.

4.11 A new approach: two-dimensional numerics

So far, we have been severely constrained in the choice of potential we have been allowed to make. However, ideally we would like our potential to satisfy several key criteria. Firstly, we would like it to have a global minimum at the tetrahedral configuration as this agrees with experimental evidence. We would also like the potential to have stationary points at the squares. Additionally, we would like the potential to be smooth (continuous and continuous in derivative) across the boundaries of the coloured regions, as well as flattening off to a finite vacuum value at infinity. We note that the first two criteria were satisfied for our previous choice, but the last two are impossible to satisfy for any separable potential. The smoothness condition is extremely difficult to satisfy as it is very hard to construct a potential in the red region of F that is then continuous in derivative when mapped to the other coloured regions. The finite vacuum condition cannot be satisfied due to the overall prefactor of ϵ^2, as discussed previously. As such, we are motivated to think about going beyond the separation of variables method to solve our problem. This is numerically much more challenging, but we have devised an approach using a finite element method in FreeFEM++ to calculate solutions. The key difficulty in doing two-dimensional numerics for this problem is the unusual boundary conditions, where we have to impose a derivative that is zero normal to a curved boundary, but the finite element

scheme gives us scope to do this.

4.11.1 A proof of concept

Here we will briefly present some results for this method with the original choice of potential (4.28), in order to justify that this more involved method is sound. We present these results in Figure 4.29, and also display the opposite parity states in Figure 4.30. We must also make a remark on the colour scheme that we are using in these figures. The colouring is done such that areas where the wavefunction is negative are coloured blue, areas where the wavefunction is positive are coloured red, and areas where the wavefunction is zero are coloured magenta. A colour key is shown in Figure 4.28.

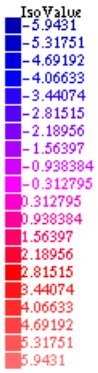

Figure 4.28: The colour key used in the production of the FreeFEM++ figures.

We see that our new plots look the same as for the one-dimensional method, with the exception of a slight discrepancy in the orientation of the darker parts of the blue rings in Figure 4.29e. We are not able to explain

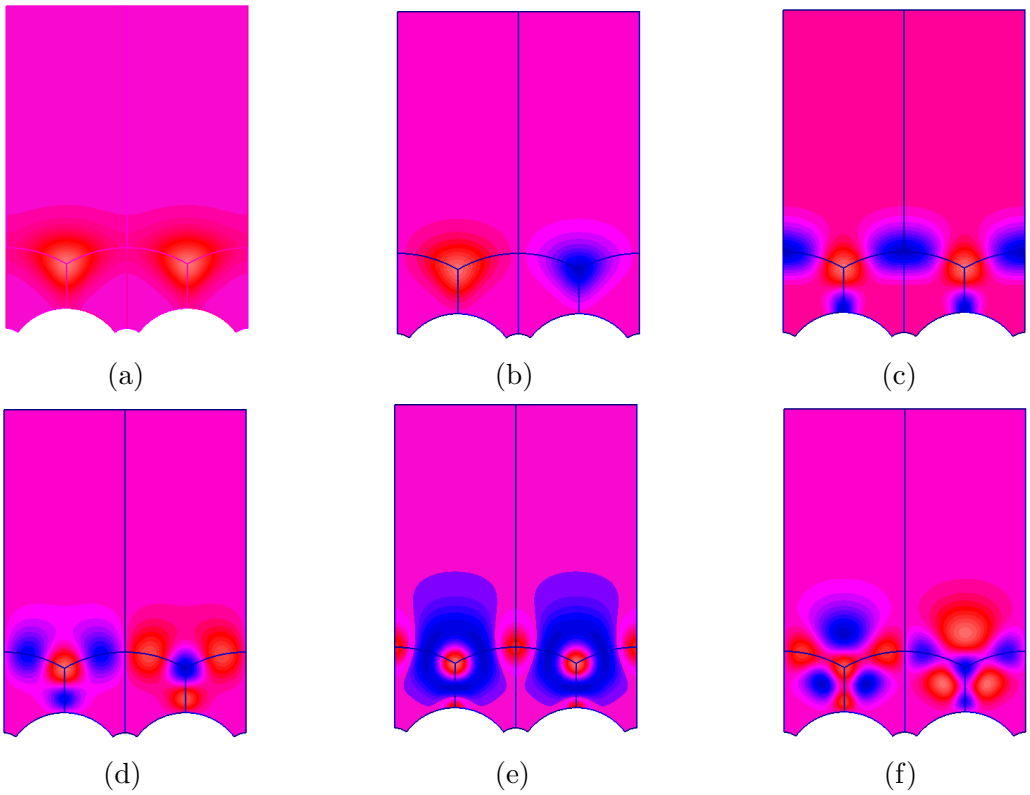

Figure 4.29: Plots for the trivial (left) and sign (right) vibrational wavefunctions calculated using two-dimensional numerics, in order of excitation.

(a) (b)

Figure 4.30: Plots for the trivial (left) and sign (right) opposite parity vibrational wavefunctions calculated using two-dimensional numerics.

this difference, but we can say that the energies of all of the calculated states agree with the energies listed in Table 4.6 up to two decimal places, so clearly the methods are consistent.

Using this new method, we were also finally able to calculate standard representation states. This is very important as we recall that standard representation states are the only vibrational wavefunctions that can be combined with spin-2 states. As such, to produce these states in the Oxygen-16 spectrum, calculating the vibrational energies for these wavefunctions was essential. Recalling that the combinations $u + w$ and $u - w$ were the ones for which we could fix boundary conditions, we plot the first three $u + w$ and $u - w$ wavefunctions with positive and negative parity. Note that these wavefunctions come as energy doublets, that is to say the first $u + w$ state with positive parity has the same energy as the first $u - w$ state with negative parity, and so on for the other states. We plot positive parity $u+w$ wavefunc-

tions in Figure 4.31 and positive parity $u - w$ wavefunctions in Figure 4.32. Likewise, we plot negative parity $u + w$ states in Figure 4.33 and negative parity $u - w$ states in Figure 4.34. Since [30] plots the wavefunctions $u + v$ and $u - v$ for the standard representation, we are not able to compare our plots with the previous results, but it will turn out after calibration that our standard representation energies are consistent with [30].

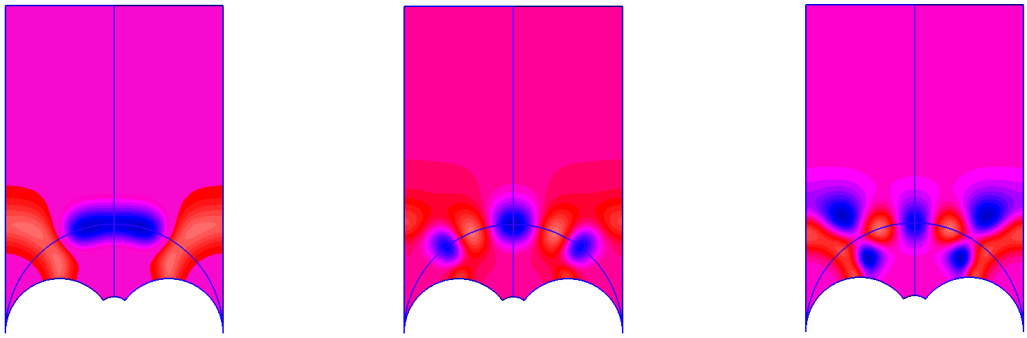

(a) (b) (c)

Figure 4.31: Plots for the first three standard representation wavefunctions $u + w$ with positive parity.

4.11.2 Calibration

We have already discussed the method for calibration, but now that we have calculated energies for all of the states, including the standard representation, we can calibrate all of our energies and generate a spectrum. In Table 4.6 we present the calibrated energies. We give the J^P values of the state and the corresponding vibrational wavefunction. States (a) to (h) correspond to the same vibrational states as before, and now states (i) to (m) are standard

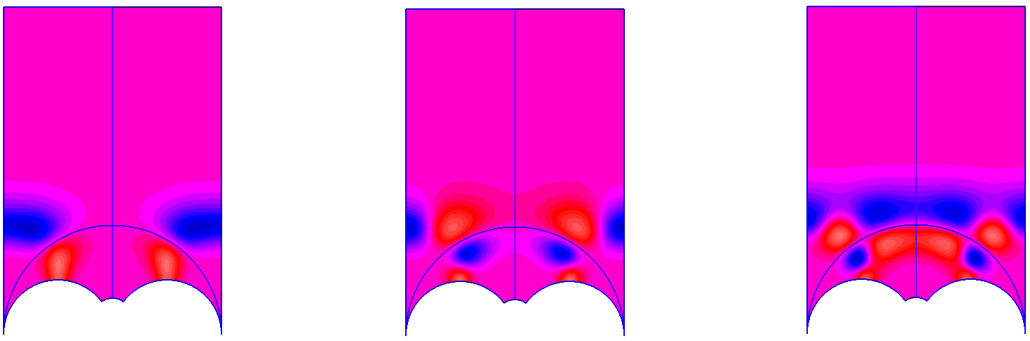

(a) (b) (c)

Figure 4.32: Plots for the first three standard representation wavefunctions $u - w$ with positive parity.

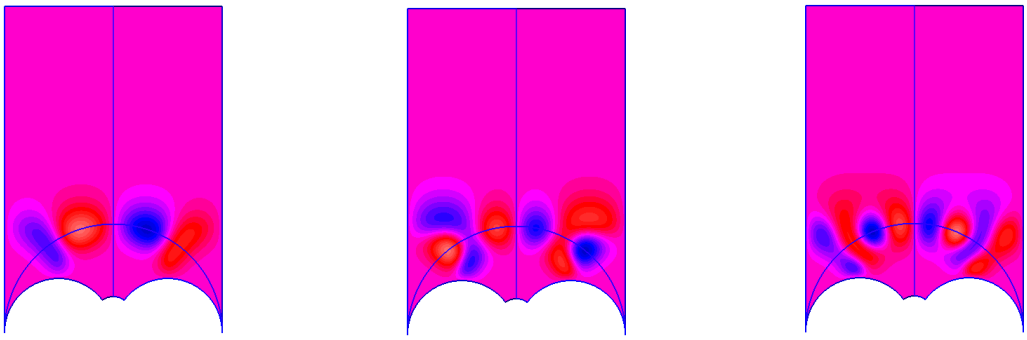

(a) (b) (c)

Figure 4.33: Plots for the first three standard representation wavefunctions $u + w$ with negative parity.

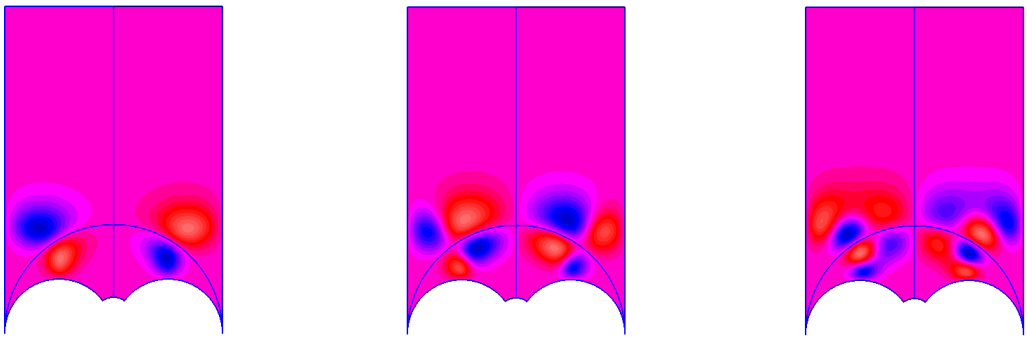

(a) (b) (c)

Figure 4.34: Plots for the first three standard representation wavefunctions $u - w$ with negative parity.

representation wavefunctions. States (i) to (k) are the first three positive parity standard representation states, and states (l) to (n) are the first three negative parity states. We include the vibrational energy, the rotational correction E^0 and the total energy, as well as an experimental value for comparison. The experimental values are taken from [33].

4.11.3 Spectrum

We are now in a position to display an energy spectrum based on our calculations. This is displayed in Figure 4.35. We observe from this spectrum that there is broadly a good agreement with experiment, especially for the low energy states. In particular, we see that the lowest lying $J = 2$ states have the correct order and energy gaps, and the ground state rotational band is well produced.

The most obvious failure of this model is the energy of the first 0^- state

State (J^P)	Vibrational State	E_{vib}	E^0	E_{tot}	Experimental
0^+	(a)	0	0	0	0
0^+	(b)	6.05	0	6.05	6.05
3^-	(e)	0.07	6.21	6.28	6.13
2^+	(i)	4.15	3.10	7.25	6.92
2^-	(l)	5.32	3.10	8.42	8.87
4^+	(a)	0	10.35	10.35	10.35
2^+	(j)	8.83	3.10	11.93	11.52
4^+	(i)	4.15	10.35	14.50	11.10
0^+	(c)	14.52	0	14.52	-
2^-	(m)	11.55	3.10	14.65	12.53
4^-	(l)	5.32	10.35	15.67	14.30
3^-	(f)	9.56	6.21	15.77	-
2^+	(k)	12.83	3.10	15.93	-
0^-	(d)	16.90	0	16.90	10.96
5^+	(i)	4.15	15.53	19.68	-
3^+	(h)	14.47	6.21	20.68	15.79
5^-	(l)	5.32	15.53	20.85	-
6^+	(a)	0	21.74	21.74	21.05
6^-	(e)	0.07	21.74	21.81	-

Table 4.6: A table showing the calibrated energies for different states J^P. We also give the relevant vibrational state, and where the experimental value is known this is listed for comparison. All energies are now given in MeV.

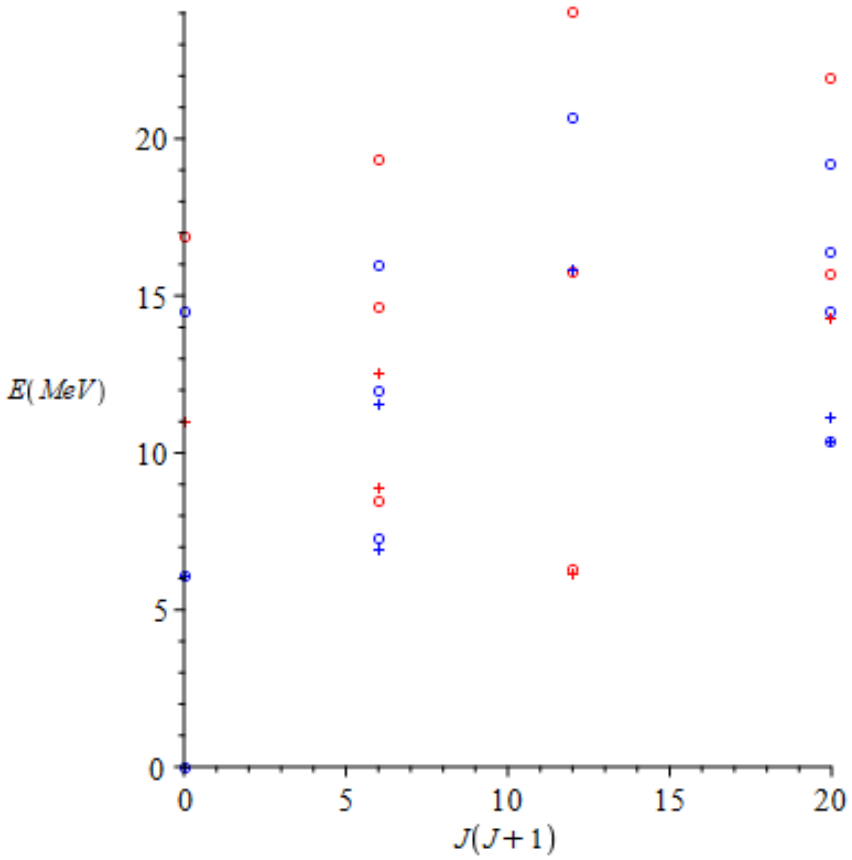

Figure 4.35: A spectrum for Oxygen-16 using the energies calculated in Table 4.6. Here circles represent states we have calculated in our model and crosses represent experimental states. Blue symbols denote states with positive parity and red symbols denote states with negative parity.

as mentioned previously, which is off by approximately 6 MeV. This differs from the experimental value by around 54%. Since the ability to produce a 0^- state in the first place is one of the attractive features of this model, as such a state cannot be found at all in rigid body quantisation, we would like to produce it accurately. We have already discussed some alternative potentials that change this value, but we now move on to a new method, with the aim of improving our results further.

4.12 Constructing a new potential

If we want to construct a potential that satisfies the criteria we outlined previously, we must think how do this. In particular, the two conditions we were previously unable to meet were for the potential to flatten off at infinity and to be smooth across the boundaries of the coloured regions. Constructing a function from scratch that satisfies these conditions is a daunting task, but we have an advantage. We already know several functions that satisfy these conditions, namely any eigenfunction of the Schrödinger equation. Therefore we can build a potential as a combination of eigenfunctions of the Schrödinger equation to achieve a potential with the desired features. Note that it does not matter what potential we use to generate the eigenfunctions, so we will take the zero potential as the simplest case. In particular we are looking to use an eigenfunction centred entirely around the tetrahedra and an eigenfunction centred entirely around the squares. We can then build a linear

combination of these two eigenfunctions to construct a function which has minima at both configurations, of the form

$$V = c_0 - V_{\text{tet}}^{c_1} - \lambda V_{\text{sq}}^{c_2}, \tag{4.63}$$

where we can adjust the parameter λ to change the relative values of the potential at the tetrahedral and square configurations. We also include constants c_0, c_1 and c_2. Since both V_{tet} and V_{sq} vanish at infinity, the parameter c_0 will fix the value to which our potential flattens off at infinity. The powers c_1 and c_2 should both be even in order to ensure that the tetrahedron and square have minima rather than maxima, and taking a higher power will make the potential more highly localised around these configurations. Note also that V_{sq} is a standard representation state and is itself the sum of a $u+w$ state and a $u-w$ state, and these are summed in such a way that the value of V_{sq} is the same at all square configurations.

We display the two base functions in Figure 4.37, and then display the constructed potential in Figure 4.38. In constructing this final potential our motivation was for the tetrahedron and square to have the same values as we used previously, specifically 96 at the tetrahedron and 128.75 at the square, as this gave a good fit for the spectrum. However, we now have our potential with local minima at both configurations, whereas previously the square was only a saddle point, and it is also smooth across all of the internal boundaries. It also flattens off at infinity to the value c_0, in this case we have

taken $c_0 = 300$. We also take the parameters $c_1 = c_2 = 6$ and $\lambda = 1.1$, as these parameters give a distinct separation between the tetrahedron and square minima, and put the values of these minima in line with the values we want. Note that the colour scheme we use for the potential is somewhat different to that used for the wavefunctions in the previous section, as our potential function is positive everywhere and so the colour key is shifted. Blue now represents the minimal values of the potential (but still a positive quantity), red the maximal values and magenta takes values in between. A colour key for the new potential is shown in Figure 4.36.

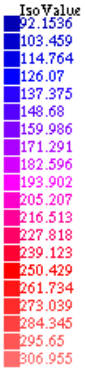

Figure 4.36: The colour key used in the production of the new potential.

It can be observed from a careful consideration of Figure 4.38, that the new potential is not perfectly symmetric under the symmetry $\eta \mapsto 1-\eta$. This may in part be due to a slight deviance in our numerics when we calculate the square centred state (one can see from Figures 4.37 and 4.37 that the tetrahedron centred potential is symmetric, but the square centred one is not). However, it should also be pointed out that since the square centred

(a) V_{tet} (b) V_{sq}

Figure 4.37: Plots for the two functions V_{tet} and V_{sq} from (4.63) that we will use to construct our new potential.

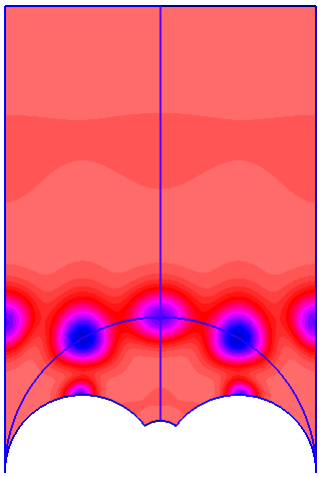

Figure 4.38: The new potential, which is now smooth everywhere and finite as $\epsilon \to \infty$.

potential is a standard representation $u \pm w$ state, there is no reason to expect that it would necessarily have this symmetry in any case. This is a slightly unfortunate feature of this new potential as it will break the $\eta \mapsto 1 - \eta$ symmetry of all of our states, causing them to look somewhat different. A task for future work would be to consider how we might force this potential to be symmetric, when it is composed of an asymmetric state. One possibility is to seek a standard representation wavefunction of the type $u \pm v$ that is centred entirely around the square, as we know that these states exhibit the desired symmetry. Unfortunately, we have not yet identified such a state and so we will continue to use the potential from Figure 4.38 in this thesis. One other partial explanation for the asymmetry is that when we truncate our region at ∞ for large values of ϵ, we also truncate at the point $(0, 0)$ which is related by mapping. However, we do not truncate at the points $(1, 0)$ or $(-1, 0)$ which slightly distorts the symmetry, and breaks the $\eta \mapsto 1 - \eta$ symmetry of the region we solve on. This can be seen in the plots we show in the following section, and we hope to correct this in the near future. It should be noted though that this will not fully correct the underlying problem of the asymmetry of the square centred state. Bearing these small caveats in mind, we are now ready to present some of the vibrational wavefunctions calculated from this potential, which we do in the next section.

4.12.1 Results

In Figures 4.39 and 4.40 we present the vibrational wavefunctions for the first three states in the trivial and sign representations, and the first state in each representation with opposite parity. In returning to plotting wavefunctions, we revert to the colouring scheme for wavefunctions from Figure 4.28. If one compares these pictures to the analogous pictures that we found for the old potential in Figures 4.29 and 4.30, one immediately see two things. Firstly, the new states are all qualitatively comparable to the old versions in terms of the number of peaks and their approximate positions. Secondly, we see that as we conjectured our new states are not symmetric under $\eta \mapsto 1 - \eta$, due to the asymmetric nature of our new potential breaking the symmetry of the states. This symmetry breaking is only slightly noticeable for low energy states, but becomes much more obvious for the higher energy states.

In Figures 4.41 and 4.42 we display the first two standard representation vibrational wavefunctions $u \pm w$ with positive parity. An immediate observation here is that we do not display the third such wavefunction as in Figures 4.31 and 4.32, because for our new potential this state does not exist. This is one very clear difference between the original potential and our new choice. Otherwise, these states appear to be quite similar, and since these states were not symmetric under $\eta \mapsto 1 - \eta$ in the original case, the effect of the symmetry breaking is less obvious.

Finally, in Figures 4.43 and 4.44 we display the first three standard representation vibrational wavefunctions $u \pm w$ with negative parity. Here we find

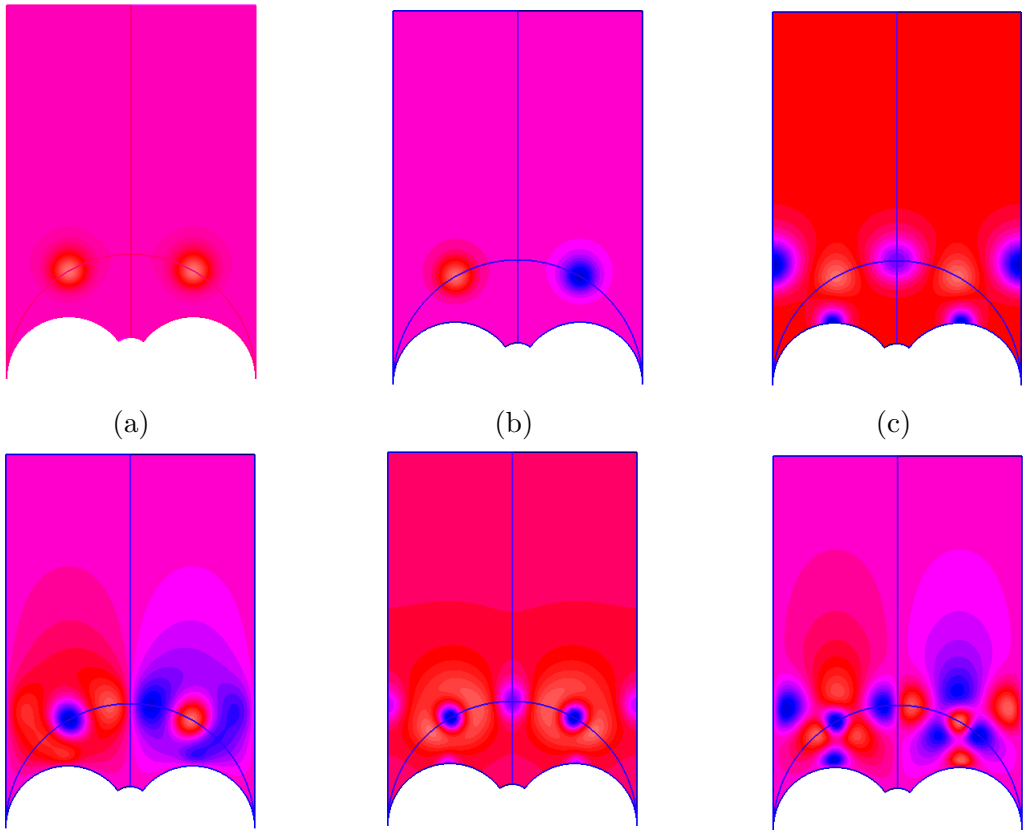

Figure 4.39: Plots for the trivial (left) and sign (right) vibrational wavefunctions for the new potential from Figure 4.38, in order of excitation.

(a) (b)

Figure 4.40: Plots for the trivial (left) and sign (right) opposite parity vibrational wavefunctions for the new potential from Figure 4.38.

(a) (b)

Figure 4.41: Plots for the first two standard representation wavefunctions $u + w$ with positive parity for the new potential from Figure 4.38.

(a) (b)

Figure 4.42: Plots for the first two standard representation wavefunctions $u - w$ with positive parity for the new potential from Figure 4.38.

that all three of the states analogous to the original ones found in Figures 4.33 and 4.34 do exist, and are again qualitatively similar.

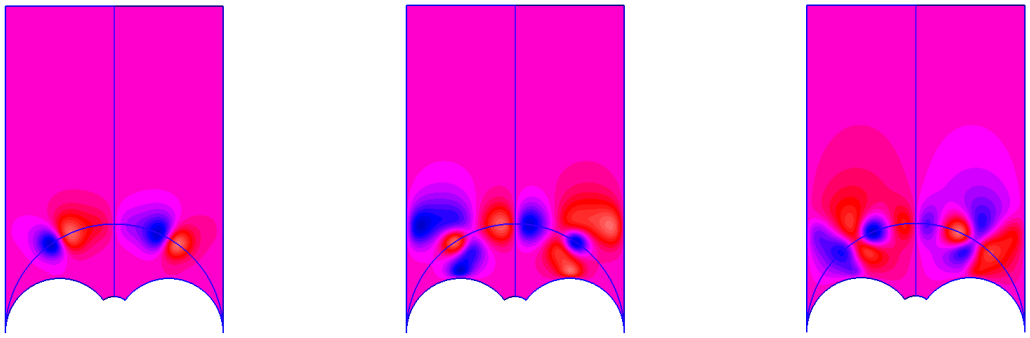

(a) (b) (c)

Figure 4.43: Plots for the first three standard representation wavefunctions $u + w$ with negative parity for the new potential from Figure 4.38.

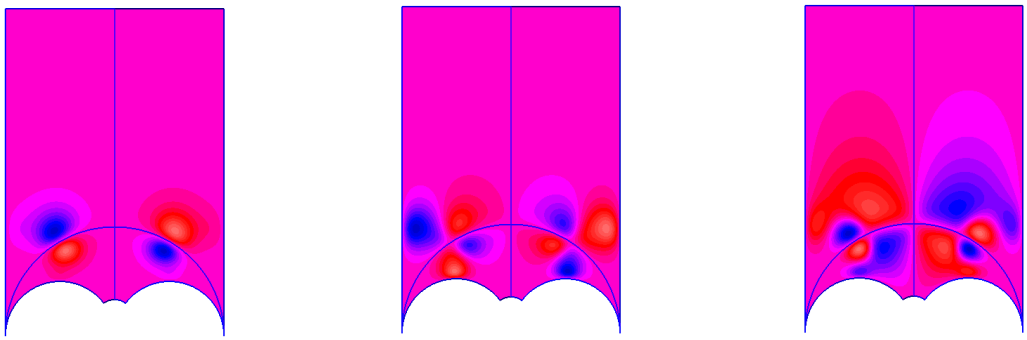

(a) (b) (c)

Figure 4.44: Plots for the first three standard representation wavefunctions $u - w$ with negative parity for the new potential from Figure 4.38.

4.12.2 Spectrum

We now want to produce a new energy spectrum based on the vibrational energies we have calculated for these new states. We do this using the same process for calibration as previously, and the resulting spectrum is displayed in Figure 4.45.

4.13 Discussion and outlook

We recall that the primary failing of the original potential (4.28, was the significant overstatement of the energy of the 0^- state. We previously calculated an energy for this state of 16.90 MeV compared to the experimental value of 10.96 MeV, an error of approximately 54%. Our new prediction for the energy of this state is 12.95 MeV which is still too large, but the error is now reduced to approximately 18% which represents a considerable improve-

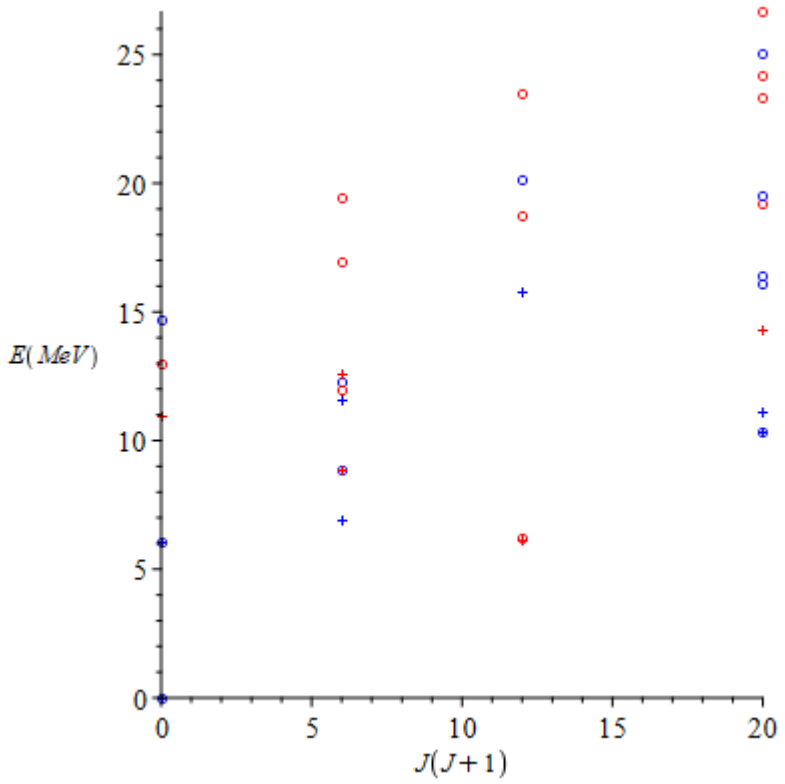

Figure 4.45: The spectrum calculated for Oxygen-16 for the new potential from Figure 4.38. As before, blue symbols denotes positive parity states and red symbols denote negative parity states. Circles denote states predicted by our model and crosses denote experimental energy values where they are known.

ment. We do notice however, that the energies of the two lowest lying spin-2 states are less well produced than before. These two states were previously produced to within less than 0.5 MeV of the experimental value, but now the energy of the 2^+ and 2^- states are out by approximately 2 MeV and 3 MeV respectively. For spin-3, the low-lying 3^- state is now extremely accurately produced (to within less than 0.1 MeV), although this was reasonably well produced before in any case. For spin-4 we recall that the lowest-lying state is fixed by our calibration, and we still do not accurately produce the first excited 4^+ state very well. This should have a similar energy to the lowest lying 4^+ state, with an energy difference of less than 1 MeV, but in our case (for both the original potential and this new one) there is a gap of several MeV. We also see that the ground state vibrational band is again well produced.

Overall, the use of this new potential has yielded some interesting results. In particular the improvement of the 0^- state energy, whilst not entirely corrected, is encouraging. It gives us reason to believe that if one experiments further with the parameters (c_0, c_1 and c_2) in our potential we may be able to fix this state still more precisely. However, it may be the case that in calibrating our parameters to describe this state, we distort the energies of other states such as the low-lying spin-2 states. A full parameter analysis of this potential to find the best possible match is something that we hope to do in the future. One could also consider including additional free parameters in the definition of the potential, which should allow more states to be fitted

exactly to experiment. However, whether this improves predictions for any remaining states is unclear, and we would like to keep our model as simple as possible.

Finally, we must again remark on the asymmetric nature of our constructed potential. Ideally, this is clearly something that should be addressed, and we will continue to investigate ways of enforcing the $\eta \mapsto 1-\eta$ symmetry that we desire. The natural way to do this is to take the potential (4.63) we defined previously and symmetrise it by hand. That is to say if we call the potential (4.63) $V(\eta, \epsilon)$, then we can define a symmetrised potential $\tilde{V}(\eta, \epsilon)$ by changing variables such that

$$\tilde{V}(\eta, \epsilon) = V(1 - \eta, \epsilon) \tag{4.64}$$

for $\eta \geq 0$, and

$$\tilde{V}(\eta, \epsilon) = V(-1 - \eta, \epsilon) \tag{4.65}$$

for $\eta < 0$. The new potential $\tilde{V}(\eta, \epsilon)$ will then be symmetric in the region from $\eta = 0$ to $\eta = 1$ about the vertical line $\eta = 1/2$, and also symmetric in the region from $\eta = -1$ to $\eta = 0$ about the line $\eta = -1/2$. It will also be continuous and smooth across the line $\eta = 0$, by construction.

Unfortunately, due to the way in which the code in FreeFEM++ is set up, this idea has proven to be more challenging to implement than one might imagine. This is due to the fact that the eigenfunctions that we use to construct the potentials are stored as arrays rather than defined as functions,

so performing a change of variables is not straightforward, and this idea is left open to the interested reader.

Another alternative idea is not to use eigenfunctions at all, but to attempt to construct a new potential from scratch that has the desired properties. It may be possible to do this by choosing rational functions with the correct minima, but this will require additional thought and we do not go into the details of this approach here.

Chapter 5

A quantum graph approach for Oxygen-16

5.1 Introducing the idea

A novel idea in the field of Skyrmion quantisation comes from a novel recent paper by Rawlinson [58]. The idea is to restrict the Skyrmion to some manifold as we have been doing up to now, but to then consider only certain key lines on the manifold. This means that we consider only certain key deformations. Making this restriction leads to a restricted configuration space which has the structure of a quantum graph, and quantum graph theory is used in the construction of solutions. The paper [58] offers promising results, improving on the Carbon-12 spectrum predicted by rigid body quantisation in the Skyrme model by allowing states which are superpositions of various key

configurations such as the triangle and linear chain. The paper also predicts several new states not previously seen in the Skyrme model for Carbon-12.

An advantage of this method is that by solving the Schrödinger equation only on certain key lines of the manifold, we reduce the problem to a series of one-dimensional problems. That is to say, we have to solve relatively simple ODEs with standard endpoint boundary conditions. This drastically simplifies the numerical work involved, although at the cost of losing some information about what happens away from the lines we consider.

We can quite easily conceive of a similar idea for Oxygen-16. We already have the necessary manifold, which remains the six-punctured sphere with constant negative curvature as before. We also already know some key lines on the manifold. If we recall Figure 4.2, we marked on the manifold a solid black line representing one of the scattering modes visualised in Figure 4.1. We also remarked that there are in fact three such modes, corresponding to lines passing through the three pairs of opposing faces of the tetrahedron. We can mark all of these modes on a single copy of the region F, which we do in Figure 5.1. The three scattering lines shown in Figure 5.1 are all related by symmetry, and we expect that the Schrödinger equation we must solve will be the same on each line. We also note that the three lines intersect at the two tetrahedral configurations, which leads us to the quantum graph structure shown in Figure 5.2. The graph contains fundamental nodes at the two tetrahedra and three removable nodes at the square configurations. The edges of the quantum graph are the scattering lines. The idea

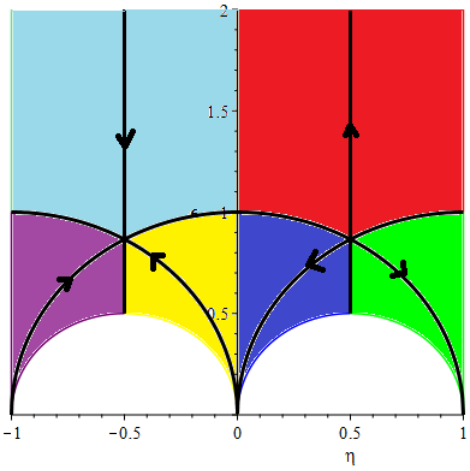

Figure 5.1: A plot of the region F with the three scattering modes clearly marked.

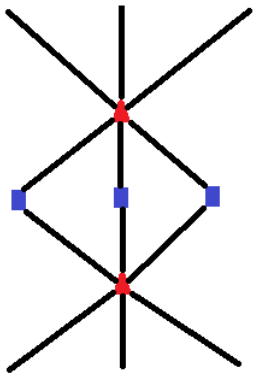

Figure 5.2: A display of the quantum graph structure obtained from considering the three scattering lines in F.

is to solve the Schrödinger equation on this graph. Since the three lines are related by symmetry, it will be enough to solve the Schrödinger equation on one of the lines, subject to boundary conditions that ensure matching at the tetrahedral notes and the condition that the solutions should vanish at infinity. The usual matching conditions in quantum graph theory are known as Kirchhoff conditions [59], [40]. These conditions require that the solutions be continuous across the nodes of the graph and that the sum of derivatives of solutions entering the node is equal to the sum of derivatives of solutions exiting the node. In our case, for the two fundamental nodes we have three edges entering each node and three edges leaving it. Therefore if we denote a coordinate on our graph by s and solutions on the three incoming nodes by $f_i(s)$ and solutions on the outgoing nodes by $g_i(s)$, the Kirchhoff condition [14], [13] states that

$$\sum_{i=1}^{i=3} \frac{df_i}{ds} = \sum_{i=1}^{i=3} \frac{dg_i}{ds}. \tag{5.1}$$

Notice that this condition does not necessarily imply that the incoming and outgoing derivatives of one particular solution must match, but for reasons of symmetry it will turn out that they do, at least in the trivial and sign representations. In fact it will turn out that for the case of the trivial and sign representations the quantum graph can be separated into three separate lines, as shown in Figure 5.3. These lines will each have the same Schrödinger equation and the same boundary conditions, and it will be sufficient to just consider one such line. For the standard representation this separation cannot

be made as the wavefunction may take a different function of u, v and w on each of the three lines so we must consider the full graph in this case, and be careful with the boundary conditions. For the trivial and sign representations

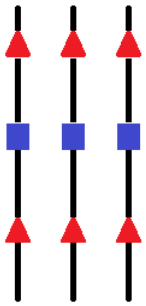

Figure 5.3: The separated quantum graph for the trivial and sign representations.

the problem is now relatively simple. We write down the usual Schrödinger equation on our graph

$$\frac{-\hbar^2}{2}\frac{d^2\phi}{ds^2} + V(s)\phi = E\phi, \tag{5.2}$$

where ϕ is the vibrational wavefunction as before. Again we see that we no longer have to worry about separability as the problem is now a one-dimensional one, so we can choose a more general potential if we want to. For the separated trivial and sign representation cases, there are no fundamental nodes at which we need to impose Kirchhoff conditions, so the only boundary conditions we need are the usual ones at infinity, namely

$$\phi(\pm\infty) = 0 \text{ and } \frac{d\phi}{ds}|_{\pm\infty} = 0. \tag{5.3}$$

The problem is now a simple second order ODE with standard endpoint boundary conditions, which can easily be solved numerically as long as the potential is a sensible function.

One final subtlety that should be mentioned is that in order to fully ensure that the three separated lines are fully equivalent we will parametrise each of them by arc length. As an example consider the straight line (we consider the right hand portion of this line). Let us parametrise it first as $(\eta, \epsilon) = (1/2, t)$, with $t = 1/2 \ldots \infty$. This is a perfectly valid parametrisation in its own right but now we attempt to rewrite this in terms of an arc length parameter s. We would also like the parametrisation to be such that the point $s = 0$ is the position of the square configuration, as the square sits at the centre of each of the scattering lines. We calculate the arc velocity on our line. Using the equation (4.3) for the hyperbolic metric, we can deduce that the arc velocity is given by

$$v(t) = \frac{\sqrt{\dfrac{d^2\eta}{dt^2} + \dfrac{d^2\epsilon}{dt^2}}}{\epsilon(t)}. \tag{5.4}$$

For our particular parametrisation this simplifies to $v(t) = 1/t$. We then calculate s by integrating over the velocity

$$s = \int_{t_0}^{t} v(\tau) d\tau. \tag{5.5}$$

In our case we want $s = 0$ to be the square so we take $t_0 = 1/2$ as that is the

position of the square in t coordinates. Performing the integral we find that

$$s = \ln(2) + \ln(t), \tag{5.6}$$

or rearranging

$$t = \frac{e^s}{2}. \tag{5.7}$$

Therefore an arc length parametrisation of the line is

$$(\eta, \epsilon) = (1/2, e^s/2) \tag{5.8}$$

for $s = 0 \ldots \infty$. Note for negative s we need to consider the left straight line and the parametrisation is symmetric. This parametrisation means that the position of the tetrahedron is at the point $\log(3)/2 \approx 0.55$.

So far we have discussed only the trivial and sign representation states, which are relatively straightforward as the graph separates into three single lines. To consider the standard representation is somewhat more involved, as this simple separation does not occur. The problem can still be broken down somewhat from the most general version of the graph in Figure 5.2, by a simple consideration of parity. Specifically, we know that the top and bottom halves of the graph are related by parity. We therefore need only solve the problem on one half of the graph (we will take the top half), which we show in Figure 5.4. We see that this new graph now has only one fundamental node, at the tetrahedron.

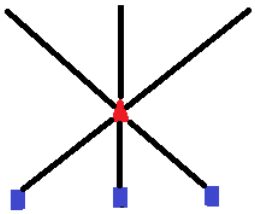

Figure 5.4: The further reduced quantum graph, which now consists of only one fundamental node.

We also know the boundary conditions at all of the end points of the graph. At the three upper end points, which correspond to infinity, we must have the condition that the wavefunction vanishes. At the three lower end points, which are at the square configuration, the boundary condition will depend on parity, but will be either that the wavefunction or its derivative must vanish. Let us now say that a wavefunction on one of the upper branches of the graph is denoted by ψ and a wavefunction on one of the lower branches is denoted by ϕ. We must thus have on all three branches that $\psi(\infty) = 0$ and either $\phi(0) = 0$ or $\phi'(0) = 0$ depending on parity, where we take $s = 0$ to be the position of the square as before. Imposing the continuity condition, we must have that

$$a_1\psi(t) = a_2\psi(t) = a_3\psi(t) = b_1\phi(t) = b_2\phi(t) = b_3\phi(t), \tag{5.9}$$

where t denotes the position of the tetrahedron. Also, we have the Kirchhoff

condition for derivatives, which gives

$$a_1\psi'(t) + a_2\psi'(t) + a_3\psi'(t) = b_1\phi'(t) + b_2\phi'(t) + b_3\phi'(t). \tag{5.10}$$

One solution of this is if we have $a_1 = a_2 = a_3 = a$ and $b_1 = b_2 = b_3 = b$, with a and b then related by $a\psi(t) = b\phi(t)$ and $a\psi'(t) = b\phi'(t)$. In practice, this means we can identify ψ and ϕ and the graph can be separated out into the three lines we saw before. This set of solutions will thus yield the trivial and sign representation states, depending on parity.

However, (5.9) and (5.10) also admit another kind of non-trivial solution, specifically if one of $\psi(t)$ or $\phi(t)$ is equal to zero (obviously if both are zero then we have the trivial solution). Suppose that $\psi(t) = 0$ and $\phi(t) \neq 0$, then from (5.9) we must have $b_1 = b_2 = b_3 = 0$. We also have the Kirchhoff condition (5.10), which now tells us that

$$a_1\psi'(t) + a_2\psi'(t) + a_3\psi'(t) = 0, \tag{5.11}$$

which implies $a_1 + a_2 + a_3 = 0$. This equation has a two-dimensional solution space. We now recall that in the standard representation we expect to find two solutions with degenerate energies, such as $u + v$ and $u - v$ or $u + w$ and $u - w$. One way to obtain a degenerate pair of solutions from the two-dimensional solution space is to take $a_1 = \pm a_2$ and a_3 fixed accordingly to satisfy the conditions.

Alternatively, we could have considered the case $\phi(t) = 0$ with $\psi(t) \neq$

0. Then by the same arguments, we would have $a_1 = a_2 = a_3 = 0$ and $b_1 + b_2 + b_3 = 0$. This yields the degenerate solutions $b_1 = \pm b_2$ with b_3 fixed. These solutions will again be degenerate, but will have different energy to the two solutions corresponding to $\psi(t) = 0$. These solutions thus represent standard representation states with a different vibrational wavefunction.

If we consider this second case, since $a_1 = a_2 = a_3 = 0$, the lower half of the graph is the only non-trivial part, and so we solve on only that part of the graph. This means we must impose boundary conditions at the square (these are fixed by parity to be $\phi'(0) = 0$ for positive parity or $\phi(0) = 0$ for negative parity, as outlined previously) and at the tetrahedron. Note that previously we did not impose a boundary condition at the tetrahedron but now we must do so. We can consider either the case $\phi(t) = 0$ or $\phi'(t) = 0$, with the first case giving rise to states that vanish at the tetrahedron and the second case giving rise to states that are maximal at the tetrahedron.

We could also consider the first case where $b_1 = b_2 = b_3 = 0$, and the non-trivial part of the graph is the top part, and construct solutions in this way. Then we have to impose boundary conditions at the tetrahedron and at infinity. Obviously at infinity we must have $\psi(\infty) = 0$, and again at the tetrahedron we can consider either the case $\psi(t) = 0$ or $\psi'(t) = 0$, such that the wavefunction either vanishes or is maximal at the tetrahedron. In this case however, it is not clear how to impose parity, as we normally do this by fixing the boundary condition at the square, which we cannot do here.

5.2 A proof of concept

Once again we will use the potential (4.28) as a proof of concept. We now present some solutions of (5.3) subject to (5.2) with potential (4.28). We first must point out that there are certain states which are not susceptible to study via this approach. Specifically, these states are ones which are forced to be zero on all of the quantum graph lines due to boundary conditions. In particular these states are states with negative parity in the trivial representation and states with positive parity in the sign representation. It also includes certain combinations of u, v and w in the standard representation, but not either of the combinations $u+w$ or $u-w$ with either parity, which are the combinations we are interested in. We can however apply the quantum graph method to all of the other states, and at this stage we are interested in seeing how well the quantum graph method approximates the full solutions which we have calculated previously. Clearly, we expect that some information is lost, and this is particularly true for higher excited states where a higher proportion of the wavefunctions are concentrated away from the scattering lines. However for the low energy states, such as the ground state, the quantum graph would be expected to give a good approximation.

5.2.1 Results

We now present some results where we plot a cross-section of the full two-dimensional solution on one of the scattering lines and compare it with the

quantum graph solution. For the full two-dimensional solution we plot a thickened profile which represents the solution on a tube of thickness 0.2 centred on the line $\eta = 1/2$. We do this as it gives us an average value of the profile on this line, and for the higher excited states taking this thickened tube allows us to capture some of the off line excitations which we would otherwise miss.

We now display the solutions in Figure 5.5. We use a Matlab fitting algorithm to attach a scalar multiplier to the quantum graph solution that gives the best fit to the full two-dimensional tube solution. As we shall see from the resulting figures, the fit is quite good for lower energy states but breaks down for higher excited states and we shall discuss reasons for this later, along with other aspects of the results. We also display in Table 5.1 values of the calibrated vibrational energies for the states in the quantum graph picture compared to the full two-dimensional situation.

It will be noted that have not given plots for any standard representation states in the quantum graph picture, as these have not yet been produced. We do however give energies for the three standard representation states of each parity in Table 5.1. These energies were calculated on the lower part of the graph from Figure 5.4, that is to say the case with $a_1 = a_2 = a_3 = 0$. One can also calculate solutions with $b_1 = b_2 = b_3 = 0$, but since it is not clear how to define parity in this case we do not consider these here. It can be seen that the first states of each parity (labelled (i) and (l)) match up quite well with the calculated vibrational energies, and the second and third

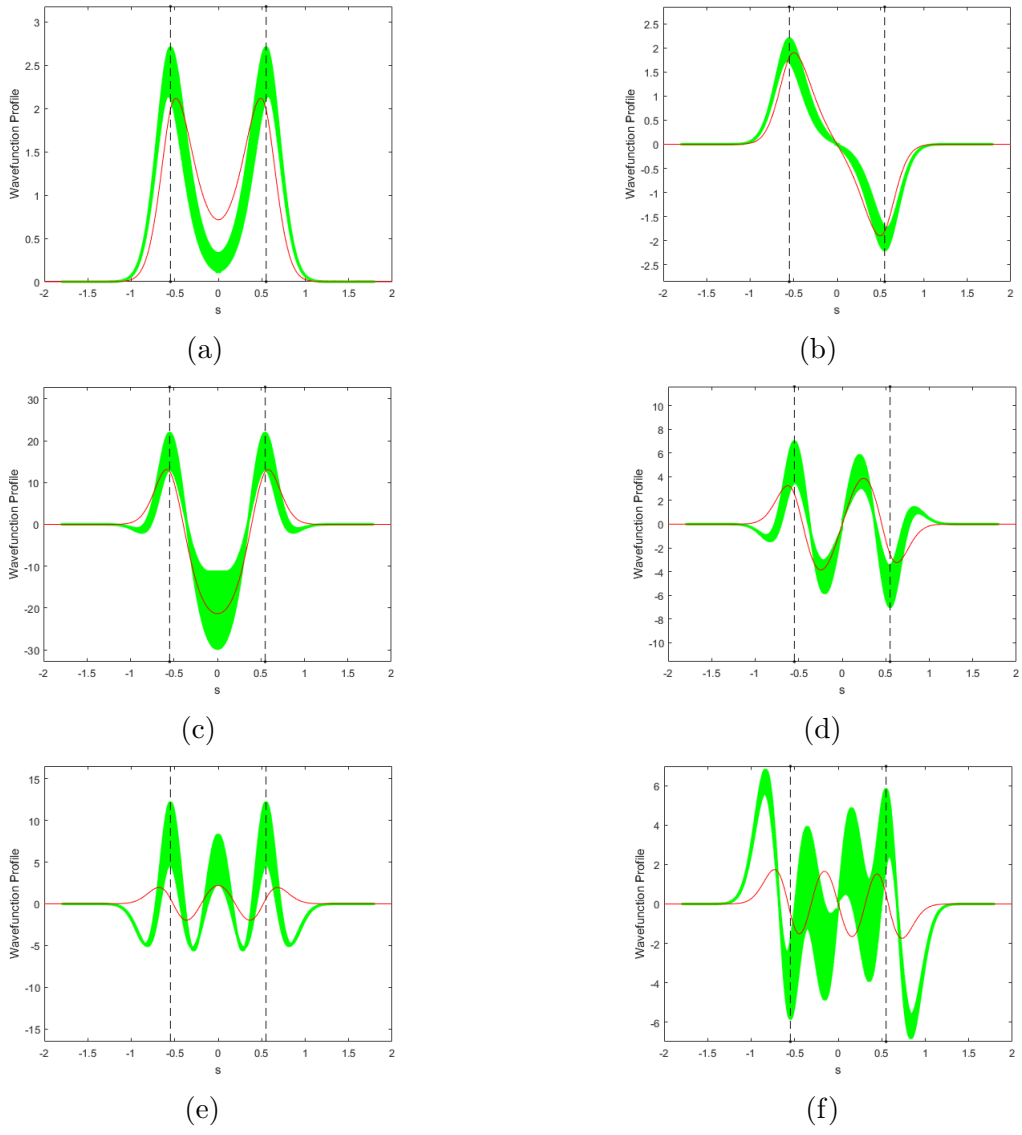

Figure 5.5: Plots for the quantum graph solutions, again with trivial states on the left and sign states on the right. The profile solution of the full solution is in green and the quantum graph solution is in red. The dashed black line denotes the position of the tetrahedron where we do not specifically impose a boundary condition.

Vibrational State	Full Solution Energy	Quantum Graph Energy
(a)	0	0
(b)	6.05	6.05
(c)	14.52	14.99
(e)	0.07	0.28
(f)	9.56	9.77
(g)	17.85	20.43
(i)	4.15	3.59
(j)	8.83	6.72
(k)	12.83	13.13
(l)	5.32	5.98
(m)	11.55	12.87
(n)	16.24	22.70

Table 5.1: A table comparing the vibrational energies of states using the quantum graph and full two-dimensional methods.

states are plausible. However, the energy of the third negative parity state (n) is considerably off.

5.2.2 Discussion

We see the results are roughly in line with what we expect. For the ground state and the first state in the sign representation we see that the quantum graph solution is qualitatively the same as the cross-section of the full solution. Then for the first excited states in each representation we see that the solutions look qualitatively similar near to the squares and tetrahedra, but asymptotically the quantum graph does not quite capture the behaviour of the full solutions. Then for the second excited states in each representation we see that the graph solutions match up much less well with their

two-dimensional counterparts. In terms of the energies we observe that there is good agreement between the quantum graph and the full solutions. Recalling that the exact matching for states (a) and (b) comes from the way in which we calibrate the vibrational energies, we see that for states (c), (e) and (f) the matching is very good and for state (g) the energy is at least in the correct neighbourhood. Overall we can conclude that the quantum graph description works very well for the lower energy states and only moderately well for the higher excited states, whilst we also recall that there are some states ((d) and (h)) for which the method does not work at all. For the standard representation we see a similar pattern, where the energies of the lower energy states match well, but are further out for the higher energy states, most notably state (n). We would like to produce some plots for standard representation states in the quantum graph picture, for comparison with the full states calculated in Chapter 4, and this will be a task for future work.

5.3 Other potentials

In addition to the fact that the numerical work is considerably simplified, a further advantage of the quantum graph method is that because it automatically gives us an ODE rather than a PDE to solve we no longer have to worry about separability. As such, we are free to choose more general potentials, as in our two-dimensional numerical work. However, we know that the original potential (4.28) produced the Oxygen-16 very well with the exception of the

0^- state. Therefore any change of potential would be motivated by wanting to correct this inaccuracy. Unfortunately, the 0^- state is one of the states which is not susceptible to analysis by the quantum graph method as it is identically zero on all relevant lines due to boundary conditions. Therefore, there is probably limited value in considering alternative potentials in the quantum graph framework, and we do not do so here.

Chapter 6

Carbon-12 and the three-punctured sphere

We now briefly discuss the prospect of using the same framework as we have been using for Oxygen-16 to quantise other Skyrmions. In particular, we could plausibly think about considering any Skyrmion with baryon number equal to a multiple of four. One possibility that turns out to be particularly relevant is that of Carbon-12, because in this case not only can we use essentially the same method as for Oxygen-16, but we can also make a very highly related choice of manifold as we shall outline shortly. First, let us remember that the $B = 12$ Skyrmion has two minimal energy configurations that are roughly equal in energy, namely the triangle and the linear chain that we saw in Figure 1.2. Physically, it is known that the triangle configuration should be the minimal energy configuration, and the linear chain, also known as

the Hoyle state, is an early excited state [69]. We will use this as the basis for our upcoming proposal. Whereas in the case of Oxygen-16 we had the global minimum of our potential situated at the tetrahedra with higher local minima at the squares, now we will want to have a global minimum at the triangle and a higher local minimum at the chain.

Recall that for Oxygen-16 we chose as our manifold the six-punctured sphere with constant negative curvature. We chose this since this manifold had three symmetry axes stretching out to infinity in each direction, corresponding to the three symmetry axes of the tetrahedral configuration. In the case of Carbon-12, we can instead choose the three-punctured sphere. We colour the region in the same way that we did before, and now we consider the points where three colours meet to be the position of the triangle configurations and the points where two colours meet to be the position of the chain configurations. The points at infinity now represent when the Carbon-12 nucleus has separated into an alpha particle and a pair of alpha particles. Note that there is a slight distinction in how we think about our manifold between the Oxygen-16 and Carbon-12 cases. For Carbon-12, we do not think in terms of scattering modes, but rather we think of the points on the sphere as shapes of triangles (corresponding to the location of the three alpha particles) and the three punctures are when two alpha particles lie on top of each other.

Although the punctures on the 3-punctured sphere are in different places compared to the 6-punctured sphere, the projection of the manifold onto the

complex plane will in fact look like exactly one half of the 6-punctured sphere [18]. We will also consider the projection not onto the complex upper half-plane as before, but rather on to the Poincaré disk, as we want to think in terms of triangles and the Poincaré disk makes this more obvious. In order to fully realise this, we must consider the consequences of projecting our surface onto the Poincaré disk rather than the plane as before. The mapping to go between the complex plane and the Poincaré disk is well known, and the formulae for taking a point (η, ϵ) from the plane to the disk and the disk to the plane respectively are given by

$$(\eta, \epsilon) \to \left(\frac{2\eta}{\eta^2 + (1+\epsilon)^2}, \frac{\eta^2 + \epsilon^2 - 1}{\eta^2 + (1+\epsilon)^2} \right) \tag{6.1}$$

and

$$(\eta, \epsilon) \to \left(\frac{2\eta}{\eta^2 + (1-\epsilon)^2}, \frac{1 - (\eta^2 + \epsilon^2}{\eta^2 + (1-\epsilon)^2} \right). \tag{6.2}$$

The metric on the disk is also different to the metric on the plane. For the plane the metric is $ds^2 = (d\eta^2 + d\epsilon^2)/\epsilon^2$ which gives rise to the prefactor of ϵ^2 in the operator (4.4). For the disk the metric is $ds^2 = 4(d\eta^2 + d\epsilon^2)/(1 - (\eta^2 + \epsilon^2))^2$. This changes the form of the operator so that we now have

$$-\Delta_{\text{vib}} = -\left(\frac{1 - (\eta^2 + \epsilon^2)^2}{4} \right) \left(\frac{\partial^2}{\partial \eta^2} + \frac{\partial^2}{\partial \epsilon^2} \right). \tag{6.3}$$

Lastly the boundary curves that we defined for our red region will be different once it has been mapped to the Poincaré disk. It turns out if we apply the

coordinate transformation above our region is now bounded by the curves $\eta = 0$, $\epsilon = 0$, $\epsilon = 1 - \sqrt{\eta(2-\eta)}$ and $\epsilon = -1 + \sqrt{\eta(4-\eta)}$. Again this is two straight lines and two arcs of circles, as we had before.

6.1 The three-punctured sphere as a vibrational manifold

In Figure 6.1 we display the projection onto the complex upper half-plane of the full three-punctured sphere and the quarter of the three-punctured sphere that will be analogous to the region F we considered for Oxygen-16. We also display the same region projected on to the Poincaré disk in Figure 6.2.

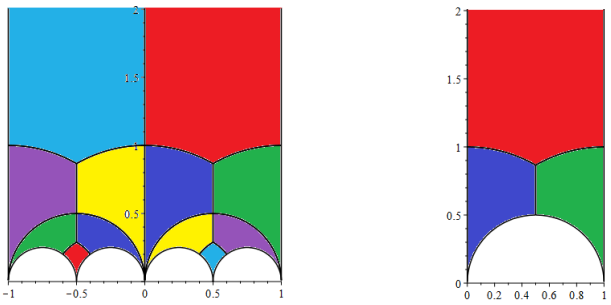

(a) (b)

Figure 6.1: Plots of the projection of the full three-punctured sphere onto the complex upper half-plane (left) and the projection of one quarter of the surface (right).

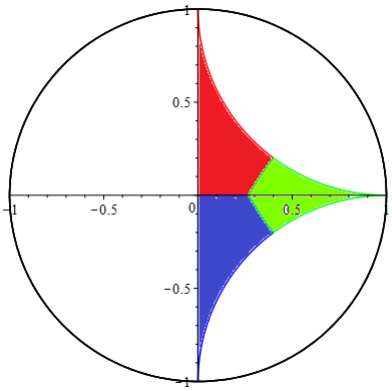

Figure 6.2: A plot of the quarter of the three-punctured sphere from Figure 6.1b, but now displayed on the Poincaré disk.

6.2 The shape space of triangles

As alluded to previously, we want to think about Carbon-12 in terms of triangles. That is to say, we consider the three alpha particles making up Carbon-12 as the vertices of a triangle. The minimal energy configuration is where this triangle is equilateral, and we can even think of the linear chain as a triangle where the obtuse angle has opened out to 180 degrees. The paper [34] discusses the theory of the shape space of triangles, and for a full discussion the reader is referred there. An interesting analogy with Oxygen-16 is to imagine that you are located on one of the four alpha-particles making up the Oxygen-16 configuration, and looking out at the other three particles. If you are at the tetrahedron (the minimum for Oxygen-16) you will see the equilateral triangle, and if you are at the square you will see the linear chain. As we expect based on our colouring, there is a clear analogy

between the tetrahedron and triangle configurations and between the square and chain configurations. As one transitions between the triangle and the chain there are many isosceles triangle configurations. Another interesting point to observe is that one can clearly see the quantum graph from [58] in Figure 6.2. One has the equilateral triangle at the central point where three colours meet and the linear chain at the centres of the three edges. A subtle point is that as in the quantum graph from [58], the three linear chains are slightly different. If one labels the three alpha particles, say 1, 2 and 3, then the three chains each have a differently labelled alpha particle as the central particle in the chain. In fact, the particles are identical so this makes no practical difference, but it is a subtlety that is worth mentioning, in order to connect with [58]. Whilst the shape space described in [34] is very natural to describe the triangle, it is somewhat harder to claim that the continued use of the hyperbolic metric is justified. It remains the most mathematically natural choice to make, but there are no natural scattering trajectories as for Oxygen-16 so this choice of metric has less physical relevance. It may be interesting to consider equipping the 3-punctured sphere with alternative metrics in the future, but we will continue to work with the hyperbolic metric here as a matter of convenience.

6.3 Symmetries and boundary conditions

We must think about how the symmetries and boundary conditions that we established for Oxygen-16 on the 6-punctured sphere can be translated to the 3-punctured sphere for Carbon-12. Our manifold has many of the same symmetry properties as the 6-punctured sphere, in regard to the mappings we can use to map between the different coloured regions. Since the different representations into which our solutions fell for the Oxygen-16 problem were related to the S_3 symmetry, the fact that our 3-punctured sphere has the same symmetries will mean that the vibrational wavefunctions for Carbon-12 will fall into the same three representations. The way in which the symmetry conditions will work in the three representations must be considered. In the trivial representation, the rotations that map between the different coloured regions will work in exactly the same way as for the Oxygen-16 case, but for the sign and standard representations we must be slightly more careful and it will be necessary to give extra consideration to how the rotations act. Note that as one moves along one of the boundaries between the coloured regions, one moves from the tetrahedron to the square. These lines correspond to isosceles triangles which have a natural C_2 symmetry, mapping the two equivalent corners into each other and keeping the remaining corner fixed. The trivial representation transforms trivially under this symmetry, whereas the sign representation picks up a factor of minus one and the effect on a standard representation wavefunction will depend on precisely which wave-

function is considered. The main difficulty is that although there is clearly a natural action of S_3 on the space of triangles, simply by exchanging labelled vertices, this does not give rise to an obvious action of rotations. This will need some additional thought in order to take this idea further.

Recall also that for Oxygen-16 our boundary conditions were derived from parity and the various Möbius transformations relating the coloured regions of F. Since these mappings are the same, the boundary conditions for Carbon-12 states of a particular representation and parity will correspond to the same boundary conditions as for Oxygen-16.

A key difference will be in our choice of potential, which we will want to choose so as to produce the low-lying spectrum of Carbon-12. The structure of this potential may be relatively similar to Oxygen-6 potentials, but certainly some parameter values will change. We might consider the potential used in [58] as a good starting point.

6.4 Allowed spin states for Carbon-12

We can also ask ourselves what are the allowed states of a given spin and parity for Carbon-12. Rawlinson does this in [58], and determines the bases of allowed states for each J^P to be those that we show in Table 6.1.

In [58], Rawlinson uses the C_2 action $\exp(i\pi L_2)$ to represent swapping particles 2 and 3, and the action $\exp(i\pi L_3)$ to represent parity. In particular, he argues that all wavefunctions should be invariant under S_3, which means

J^P	Basis	J^P	Basis
0^+	$\|0,0\rangle$	0^-	
1^+		1^-	$\|1,1\rangle + \|1,-1\rangle$
2^+	$\|2,2\rangle + \|2,-2\rangle$ $\|2,0\rangle$	2^-	$\|2,1\rangle - \|2,-1\rangle$
3^+	$\|3,2\rangle - \|3,-2\rangle$	3^-	$\|3,3\rangle + \|3,-3\rangle$ $\|3,1\rangle + \|3,-1\rangle$
4^+	$\|4,4\rangle + \|4,-4\rangle$ $\|4,2\rangle + \|4,-2\rangle$ $\|4,0\rangle$	4^-	$\|4,3\rangle - \|4,-3\rangle$ $\|4,1\rangle - \|4,-1\rangle$
5^+	$\|5,4\rangle - \|5,-4\rangle$ $\|5,2\rangle - \|5,-2\rangle$	5^-	$\|5,5\rangle + \|5,-5\rangle$ $\|5,3\rangle + \|5,-3\rangle$ $\|5,1\rangle + \|5,-1\rangle$

Table 6.1: A table listing bases of allowed spin states for each J^P for Carbon-12.

they will be invariant under $\exp(i\pi L_2)$. The reason for this is that since the alpha particles are identical, all wavefunctions should be invariant under an exchange of alpha particles. This assumption means that in effect we need only consider the trivial representation, and this will still be enough to produce many states. Note also that this argument only works because alpha particles are bosons, and so invariant under relabelling due to boson exchange statistics. An alternative case to consider would be the Helium-3 nucleus, which we could think of as being composed of three $B = 1$ Skyrmions rather than three alpha particles. We could still use the three-punctured sphere and the shape space of triangles, but now since $B = 1$ Skyrmions are fermions, they would pick up a minus sign under relabelling due to fermion exchange statistics. That is, the wavefunctions would always pick up a minus sign

under S_3, so we could consider only the sign representation.

6.5 Outlook

The idea is to solve the Schrödinger equation, which takes the same form as before, but now with a potential that is more suitable for Carbon-12, with the aim of fitting the known experimental spectrum for Carbon-12 as successfully as possible. The process for doing this will employ the same methods as for Oxygen-16, with the aim again being to use two-dimensional numerics in order to allow a general choice of potential. Previous work done on Carbon-12 in the Skyrme model can be found in [43] and also in the paper [58] on quantum graphs, which motivated Chapter 5 of this thesis. The paper [43] gives a good understanding of the ground state and Hoyle state bands, as well as a good match to the known experimental value of the ratio of root mean square radii of the two states. However, a full vibrational quantisation of Carbon-12 has not yet been performed within the Skyrme model, and it is conceivable that such work could lead to the prediction of states not previously found in the Skyrme model. One point that is not clearly understood about the $B = 12$ Skyrmion is which of the triangle and chain configurations is actually the global minimum in the Skyrme model. In [43], the writers cite the energy of the triangular configuration as 1816 and the chain configuration as 1812 in Skyrme units, but with associated errors of up to 0.2%. This means that the energies are 1816 ± 3.6 and 1812 ± 3.6

respectively, so the ordering is unclear. Physically, it is understood that the triangle ought to be the global minimum, and we hope that a full vibrational quantisation may shed some light on this too. Another important point is that we wish to build on the quantum graph approximation seen in [58], by finding some states that may be missed. For example when we considered the quantum graph approximation for Oxygen-16 in Chapter 5, we found that two states were entirely missed, including the physically relevant 0^- state. We hope that this method may discover similar states that were missed by the quantum graph model for Carbon-12. We do not give results for Carbon-12 in this thesis, but leave this idea open for future work.

Chapter 7

Conclusion

7.1 Summary and discussion

In this thesis we have considered the vibrational quantisation of the Skyrme model. We began by discussing the limitations of rigid body quantisation, and moved on to consider recent work on vibrational quantisation [29], [30],[31]. We sought to generalise this method, which we have applied to the $B = 2$ and $B = 16$ Skyrmions in this thesis, as well as outlining a concept for how the method could be applied to $B = 12$. We argued that vibrational quantisation goes some way to resolving a fundamental problem of the Skyrme model, which is that the calculated binding energies of nuclei are too high. We saw that including vibrational modes contributes to the zero point energy of a Skyrmion, consequently lowering its binding energy.

In Chapter 3 we considered the $B = 2$ Skyrmion, with the aim of describ-

ing it as the deuteron. We sought to conduct a full vibrational analysis, and also included a pion mass term. This allowed us to go further than previous work done for the $B = 2$ sector, which conducted a limited vibrational analysis in the instanton approximation, for the case of massless pions [44]. We found in our model that the value of the binding energy of the deuteron, whilst still too large, was closer to the experimental value given in [16] than in previous models. We also came close to making the isospin-1 state an unbound state, as it is physically, and conjectured that for a slightly higher pion mass this may well occur. We left this open as a task for future work, along with the calculation of other physical observables of the deuteron such as its electric charge radius, which is well known experimentally [16]. It should be noted that this work was all done in the attractive channel configuration. This approximation could be improved by including more degrees of freedom, but obviously this would be numerically more challenging. Another open task would be to include the Coulomb interaction in the model, which would have the effect of making the proton-proton state less bound than the neutron-neutron state, and could be worth investigating. The incorporation of the Coulomb effect into the Skyrme model has not been widely investigated before, but is considered in [45]. There have been some attempts to gauge the Skyrme model, including the electromagnetic interaction, and some discussion of this can be found in [56].

We then considered the $B = 16$ Skyrmion in Chapter 4, with the physical nucleus we were seeking to describe there being Oxygen-16. We sought

to generalise some previous work done on vibrational quantisation for this sector. In particular we aimed to address a specific weakness of this work [30, 31], which was that the method used imposed severe restrictions on the choice of potential, meaning that the potential chosen was not particularly physical or related to the Skyrme model. It also had the undesirable feature of not being smooth everywhere. We were able to circumvent these issues by using a more involved two-dimensional numerical method to approach the problem. We checked that this method was robust by first considering the previously used potential with our new numerical method, and verified that our results were consistent. We then constructed a new potential with more desirable properties, specifically having minima at both of the minimal energy Skyrmion configurations, flattening off to a finite value at infinity, and being smooth everywhere. We found that the energy of the 0^- state was considerably improved compared to [30], although still slightly overstated compared to experiment [33]. We also found that for our particular parameter set, the energies of the two lowest lying spin-2 states were slightly adversely effected by our new potential. We conjectured that varying the parameters in order to precisely fix one state could have a detrimental effect on others, and that a task for future work was to run a full parameter sweep on our new potential to determine the best overall fit. Another point for future consideration in this problem is the metric. In [30], not only the potential, but also the metric term was restricted by the constraint that the equations had to be separable. Our method allows us to use any metric on the 6-punctured sphere. In

particular, one could attempt to calculate the induced metric directly from Skyrmion-Skyrmion scattering.

We next considered an alternative approach to the $B = 16$ sector in Chapter 5, using a quantum graph approach based on the work done in [58]. This idea is interesting because it considerably simplifies the vibrational quantisation problem, although it should be noted that the results are only an approximation, and information about certain states is entirely lost. However, the results are very promising for low-energy states. It is reasonable to say that the quantum graph approximation is a sensible one, and could be used in cases where a full numerical approach is too complicated to implement. We do however need to give a little more thought to how the standard representation states can be plotted in this picture. All that is required for the quantum graph method is the identification of a suitable vibrational manifold and certain key lines on it, so it may be possible to apply this technique to many other Skyrmion sectors.

Finally, in Chapter 6 we made some conjectures that the two-dimensional vibrational method that was applied for Oxygen-16 in Chapter 4 could also be applied to Carbon-12. We argued that a highly related manifold could be used that would have many similar symmetry properties meaning that, up to the choice of a different potential, the problem would be very similar and employ essentially the same numerical methods. We noted in Chapters 4 and 5 that the quantum graph method entirely misses certain states that are found using the full numerical method, such as the 0^- state in the case

of Oxygen-16. Our conjecture is that using the full numerical method for Carbon-12 may uncover some states that were missed by [58]. We left this idea open for future work.

7.2 Outlook

We are also in a position to consider some open questions that the work in this thesis generates for future consideration. One possibility is to apply the technique used for $B = 2$ in Chapter 3 to the $B = 8$ Skyrmion. In this case we would be considering the scattering of two $B = 4$ cubes rather than two single Skyrmions, but the approach and method would be similar. There is no stable nucleus with baryon number $B = 8$, and the $B = 8$ Skyrmion models the unstable Beryllium-8 nucleus, which decays into two α-particles. The Finkelstein-Rubinstein constraints here would mean that the ground state should have $J = 0$, $I = 0$, and it would be interesting to see whether vibrational quantisation predicts this to be a bound state or not.

The approaches considered for Oxygen-16 in Chapters 4 and 5 could also be applied to other Skyrmion sectors. In particular, a key feature of Oxygen-16 in our approach was that it has two minimal energy configurations with very similar energies, the tetrahedron and the square. As such, other Skyrmions that share this property could be susceptible to this idea. One possibility is the $B = 20$ Skyrmion that models Neon-20, which has two minimal energy configurations separated by a potential barrier [42]. It is not

completely obvious how to choose the scattering space, so this requires some thought, but is certainly an avenue for future exploration. Other possibilities include $B = 24$, which models Magnesium-24, and Helium-3. Helium-3 can be considered in much the same way as we discussed for Carbon-12 in Chapter-6, except we would need to consider three $B = 1$ Skyrmions rather than three α-particles. The three-punctured sphere could be used again, but with different Finkelstein-Rubinstein constraints.

One final idea is to combine vibrational quantization with generalised Skyrme models, with the additional features that we discussed in Chapters 1 and 2, such as BPS terms [1]. Efficient approximations, possibly based on quantum graphs, would be very useful to determine which parameters give the best match for the quantum states. All of the above ideas could be an interesting basis for future work.

Bibliography

[1] C. Adam, J. Sánchez-Guillén, and A. Wereszczyński. "A Skyrme-type proposal for baryonic matter". *Phys. Lett.* B691 (2010), 105.

[2] G. Adkins and C. Nappi. "The Skyrme model with pion masses". *Nucl. Phys.* B233 (1984), 109.

[3] G. Adkins, C. Nappi, and E. Witten. "Static properties of nucleons in the Skyrme model". *Nucl. Phys.* B228 (1983), 552.

[4] R. Battye, M. Haberichter, and S. Krusch. "Classically isospinning Skyrmion solutions". *Phys. Rev.* D90 (2014), 125035.

[5] R. Battye, S. Krusch, and P. Sutcliffe. "Spinning Skyrmions and the Skyrme parameters". *Phys. Lett.* B626 (2005), 120.

[6] R. Battye, N. Manton, P. Sutcliffe, and S. Wood. "Light nuclei of even mass number in the Skyrme model". *Phys. Rev.* C80 (2009), 034323.

[7] R. Battye and P. Sutcliffe. "A Skyrme lattice with hexagonal symmetry". *Phys. Lett.* B416 (1998), 385.

[8] R. Battye and P. Sutcliffe. "Skyrmions and the pion mass". *Nucl. Phys.* B705 (2005), 384.

[9] R. Battye and P. Sutcliffe. "Skyrmions, fullerenes and rational maps". *Rev. Math. Phys.* 14 (2002), 29.

[10] W. Bauhoff, H. Schultheis, and R. Schultheis. "Alpha cluster model and the spectrum of O16". *Phys. Rev.* C29 (1984), 1046.

[11] E. Braaten and L. Carson. "Deuteron as a soliton in the Skyrme model". *Phys. Rev. Lett.* 56 (1986), 1897.

[12] E. Braaten, S. Townsend, and L. Carson. "Novel structure of static multisoliton solutions in the Skyrme model". *Phys. Lett.* B235 (1990), 147.

[13] B. Brown, M. Langer, and K. Schmidt. "The HELP inequality on trees". *Proc. Symp. Pure. Math* 77 (2008).

[14] B. Brown and K. Schmidt. "On the HELP inequality for hill operators on trees". *Operator Theory: Advances and Applications* 219 (2012).

[15] E. Caurier, G. Martinez-Pinedo, F. Nowacki, A. Poves, and A. Zuker. "The shell model as a unified view of nuclear structure". *Rev. Mod. Phys.* 77 (2005), 427.

[16] T. Ericson. "The deuteron properties". *Nucl. Phys.* A416 (1984), 281.

[17] L. Fadeev. "Some comments on the many dimensional solitons". *Lett. Math. Phys.* 1 (1976), 289.

[18] H. Farkas and I. Kra. *Theta Constants, Riemann Surfaces and the Modular Group*. American Mathematical Society, 2001.

[19] D. Feist, P. Lau, and N. Manton. "Skyrmions up to baryon number 108". *Phys. Rev.* D87 (2013), 085034.

[20] D. Finkelstein and J. Rubinstein. "Connection between spin, statistics and kinks". *J. Math. Phys.* 9 (1968), 1762.

[21] D. Foster and S. Krusch. "Scattering of Skyrmions". *Nucl. Phys.* B897 (2015), 697.

[22] M. Gell-Mann, R. Oakes, and B. Renner. "Behaviour of current divergences under $SU(3) \times SU(3)$". *Phys. Rev.* 175 (1968), 2195.

[23] M. Gillard, D. Harland, E. Kirk, B. Maybee, and J. Speight. "A point particle model of lightly bound Skyrmions". *Nucl. Phys.* B917 (2017), 286.

[24] M. Gillard, D. Harland, and J. Speight. "Skyrmions with low binding energies". *Nucl. Phys.* B895 (2015), 272.

[25] D. Giulini. "On the possibility of spinorial quantisation in the Skyrme model". *Mod. Phys. Lett.* A8 (1993), 1917.

[26] S. Gudnason and C. Halcrow. "Vibrational modes of Skyrmions". *Phys. Rev.* D98 (2018), 125010.

[27] L. Hafstad and E. Teller. "The alpha-particle model of the nucleus". *Phys. Rev.* 54 (1938), 681.

[28] C. Halcrow. "Skyrmions - beyond rigid body quantisation". PhD thesis. Cambridge University, 2017.

[29] C. Halcrow. "Vibrational quantisation of the B=7 Skyrmion". *Nucl. Phys.* B904 (2016), 106.

[30] C. Halcrow, C. King, and N. Manton. "A dynamical α-cluster model of Oxygen-16". *Phys. Rev.* C95 (2017), 031303.

[31] C. Halcrow, C. King, and N. Manton. "Oxygen-16 spectrum from tetrahedral vibrations and their rotational excitations". *Int. J. Mod. Phys.* E28 (2019), 1950026.

[32] C. Houghton, N. Manton, and P. Sutcliffe. "Rational maps, monopoles and Skyrmions". *Nucl. Phys.* B510 (1998), 507.

[33] J. Kelley, D. Tilley, H. Weller, and C. Cheves. "Energy levels of light nuclei A=16-17." *Nucl. Phys.* A564 (1993), 1.

[34] D. Kendall. "A survey of the statistical theory of shape". *Stat. Sci.* 4 (1989), 87.

[35] C. King. "$B = 4N$ nuclei in the Skyrme model". PhD thesis. Cambridge University, 2019.

[36] S. Krusch. "Finkelstein-Rubinstein constraints for the Skyrme model with pion masses". *Proc. Roy. Soc. Lond.* A462 (2006), 2001.

[37] S. Krusch. "Homotopy of rational maps and the quantisation of Skyrmions". *Ann. Phys.* 304 (2003), 103.

[38] S. Krusch. "Quantisation of Skyrmions". *hep-th/0610176* (2006).

[39] S. Krusch and J. Speight. "Quantum lump dynamics on the two-sphere". *Commun. Math. Phys.* 322 (2013), 95.

[40] P. Kuchment. "Quantum graphs: an introduction and a brief survey". *Proc. Symp. Pure. Math.* 77 (2008).

[41] L. Landau and E. Lifshitz. *Mechanics*. Pergamon Press Limited, 1969.

[42] P. Lau and N. Manton. "Quantisation of T_d and O_h symmetric Skyrmions". *Phys. Rev.* D89 (2014), 125012.

[43] P. Lau and N. Manton. "States of Carbon-12 in the Skyrme model". *Phys. Rev. Lett.* 113 (2014), 232503.

[44] R. Leese, N. Manton, and B. Schroers. "Attractive channel Skyrmions and the deuteron". *Nucl. Phys.* B442 (1995), 228.

[45] N. Ma, C. Halcrow, and H. Zhang. "Effect of the Coulomb energy on Skyrmions". *Phys. Rev.* C99 (2019), 044312.

[46] R. Machleidt and D. Entem. "Chiral effective field theory and nuclear forces". *Phys. Rep.* 503 (2011), 1.

[47] O. Manko, N. Manton, and S. Wood. "Light nuclei as quantised Skyrmions". *Phys. Rev.* C76 (2007), 055203.

[48] N. Manton. "A remark on the scattering of BPS monopoles". *Phys. Lett.* B110 (1982), 54.

[49] N. Manton and P. Sutcliffe. *Topological Solitons*. Cambridge University Press, 2004.

[50] N. Manton and S. Wood. "Reparametrising the Skyrme model using the Litihum-6 nucleus". *Phys. Rev.* D74 (2006), 125017.

[51] M. L. Mehta. *Random Matrices*. Academic Press, 2004.

[52] B. Moussallam. "Casimir energy in the Skyrme model". *Conf. Proc.* C9209271 (1992), 269.

[53] C. Nave. "The most tightly bound nuclei". *Am. Jour. Phys.* 57 (1989), 552.

[54] C. Naya and P. Sutcliffe. "Skyrmions and clustering in light nuclei". *Phys. Rev. Lett.* 121 (2018), 232002.

[55] C. Naya and P. Sutcliffe. "Skyrmions in models with pions and rho mesons". *JHEP* 1805 (2018), 174.

[56] B. Piette and D. Tchrakian. "Static solutions in the U(1) gauged Skyrme model". *Phys. Rev.* D62 (2000), 025020.

[57] W. Press, S. Teukolsky, W. Vetterling, and B. Flannery. *Numerical Recipes in Fortran 77, 2nd Edition*. Cambridge University Press, 1992.

[58] J. Rawlinson. "An alpha-particle model for Carbon-12". *Nucl. Phys.* A975 (2018), 122.

[59] M. Richardson and N. Balazs. "On the network model of molecules and solids". *Ann. Phys.* 77 (1972), 308.

[60] P. Runge. "Die farben-kugel oder construction des verhaeltnisses aller farben zueinander". *Hamburg* (1810).

[61] T. Sakai and S. Sugimoto. "Low energy hadron physics in holographic QCD". *Prog. Theor. Phys.* 113 (2005), 843.

[62] T. H. R. Skyrme. "A nonlinear field theory". *Proc. Roy. Soc.* A260 (1961), 127.

[63] P. Sutcliffe. "Skyrmions in a truncated BPS theory". *JHEP* 1104 (2011), 045.

[64] P. Sutcliffe. "Skyrmions, instantons and holography". *JHEP* 08 (2010), 019.

[65] T. Walhout and J. Wambach. "Nucleon-nucleon potential in the Skyrme model: beyond the product approximation". *Phys. Rev. Lett.* 67 (1991), 314.

[66] E. Wigner. "Characteristic vectors of bordered matrices with infinite dimensions". *Ann. Math.* 62 (1955), 548.

[67] K. Wilson. "Confinement of quarks". *Phys. Rev.* D10 (1974), 2445.

[68] E. Witten. "Baryons in the 1/N expansion". *Nucl. Phys.* B160 (1979), 57.

[69] B. Zhou, A. Tohsaki, H. Horiuchi, and Z. Ren. "Breathing-like excited state of the Hoyle state in C-12". *Phys. Rev.* C94 (2016), 044319.